

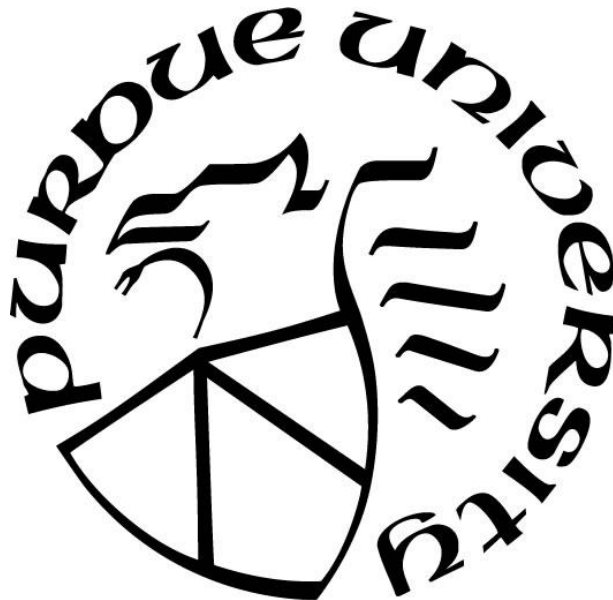
**IMPURITY CONTROL AND ANALYSIS OF ULTRA-PURE GALLIUM
FOR INCREASING MOBILITY IN GALLIUM ARSENIDE GROWN BY
MOLECULAR BEAM EPITAXY**

by
Kyungjean Min

A Dissertation

*Submitted to the Faculty of Purdue University
In Partial Fulfillment of the Requirements for the degree of*

Doctor of Philosophy



School of Materials Engineering

West Lafayette, Indiana

May 2019

**THE PURDUE UNIVERSITY GRADUATE SCHOOL
STATEMENT OF COMMITTEE APPROVAL**

Dr. Kevin P. Trumble

School of Materials Engineering

Dr. David R. Johnson

School of Materials Engineering

Dr. Eric P. Kvam

School of Materials Engineering

Dr. Michael J. Manfra

Department of Physics and Astronomy

Approved by:

Dr. David F. Bahr

Head of the Graduate Program

Dedicated to My Grandmother, Gilwoo Lee in Heaven

ACKNOWLEDGMENTS

I have longed for this PhD degree since I was in middle school. However, there were many difficulties and obstacles for the PhD degree, as if it went far away because I wanted it. I know graduate school life is tough for everyone. But, I can definitely say my graduate school years were much more challenging and tough than others, just considering the time (10.5 years) that I spent at graduate schools for two master's degrees and one doctoral degree. But, there were also miraculous moments so I could continue my PhD research and finally obtain a PhD degree. And these miraculous moments were thanks to wonderful people in the following.

Most of all, I truly thank my advisor, Professor Trumble. Without his guidance and supports, I could not overcome many challenges in my PhD research and I could not be a materials scientist like now. There is an old saying, "Give a man a fish, and you feed him for a day. Teach a man to fish, and you feed him for a lifetime." Professor Trumble taught me how to think of new ideas, formulate the ideas and complete the ideas, rather than just giving the ideas. These are very valuable for my lifetime research.

I also thank my advisor, Professor Johnson. Professor Johnson helped me a lot in my Master's Thesis in Materials Engineering and always tried to give me many opportunities in research. I am also grateful to Professor Manfra for his supports, especially giving me a chance to learn Molecular Beam Epitaxy (MBE) and have experiences in the MBE related experiments. I also thank Professor Kvam for his advice on dissertation and his classes I could accumulate fundamental knowledge in Materials Engineering.

I also thank Dr. Gardner who was very supportive to Molecular Distillation Experiment. I also would like to thank Dr. Wood and Ms. Rothwell for the ICP-MS analysis and useful discussions.

I should not miss to thank Dr. Atkinson, Purdue Graduate School and Purdue Fellowship office who helped me and awarded me fellowships for two years so I could continue my PhD research in Materials Engineering. I also thank many MSE fellow students and friends in Purdue Korean Catholic Association. Especially, I would like to thank Dr. Lisa Nielsen for her friendship and mental support.

I truly thank my family: Mom, Dad and my little brother. My family always supported me in every way. Without their supports, I could not survive in Lafayette and could not complete my PhD research

Lastly, I would like to remember my grandpa and two grandmas who passed away last year. Due to the scheduled experiments for this dissertation, I was not with them when they passed away. I am really sorry for that with my endless tears. Especially, this thesis (dissertation) is dedicated to my grandma, Gilwoo Lee, who was very supportive to my study, encouraged me to pursue PhD degree and really wanted to see my graduation for the PhD degree.

TABLE OF CONTENTS

LIST OF TABLES	8
LIST OF FIGURES	9
ABSTRACT	13
1. INTRODUCTION	15
2. BACKGROUND	17
2.1 Mobility and Impurity Scattering.....	17
2.2 Heterostructure (GaAs/AlGaAs) Design	18
2.3 Methods of Ultra-Purification of Ga.....	19
2.4 Objectives of Thesis.....	20
3. MOLECULAR DISTILLATION THEORY.....	22
3.1 Distillation and Evaporation Theory.....	22
3.2 Evaporation Behavior of Pure Ga in MBE	24
3.2.1 Experimental Conditions of In-Situ MBE Distillation and Growth	24
3.2.2 Free Evaporation.....	25
3.2.3 Transmission Probability of Evaporating Ga Species at Vertical Standing Crucible	27
3.2.4 Evaporated Ga amount from the Receding Ga Surface in MBE Crucible	33
3.3 Molecular Distillation of Impurities	36
3.4 Molecular Distillation Kinetics.....	38
4. IN-SITU MBE DISTILLATION ANALYSIS BY ICP-MS	44
4.1 Motivation of Elemental Analysis of Ultra-pure Ga.....	44
4.2 Analysis initial ultra-pure Ga and residual Ga by ICP-MS	46
4.2.1 Experimental.....	46
4.2.2 Results and Discussion	50
4.3 Implications of ICP-MS Results and Background of Chemical Separation of Ga	63
4.4 Thermodynamic study of Ga separation by Sephadex G-25	66
5. ACTIVE OXIDATION OF GERMANIUM.....	74
5.1 Calculations of Ge Atomic Evaporation.....	74
5.2 Germanium active oxidation hypothesis from Si active oxidation model.....	76
5.3 Germanium oxidation analysis	77

5.4	Construction of vapor species diagram of Ge-O system	81
5.4.1	Pure Ge	81
5.4.2	Dilute Ge in Ga(l)	85
5.4.3	The oxidation and evaporation behavior of 1 ppm Ge in Ga in MBE system.....	89
5.5	Justification of Active Oxidation by Mass Balance and Flux Calculations.....	91
5.6	Consideration of other volatile compound evaporation causing Ge loss.....	95
5.6.1	The formation of GeO from N ₂ O or NO ₂ involvement	95
5.6.2	Volatile GeCl ₄	96
6.	MOLECULAR DISTILLATION EXPERIMENT	97
6.1	Setup of Vacuum Chamber for Materials Distillation	97
6.2	Chamber Baking and Leak Testing.....	104
6.3	Preliminary Experiment for Distillation of 7N Ga (Cell Outgassing, Crucible Outgassing and Power Increase Test).....	110
6.4	Distillation Experiment.....	119
6.5	Results and Discussion	125
6.5.1	Gallium Recovered	125
6.5.2	GDMS Analysis.....	125
6.5.3	Analysis of RGA spectra during distillation.....	127
6.5.4	Ga Evaporation Analysis	136
6.5.5	Calculations of Solubility of Oxygen in Ga	139
7.	CONCLUSIONS	144
	APPENDIX A. SourCe Cell Drawing	148
	APPENDIX B. GDMS Analysis Results.....	150
	REFERENCES	153
	VITA.....	158

LIST OF TABLES

Table 3.1 Maximum evaporation rate and evaporated amount of Ga for distillation and growth	27
Table 3.2 Evaporation rate and evaporated amount of Ga for distillation and growth with collision and condensation effects	35
Table 3.3 The time for an impurity concentration to reduce to the half of the initial concentration (1 ppm) at 1360 K from the MBE crucible.....	42
Table 3.4 Activity coefficient of impurities in Ga found in literature	43
Table 4.1 Possible Polyatomic Species Interfering with Ge, Fe, Sn and Zn for Ga in HNO ₃	49
Table 4.2 Concentration of Ge, Zn, Sn and Fe measured in initial and recovered Ga for the grade of 6N, 7N and 8N by ICP-MS [ppb].....	50
Table 4.3 Signals of ⁷² Ge and ⁷⁴ Ge in 6N Ga and their ratio.....	51
Table 4.4 Results of ⁶⁶ Zn detection in 7N and 8N Ga samples by standard addition method.....	55
Table 4.5 Detection of ⁶⁶ Zn in 7N Ga in the increased wash-out time	56
Table 4.6 Results of ⁵⁶ Fe detection in 6N and 7N Ga by standard addition method	57
Table 4.7 Gallium hydrolysis reaction at 25 °C	67
Table 4.8 Germanium hydrolysis reaction at 25 °C	67
Table 5.1 Thermodynamic data of Ge, Ge oxide, and oxygen	80
Table 6.1 Decreased element in distillation.....	126
Table 6.2 Increased element in distillation	126

LIST OF FIGURES

Fig. 2.1 Schematic diagram of GaAs/AlGaAs heterostructure and conduction bands with an electron density in each conduction band	18
Fig. 2.2 Mechanism of zone refining	20
Fig. 3.1 MBE Ga crucible (Veeco) and schematic diagram of crucible dimension	25
Fig. 3.2 Maximum evaporation rate of Ga from MBE crucible for the Ga liquid surface area of 3.14 cm^2 as a function of temperature	27
Fig. 3.3 Schematic diagram of the movement of gas particles inside the crucible in four different cases (a) liquid surface – crucible opening end, (b) liquid surface – wall surface, (c) wall surface – crucible opening end, (d) wall surface – wall surface and (e) wall surface – liquid surface.	29
Fig. 3.4 The variation of transmission probability at the presence of collision in the crucible depending on length between melt surface and crucible end at $r = 0.95 \text{ cm}$	31
Fig. 3.5 The variation of transmission probability with the presence of collisions in the crucible depending on length between melt surface and crucible end at $L = 5 \text{ cm}$	32
Fig. 3.6 Receding length for 16 hours distillation as a function of time.....	34
Fig. 3.7 Receding length for 400 hours distillation as a function of time.....	34
Fig. 3.8 Vapor pressures of Ga and impurities as a function of temperature	37
Fig. 3.9 Evaporation rate of 1 ppm impurities and pure Ga as a function of distillation temperature	38
Fig. 3.10 Residual concentrations over distillation time for overall impurities with the 1 ppm initial concentrations distilled at 1360 K	40
Fig. 3.11 The residual concentrations of 1 ppm Cd after distillation at 1360 K as a function of distillation time	40
Fig. 3.12 The residual concentrations of 1 ppm Zn and Mg after distillation at 1360 K as a function of distillation time.....	41
Fig. 3.13 The residual concentrations of 1 ppm Ag, In and Mn after distillation at 1360 K as a function of distillation time.....	41
Fig. 3.14 The residual concentrations of 1 ppm Ge after distillation at 1360 K as a function of distillation time	42

Fig. 3.15 Indium residual concentration change in logarithmic scales with the comparison of free evaporation and evaporation from receding surface in the MBE crucible	43
Fig. 4.1 Germanium signal comparison for 7N and 8N Ga in HNO ₃ at different total dissolved solids (a) Ion intensity of ⁷² Ge, ⁷⁴ Ge and ⁴⁰ Ar ⁴⁰ Ar ⁺ versus TDS for 8N Ga. (b) Ion intensity of ⁷⁴ Ge, ⁸⁹ Y and ⁴⁰ Ar ⁴⁰ Ar ⁺ versus TDS for 7N Ga.....	60
Fig. 4.2 ¹²⁰ Sn signal comparison in different concentration of dissolved Ga in HNO ₃ , comparing to ⁸⁹ Y and ⁴⁰ Ar ⁴⁰ Ar ⁺ variance. (a) Ion intensity of ¹²⁰ Sn, ⁸⁹ Y and ⁴⁰ Ar ⁴⁰ Ar ⁺ versus TDS for 8N Ga. (b) Ion intensity of ¹²⁰ Sn, ⁸⁹ Y and ⁴⁰ Ar ⁴⁰ Ar ⁺ versus TDS for 7N Ga.....	62
Fig. 4.3 Hydrolysis constant (quotient) of Ga-hydroxide species Ga(OH) ₃ (top) and Ga(OH) ₄ ⁻ (bottom) as a function of ionic strength with and without 0.1 M medium	69
Fig. 4.4 Hydrolysis constant (quotient) of Ge hydroxide species GeO(OH) ₃ ⁻ (top) and GeO ₂ (OH) ₂ ²⁻ (bottom) as a function of ionic strength with and without 0.1 M medium	70
Fig. 4.5 Speciation diagram of Ga-hydroxide distribution as a function of pH, I = 0.64 M in the absence of medium	71
Fig. 4.6 Speciation diagram of Ge-hydroxide distribution as a function of pH, I = 0.64 M in the absence of medium	72
Fig. 5.1 Equilibrium P(O ₂) of the formation of GeO ₂ (s) in the reaction of (1)	78
Fig. 5.2 Vapor species diagram for pure Ge-O system at growth and distillation temperature....	82
Fig. 5.3 Transition points of active oxidation to passive oxidation for pure Ge.....	84
Fig. 5.4 Vapor Species diagram comparison of 1 ppm Ge-O system and pure Ge-O system at 1360 K.....	87
Fig. 5.5 Transition points of active oxidation to passive oxidation for 1 ppm Ge.....	88
Fig. 5.6 Vapor species diagram of 1 ppm Ge-O system at 923 K, 1160 K, and 1360 K.....	89
Fig. 5.7 Oxygen flux change upon P(O ₂) in the system.....	95
Fig. 6.1 Materials distillation chamber drawing.....	99
Fig. 6.2 Installed materials distillation chamber.....	100
Fig. 6.3 The first RGA spectrum of materials distillation chamber after installation	102
Fig. 6.4 Source cell (see Appendix A for detailed schematic).....	103
Fig. 6.5 RGA spectra from the chamber initial vacuum level(red) and after two days additional pumping (blue).....	104
Fig. 6.6 Materials distillation chamber surrounded with heating tapes	106

Fig. 6.7 Materials distillation chamber Al foils are covered with	106
Fig. 6.8 RGA Spectra before (red) and after (blue) cell heating and chamber baking, chamber and cell at room temperature	108
Fig. 6.9 RGA spectra before (red) and after (blue) chamber baking and cooling to room temperature, with cell at 460 °C (733 K).....	108
Fig. 6.10 Scratch approximately 1 mm long on knife edge of 6-in. CF flange on chamber bottom	110
Fig. 6.11 Schematic drawings and picture of PBN crucible	112
Fig. 6.12 Ar bag placed below chamber for crucible loading and the loaded crucible to the cell inside the Ar bag	112
Fig. 6.13 Experimental parameter change during the first crucible outgassing.....	114
Fig. 6.14 Experimental parameter change during the second crucible outgassing.....	116
Fig. 6.15 Experimental parameter change during the third crucible outgassing	117
Fig. 6.16 Experimental parameter change during the fourth crucible outgassing	118
Fig. 6.17 RGA spectrum of the Materials Distillation Chamber before distillation experiment	120
Fig. 6.18 Traps connected to the chamber in liquid nitrogen	121
Fig. 6.19 Changes of experimental parameters during distillation of 7N Ga	122
Fig. 6.20 Schematic diagram of the chamber cell installed	123
Fig. 6.21 Gallium sample in the crucible before heating (left) , 10 min later heating started and at 309 K (center) and during distillation at 1360 K (right).....	124
Fig. 6.22 Vapor Species diagram for 440 ppb Ge-O system at 1360 K	127
Fig. 6.23 RGA monitoring for P(O ₂) and P(GeO) with total pressure during distillation of 7N Ga	128
Fig. 6.24 Major gases measured in the RGA showing the decreased P(O ₂) during distillation of 7N Ga	129
Fig. 6.25 RGA monitoring for P(O ₂) and P(GeO) with total pressure in the second crucible outgassing	130
Fig. 6.26 RGA monitoring for P(O ₂) and P(GeO) with total pressure in the third and fourth crucible outgassing.....	131
Fig. 6.27 Major gases measured in the RGA during the second crucible outgassing.....	132
Fig. 6.28 Major gases measured in the RGA during the third and fourth crucible outgassing...	133

Fig. 6.29 RGA monitoring for P(O ₂) and P(GeO) in the third and fourth crucible outgassing..	134
Fig. 6.30 The solubility of oxygen in liquid Ga in equilibrium and stable phase depending on P(O ₂) at 1360 K, 1160 K and 923 K.....	142

ABSTRACT

Author: Min, Kyungjean. PhD

Institution: Purdue University

Degree Received: May 2019

Title: Impurity Control and Analysis of Ultra-Pure Gallium for Increasing Mobility in Gallium Arsenide Grown by Molecular Beam Epitaxy

Major Professors: Kevin Trumble and David Johnson

High mobility 2DEG (two-dimensional electron gas) confined in GaAs is a good platform to understand correlated electron systems and a promising candidate for qubit devices. For example, the non-Abelian feature of Fractional Quantum Hall state enabling topological quantum computation is only found in GaAs with high mobility. Theoretical calculations have shown that the mobility is inversely proportional to impurities in GaAs/AlGaAs heterstructures grown by Molecular Beam Epitaxy (MBE). In recent MBE experiments, the source Ga was found to be more important in the limitation of mobility than Al and As. A high mobility of 35 million cm^2/Vs was recently observed when an 8N Ga (total nominal impurity concentration of ~ 10 ppb) source was used compared to 25 million cm^2/Vs for a 7N Ga source. In addition, significant mobility increase was observed after in-situ distillation of the source Ga before growth. In order to clarify the mechanism of how the distillation contributed to the Ga purification, thus resulting in the mobility increase, the MBE in-situ distillation was analyzed by molecular distillation theory. Evaporation behavior of solvent Ga was analyzed including effects of evaporation from a crucible with receding liquid depth. Then impurity removal through molecular distillation was analyzed with molecular evaporation kinetics. The remaining 7N and 8N Ga after in-situ MBE distillation and growth were elementally analyzed by ICP-MS (Inductively Coupled Plasma Mass Spectrometry) and compared with analyses of the starting 7N and 8N Ga from same lots. Due to the increased detection limit of ICP-MS in metal analysis, the concentrations of most impurity elements reached the detection

limit of ~1-10 ppb. However, unusual high concentration of 690 ppb Ge was found in the 7N Ga, exceeding the nominal concentration of 7N (100 ppb). Significant decrease in Ge concentration was found in the comparison of initial ultra-pure Ga and remaining Ga for both grades of 7N and 8N. The significant Ge losses cannot be explained by atomic Ge evaporation due to the low vapor pressure of Ge. However, a hypothesis of Ge evaporation as GeO(g) by Ge active oxidation was proposed. In order to test the active oxidation of very dilute Ge in Ga in the MBE conditions with very low $P(O_2)$, the equilibrium $P(GeO)-P(O_2)$ vapor species diagram was calculated from thermodynamics. The analysis shows that even very dilute Ge in Ga of ~ 1 ppm concentration can be actively oxidized in the extremely low $P(O_2)$ of MBE. In order to prove active oxidation of Ge, molecular distillation of 7N Ga was performed in a specially constructed high vacuum chamber. The 7N Ga with unusual high Ge concentration of 440 ppb (by GDMS analysis) was distilled for 16 h at 1360 K under the starting $P(O_2)$ of 3×10^{-6} torr and the total pressure of 10^{-5} torr. The chamber vacuum was monitored by Residual Gas Analyzer (RGA) and the residual Ga after 16 h distillation was analyzed by GDMS. In the GDMS analysis, significant Ge loss was found from 440 ppb to below the detection limit of 10 ppb, confirming Ge active oxidation hypothesis. The oxygen-assisted impurity removal in distillation also may be applicable to other impurities with high vapor pressure gaseous oxide, but low vapor pressure itself, such as Al, Si and Sn.

1. INTRODUCTION

Fractional quantum Hall effect (FQHE) is the phenomenon that Hall conductance is quantized at half integer and is found to be present in GaAs/AlGaAs two-dimensional electron gas (2DEG) [1]. The non-Abelian phase characteristics of the FQHE allows GaAs/AlGaAs 2DEG to be a strong candidate for the qubit for quantum computing [2]. The observation of FQHE requires a certain amount of impurities in dopants as well as high purity and low defect GaAs/AlGaAs 2DEG to avoid scattering of electrons with impurities for high mobility [3].

Previous work has suggested mobility is inversely proportional to impurity concentration in GaAs/AlGaAs 2DEG from theoretical calculations [4]. More recently, Manfra and co-workers [5], [6] have shown increasing mobility with increase purity of the Ga source in MBE. In-situ MBE distillation of Ga was performed at 1360 K, which is 200 K above the growth temperature (~ 1160 K) for 16 h. After the distillation, there was 400 h growth. The significant increase of electron mobility in GaAs/AlGaAs 2DEG was found in the in-situ MBE distillation of Ga while no mobility increase was found in the distillation of other elements of Al and As. Moreover, the higher mobility of $35 \times 10^6 \text{ cm}^2/\text{Vs}$ was measured when purer Ga of 8N (99.999999 %, 10 ppb) grade was used, compared to the mobility of $25 \times 10^6 \text{ cm}^2/\text{Vs}$ with the use of 7N (99.99999 %, 100 ppb) grade Ga. This shows the purity of Ga plays a major role in the mobility of GaAs/AlGaAs 2DEG and even affects the realization of quantum computing.

As high purity Ga is demanded for the growth of GaAs/AlGaAs 2DEG, the chemical analysis method with low detection limit is required to determine the impurity concentration of ultra-pure

Ga. The most common analysis technique used today is Glow Discharge Mass Spectrometry (GDMS). However, GDMS is at the detection limit of about 1 ppb for most impurity elements already in the best commercially available Ga. Inductively Coupled Plasma Mass Spectrometry (ICP-MS) is known to be the state-of-the-art technique in elemental analysis with sub-parts-per-trillion (sub-ppt) detection limit. Since ICP-MS requires liquid samples, however, ultra-pure Ga must be dissolved in acid before introduction of the sample to the spectrometer.

This work will include the chemical analysis of ultra-pure Ga and distilled Ga by ICP-MS to determine if higher resolution chemical analysis is possible and to clarify the correlation of Ga purity and mobility and the mechanism of the distillation. In the chemical analysis of ultra-pure Ga by ICP-MS, limitations were found, which increase the potential detection limit of ICP-MS of sub-ppt. To improve the degraded detection limit, chemical separation of Ga by liquid chromatography will be suggested. In addition to the chemical analysis, the work for the analytical model development will be included to explain unusual results found in the analysis of distilled Ga samples by ICP-MS.

2. BACKGROUND

2.1 Mobility and Impurity Scattering

Mobility (drift mobility for electron) is defined by $\mu = \sigma/ne = e\tau/m$, where σ is the conductivity, e is the charge of the electron, n is the concentration of electrons, m is the effective mass and τ is the transport life time. In 2DEG, n is the 2D areal density. The transport lifetime τ is also called scattering time and affected by several independent scattering mechanism. In GaAs/AlGaAs 2DEG system the transport time, and thus mobility, is mainly affected by the following scattering [4], [7].

1. acoustic phonon scattering via deformation coupling
2. acoustic phonon scattering via piezoelectric coupling
3. impurity scattering by unintentional background charged impurities
4. impurity scattering by intentional dopants in the modulation doping delta layers

Mobility measurement is conducted at 0.3 K using cryogenic system of $^3\text{He}/^4\text{He}$ dilution refrigerator [5]. At the temperature of 0.3 K, acoustic phonon scattering is sufficiently weak. Therefore, the impurities mainly contributed to the mobility degradation are unintentional background charged impurities and intentional dopants in the modulation doping delta layers. The intentional dopants in the delta layer are invariably present impurities. On the while, the unintentional background charged impurities come from the source materials and vacuum of MBE system. Therefore, the concentrations of unintentional background charged impurities in 2DEG can decrease by purifying source materials and maintaining perfect vacuum system.

2.2 Heterostructure (GaAs/AlGaAs) Design

The sample grown using ultra-pure 7N and 8N Ga in Manfra and Coworker's work was GaAs/Al_{0.24}Ga_{0.76}As heterostructure. The heterostructure was grown on GaAs(100) substrate in the design of "doping well" as shown in Fig 2.1 [5], [6].

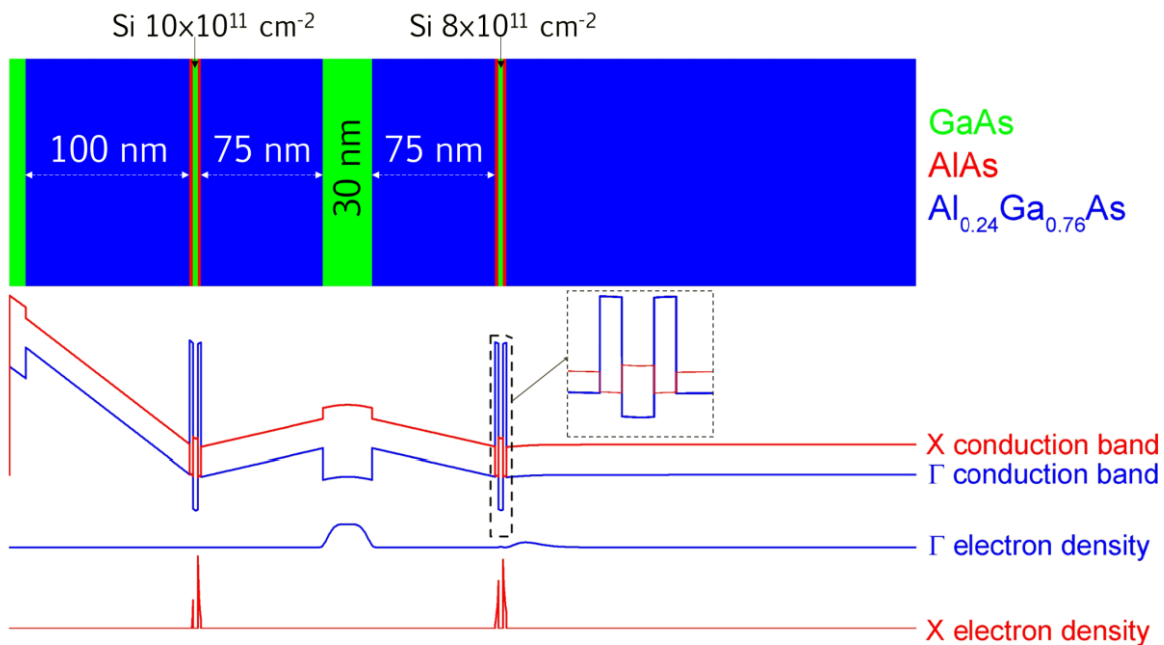


Fig. 2.1 Schematic diagram of GaAs/AlGaAs heterostructure and conduction bands with an electron density in each conduction band (Adapted from [6])

The GaAs where 2DEG resides had 30 nm thickness symmetrically surrounded by Al_{0.24}Ga_{0.76}As with 75 nm thickness. Above the AlGaAs barrier, the narrow GaAs quantum well of 2.9 nm was placed and the narrow GaAs quantum well was surrounded by AlAs barrier. Silicon was doped in the narrow GaAs quantum well in the concentration of $10 \times 10^{11} \text{ cm}^{-2}$ and $8 \times 10^{11} \text{ cm}^{-2}$.

2.3 Methods of Ultra-Purification of Ga

Purification depends on a material type as well as impurity type. Therefore, several purification methods are used through multistage separation processes to achieve semiconductor grade (99.99 % ~ 99.999999 %) purified materials. Typically used ultra-purification methods for Ga are vacuum distillation (refining) and zone refining [8].

Vacuum distillation is the molecular distillation that we will discuss in next chapter. One difference of typical vacuum distillation and in-situ MBE distillation is how the evaporating materials was treated. In the typical vacuum distillation, the evaporating materials were condensed and collected while in the in-situ MBE distillation, the evaporating materials were removed from the remaining liquid and also from the subsequent vapor beam that is condensing to make the film. In the typical vacuum distillation, the target material for purification is the condensed materials after evaporating. However, the purified materials in the in-situ distillation is residual after evaporation. The detailed principle will be discussed in the next chapter.

Zone refining is the separation using the solubility difference at solid-liquid interface introduced by Pfann [9]. As shown in Fig 2.2, when narrow molten zone passes through a long solid metal rod, impurities are ejected to the liquid region due to the difference in solubility of liquid phase and solid phase. The distribution coefficient, k , the ratio of the concentration of freezing solid to liquid, represents the redistribution of solute between solid and liquid when it melts and recrystallizes. When k is less than 1, impurities segregate to the liquid and are thus swept to the end of the bar. to the right end of solid metal rod as molten zone travels to the right. When k is greater than 1, impurities segregate to the opposite end that molten zone travels. The distribution

coefficient is materials and impurities specific constant. Depending on materials and impurities, distribution coefficient is different.

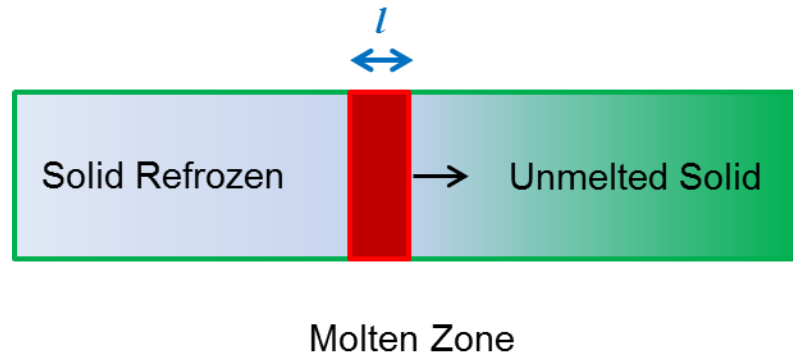


Fig. 2.2 Mechanism of zone refining

For the single pass of zone refining, the impurity concentration after zone refining is defined by the following equation.

$$C = C_0 \left[1 - (1-k) e^{-\frac{kx}{l}} \right] \quad (2.1)$$

where C is the solute concentration, C_0 is the initial solute concentration, k is the equilibrium distribution coefficient, x is the solidified length and l is the molten zone length. The distribution

2.4 Objectives of Thesis

This thesis covers the analysis of in-situ MBE distillation and growth by ICP-MS, the developed molecular distillation theory for the analysis of in-situ MBE distillation and molecular distillation experiment with the setup of vacuum chamber. In Chapter 3, molecular distillation is discussed starting from the previous evaporation theory to explain distillation. Then the developed solvent Ga and impurity evaporation behaviors from the receding surface in the MBE crucible are reported

with the developed molecular distillation kinetics. In Chapter 4, the initial ultra-pure 7N and 8N Ga and the recovered 7N and 8N Ga after distillation and growth were analyzed by ICP-MS. Three interferences in ICP-MS degrading the detection limit in metal analysis were reported. Thermodynamic study of Ga chemical separation from Ge to resolve the matrix interference of ICP-MS, thus improving the detection limit of ICP-MS, was also reported. In Chapter 5, unusual high Ge loss that cannot be explained by Ge atomic evaporation found in the ICP-MS was discussed. In order to explain high Ge loss, a Ge active oxidation hypothesis was proposed, and thermodynamic study was performed to support the Ge active oxidation hypothesis. In Chapter 6, molecular distillation experiment was discussed. The vacuum chamber setup for the molecular distillation experiment and the distillation experiment results of Ga evaporation, GDMS analysis for the impurity analysis and RGA monitoring was discussed.

3. MOLECULAR DISTILLATION THEORY

Molecular distillation is the separation of impurities from solvent material by heating the materials under high vacuum. Molecular distillation was used in the MBE GaAs/AlGaAs growth to purify Ga, thus increasing the mobility of 2DEG in GaAs/AlGaAs. In order to understand Ga purification mechanism in the in-situ MBE distillation, the evaporation behavior of the solvent Ga from the MBE crucible was analyzed ahead of the impurity evaporation. Based on Langmuir equations and Clausius theory for the evaporation, Ga evaporation from the receding surface in the MBE crucible over time, considering the collision and condensation effects was developed. The impurity evaporation was also analyzed based on Langmuir-Knudsen equation with the receding surface effect. The kinetics of molecular distillation for major impurities was developed.

3.1 Distillation and Evaporation Theory

Distillation is one of the inorganic materials purification methods by heating materials [10]. The impurities and solvent material have different vapor pressures. The relative difference of vapor pressure results in the different evaporation rates. Consequently, there is a difference in the degree of evaporation as heating materials due to the vapor pressure difference, thus resulting in purifications of the solvent material in the case when the solvent material has a lower vapor pressure than impurities. In metallurgical distillation processes, there are two types of distillations: equilibrium distillation and molecular distillation. In equilibrium distillation, more volatile impurities with higher vapor pressure than the solvent material (Ga in this study) can be distilled, while less volatile impurities with lower vapor pressure than the solvent material cannot be

distilled. However, molecular distillation is carried out under high vacuum, so the equilibrium is not maintained between the vapor and liquid. Therefore, all impurities can be distilled without interference of high vapor pressure and the distillation rate is proportional to the saturation vapor pressure of impurities.

Molecular distillation is based on the evaporation of each species in materials. Therefore, the molecular distillation rate depends on the evaporation rate. Langmuir [11] first derived the evaporation rate of a single component from the kinetic theory of gases and the evaporation rate is given by

$$w \left(\frac{\text{kg}}{\text{m}^2 \cdot \text{s}} \right) = 4.37 \times 10^{-3} \cdot P \sqrt{\frac{M}{T}} \quad (3.1)$$

Here P is the saturation vapor pressure in Pascal, T is absolute temperature in K, and M is molecular or atomic weight in g/mol. Evaporation according to (3.1) occurs under perfect vacuum, when the mean free path of the evaporating species is larger than the distance between the evaporating and condensing surface. Consequently, the evaporation rate of (3.1) can be named the maximum evaporation rate.

When the vacuum is not perfect, evaporation rate is given by [10],

$$w \left(\frac{\text{kg}}{\text{m}^2 \cdot \text{s}} \right) = 4.37 \times 10^{-3} \cdot (P - P') \gamma X \sqrt{\frac{M}{T}} \quad (3.2)$$

where P' (Pa) is the effective vapor pressure at the surface, γ is the activity coefficient of the impurity species, and X is the mole fraction of the impurity species. Since the equilibrium is not maintained and constant removal of evaporating vapor species occurs in the molecular distillation, the impurity distillation is not controlled by relative volatility to the solvent material. The

additional background vapor species present in the system disturb the path of evaporating impurity species. Hence, the vapor pressure of background species was deducted from the vapor pressure of the impurity.

3.2 Evaporation Behavior of Pure Ga in MBE

In order to clarify the separation of an impurity from Ga by molecular distillation, the evaporation behavior of Ga in the MBE crucible should be analyzed, because both solvent Ga and impurity evaporate together in the distillation. Hence, how Ga was evaporated in the in-situ MBE distillation and growth of the second growth campaign comparing with the observed Ga loss is a cornerstone of molecular distillation analysis in this section.

3.2.1 Experimental Conditions of In-Situ MBE Distillation and Growth

Ingots of 7N and 8N Ga totaling 100 g each were loaded to crucibles, which were subjected to in-situ distillation for further purification at 1360 K for a total of 16 hours. Between distillation steps, there was growth at 1160 K for a total of 400 hours. Before starting the distillation, between distillation and growth and between each growth, Ga was stored at idle temperature of 923 K for a total of about one year. However, Ga vapor pressure at 923 K was five orders smaller than 1360 K, and thus the evaporated amount at 923 K was negligibly small, at ~ 0.4 g, though it lasted for a year. Therefore, Ga evaporation at the idle temperature of 923 K is not considered in this chapter. After distillation and growth were finished, the observed Ga loss was 25 g for 7N Ga and 29.6 g for 8N Ga.

The Ga crucible is slightly conical, nearly cylindrical. The dimensions of the crucible and the estimated values of diameter and initial depth of liquid, L , when the crucible is filled with 100 g liquid Ga are illustrated in Fig 3.1.

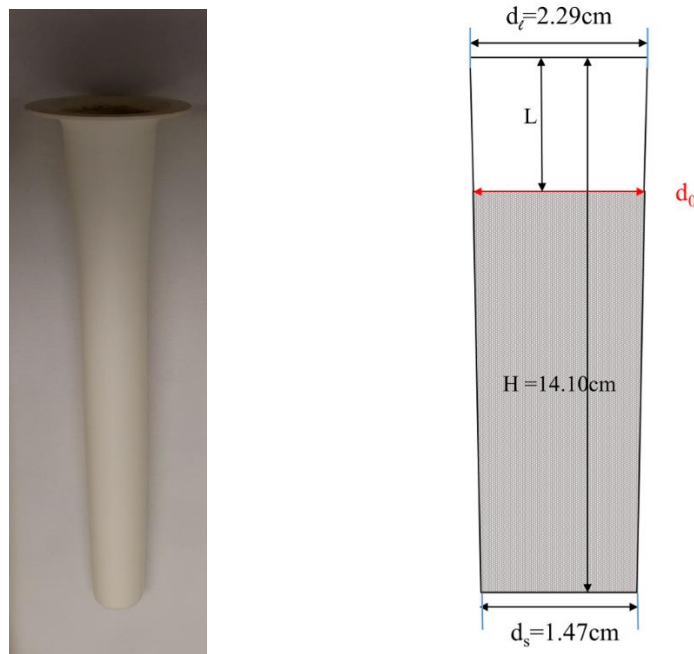


Fig. 3.1 MBE Ga crucible (Veeco) and schematic diagram of crucible dimension
($L_0 = 1.04$ cm, $d_0 = 1.90$ cm)

3.2.2 Free Evaporation

The MBE in-situ distillation and growth of GaAs/AlGaAs was performed in ultra-high vacuum of about 1×10^{-10} Torr ($= 1.33 \times 10^{-8}$ Pa). Consequently, this distillation process is applied to molecular distillation. When there is no returning condensation from vapor phase to liquid phase, the evaporation rate is maximum. The maximum evaporation rate is given by Langmuir equation of (3.1).

The Ga vapor pressure from 600°C to 1200°C is given by [12],

$$\text{Log}(P/\text{atm}) = -13984/T + 6.754 - 0.3413 \times \text{Log}(T) \quad (3.3)$$

As discussed in the above, the maximum evaporation rate under the perfect vacuum condition is defined by the Langmuir equation (3.1). For the initial 100 g of Ga in the crucible, the radius of circular liquid surface calculated from the taper of the crucible, shown in Fig 3.1, is 0.948 cm and surface area of the Ga melt is 2.82 cm². As the crucible is tilted to 26 degrees vertically in the MBE, the surface area of Ga melts increases to 3.14 cm². Using these values, the evaporation rate of Ga from 800 K to 1400 K is shown in Fig 3.2. The amount of Ga evaporated can be obtained from Langmuir equation by multiplying surface area of Ga melt that faces with the vapor phase and evaporation time (16 hours for distillation and 400 hours for growth). These are listed in Table 3.1 for the distillation and growth steps.

As shown in Table 3.1, a total of 67.9 g of Ga is predicted to be lost, with the majority being during the distillation step. This is because Ga saturation vapor pressure in distillation is two orders higher than that in growth. Clearly, free evaporation using the Langmuir equation overestimates the actual Ga loss of 25 ~ 30 g.

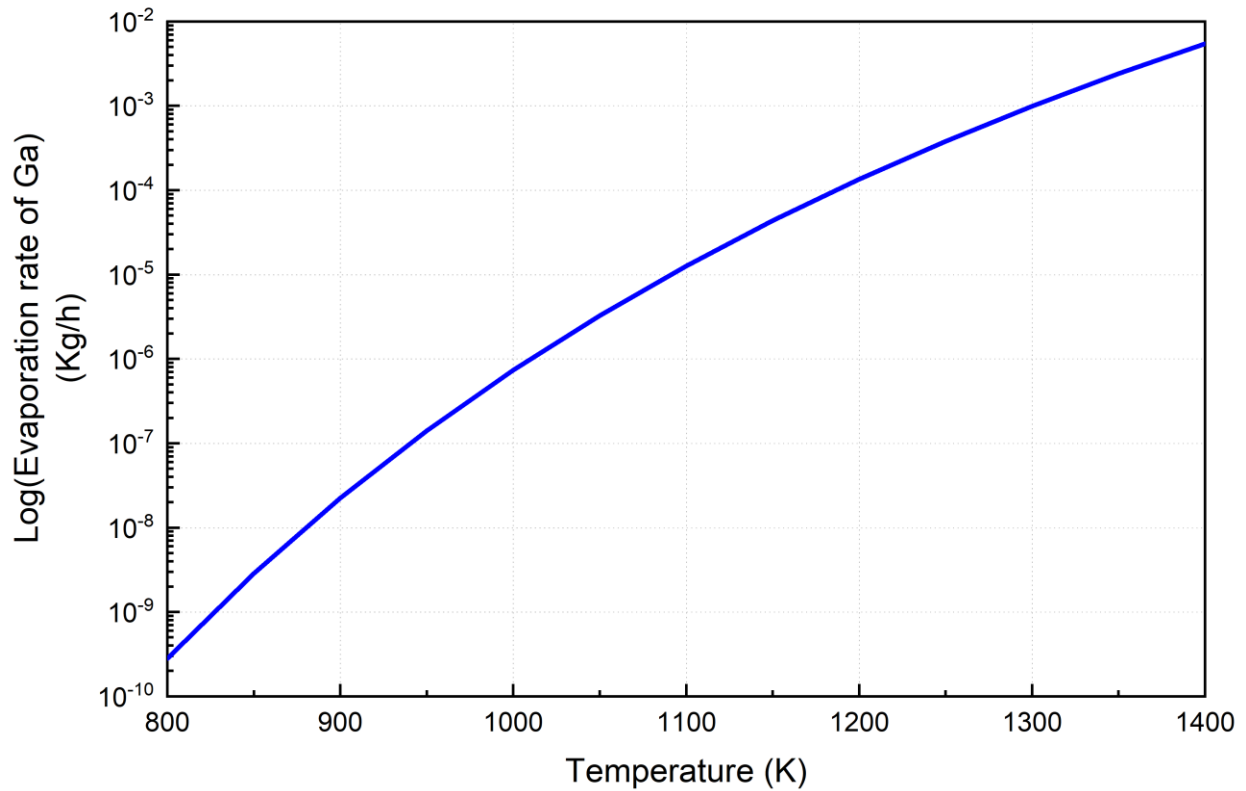


Fig. 3.2 Maximum evaporation rate of Ga from MBE crucible for the Ga liquid surface area of 3.14 cm^2 as a function of temperature

Table 3.1 Maximum evaporation rate and evaporated amount of Ga for distillation and growth

	Time (h)	Temperature (K)	Ga Saturation Vapor pressure (atm)	Evaporation Rate ($\text{kg/m}^2 \cdot \text{s}$)	Evaporated Ga amount (g)
Distillation	16	1360	2.52×10^{-5}	2.53×10^{-3}	45.8
Growth	400	1160	4.50×10^{-7}	4.88×10^{-5}	22.1

3.2.3 Transmission Probability of Evaporating Ga Species at Vertical Standing Crucible

The evaporated particles inside the crucible either pass through without striking the crucible walls or collide with the walls. The molecules that once collided with the walls go through one of the

following processes: passing through the exit, returning to the entrance and condensing, or striking with the wall again.

Clausing derived the transmission probability for emitted gas particles from the crucible for the case of particles directly passing through the crucible without collision, and for the case of passing through the crucible with collisions [13].

The MBE crucible was open. The motion of gas particles that would evaporate from the crucible can be divided into the following ways as depicted in Fig 3.3: (a) movement from the liquid surface to the crucible opening end, (b) movement from the liquid surface to the wall surface, (c) movement from the wall surface to the crucible opening end, (d) movement from the wall surface to the upper wall surface, and (e) movement from the wall surface to the liquid surface. The φ is the angle between particle direction and Ga liquid surface normal. At low angles, φ , the gas particle travels in a straight line without collision. At larger angles, depending on the location of evaporation from the liquid surface, the particle will strike the wall. From the wall there are three possible further processes that may consist of returning back to liquid surface (e), colliding again with the wall surface (d), or direct evaporation to outside of crucible (c).

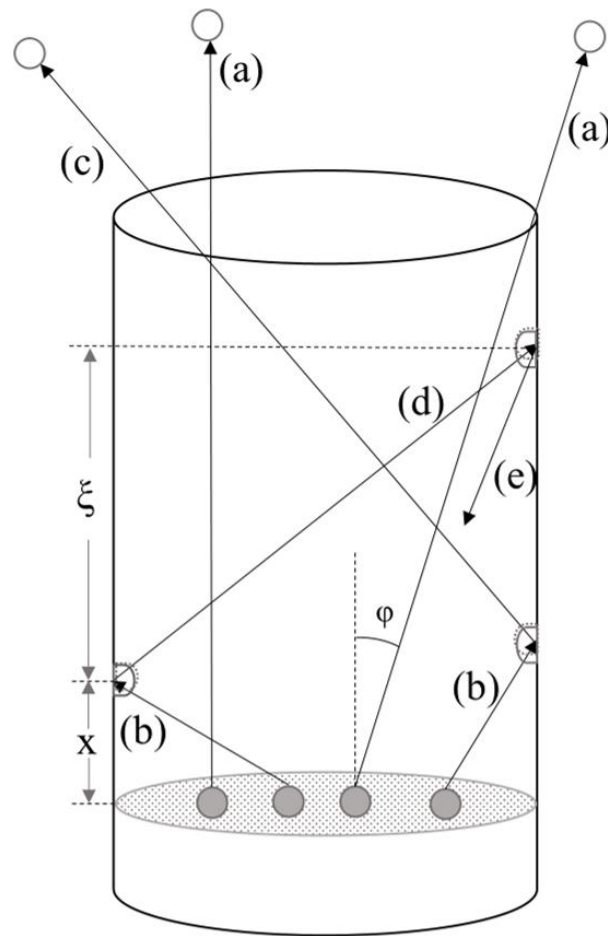


Fig. 3.3 Schematic diagram of the movement of gas particles inside the crucible in four different cases (a) liquid surface – crucible opening end, (b) liquid surface – wall surface, (c) wall surface – crucible opening end, (d) wall surface – wall surface and (e) wall surface – liquid surface.

The transmission probability is defined by equation (3.4).

$$K_c = \int_0^L W_{sr}(x) \cdot w(x) dx + W_{ss}(L) \quad (3.4)$$

where L is the length from the top of the crucible to the liquid Ga surface, W_{sr} is the probability that gas particles move from the liquid surface to the wall surface and W_{ss} is the probability that gas particles move from liquid surface to the crucible opening end. Here, $w(x)$ is the probability of collision at x inside the crucible and is defined by equation (3.5)

$$w(x) = \int_0^L W_{rr} (\xi - x) d\xi \cdot w(\xi) + W_{rs}(L - x) \quad (3.5)$$

where ξ is arbitrary point that collision occurs inside the crucible after the collision at x (Figure 3), W_{rr} is the probability that gas particles move from the wall surface to the upper wall surface, and W_{rs} is the probability that gas particles move from the wall surface to the crucible opening end. The possibility of particles returning to the liquid surface from the wall (case (e) in Figure 3) is neglected in the Clausing calculation. The probability of collision at x , $w(x)$, can be represented by equation (3.6)

$$w(x) = \alpha + \frac{1-2\alpha}{L} \cdot x \quad (3.6)$$

When the distance between melt surface and crucible opening end, L , is greater than the radius of melt surface, α is given by equation (3.7)

$$\alpha = \frac{[u(u^2+1)^{\frac{1}{2}}-u^2]-[v(v^2+1)^{\frac{1}{2}}-v^2]}{\frac{u(2v^2+1)-v}{(v^2+1)^{\frac{1}{2}}} - \frac{v(2u^2+1)-u}{(u^2+1)^{\frac{1}{2}}}} \quad (3.7)$$

with $v = \frac{L\sqrt{7}}{3L+2r\sqrt{7}}$ and $u = \frac{L}{2r} - v$.

Then the final transmission probability is represented by equation (3.8)

$$K_c = \frac{1-2\alpha}{3r^2L} \left\{ 4r^3 + (L^2 - 2r^2) (L^2 + 4r^2)^{\frac{1}{2}} - L^3 \right\} \\ + \alpha + \frac{1-\alpha}{2r^2} \left\{ L^2 - L (L^2 + 4r^2)^{\frac{1}{2}} + 2r^2 \right\} \quad (3.8)$$

The transmission probability of Ga particles, considering the probability of collision for the MBE crucible is the function of the distance between the melt surface and crucible opening end, as

shown in Fig 3.4, and the radius of crucible in Fig 3.5. As L is deeper, more collisions with the crucible walls occur. Hence, the transmission probability decreases as L increases, as shown in Fig 3.4. On the other hand, as radius increases, transmission probability increases, as suggested in Fig 3.5.

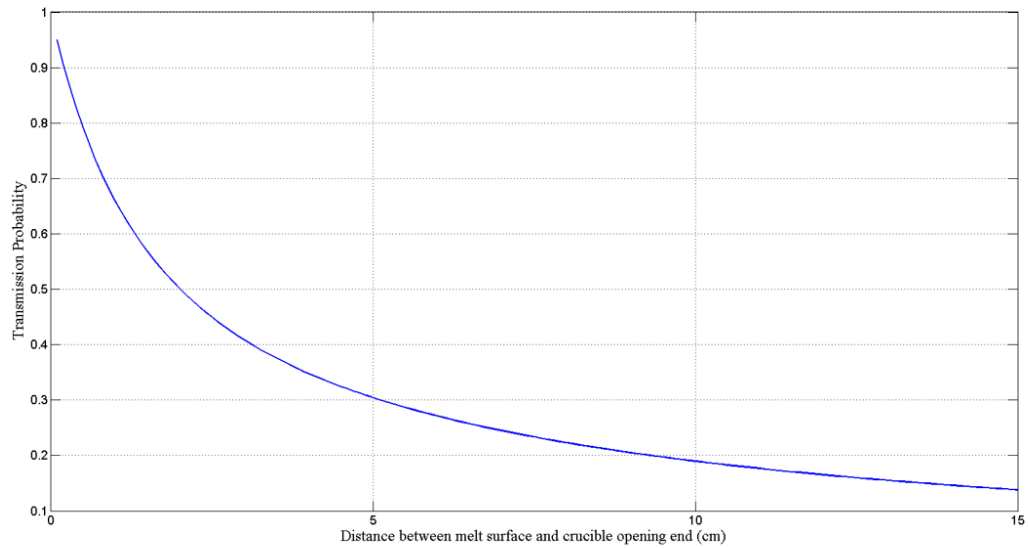


Fig. 3.4 The variation of transmission probability at the presence of collision in the crucible depending on length between melt surface and crucible end at $r = 0.95$ cm

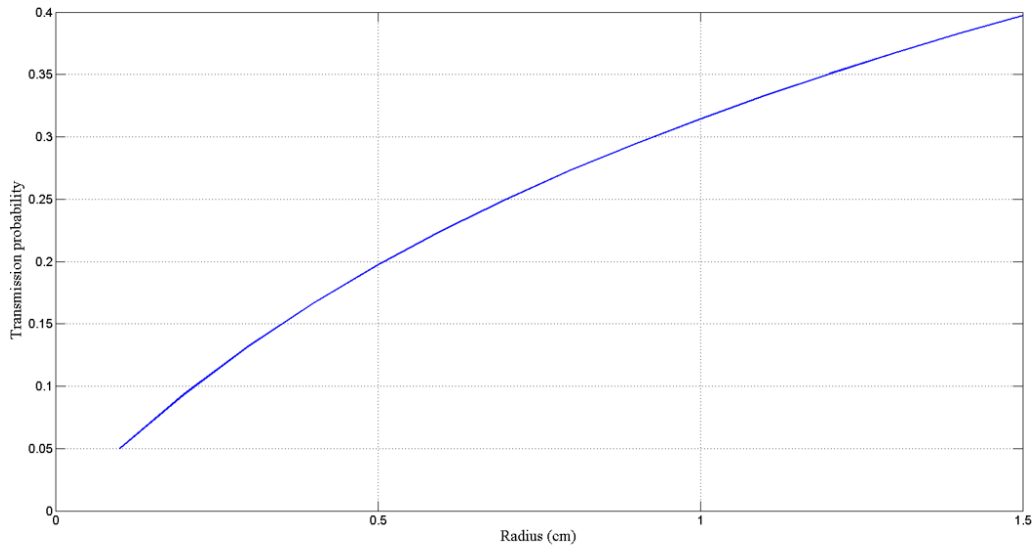


Fig. 3.5 The variation of transmission probability with the presence of collisions in the crucible depending on length between melt surface and crucible end at $L = 5$ cm

The evaporation rate in the presence of collisions is defined by multiplying transmission probability in equation (3.7) to free evaporation rate in equation (3.1) and given by equation (3.9)

$$W \left(\frac{\text{kg}}{\text{m}^2 \cdot \text{s}} \right) = 4.37 \times 10^{-3} \cdot K_c \cdot P \sqrt{\frac{M}{T}} \quad (3.9)$$

The evaporation rate is the evaporated mass per unit area of melt surface and unit time. The mass evaporated can be converted to volume change during evaporation. The change of volume in the cylindrical crucible is the surface area of melt times change of length (depth) of melt. If the surface area is assumed as a constant in a cylindrical crucible, the evaporation rate can be represented as a function of receding length in melts during evaporation, as indicated in equation (3.10). Then, the proportion of evaporation amount can be derived by integrating the infinitesimal change of length of melt over time.

$$\begin{aligned}
 W(\Delta \text{ weight}) &\rightarrow W(\Delta \text{ volume} \cdot \text{density}) \\
 &\rightarrow W(\Delta \text{ receding length} \cdot \text{surface area} \cdot \text{density})
 \end{aligned}
 \tag{3.10}$$

3.2.4 Evaporated Ga amount from the Receding Ga Surface in MBE Crucible

The evaporated Ga amount with particle collisions can be obtained from the integration of the evaporation rate W in equation (3.9), with the function of receding length, over time. To integrate the evaporation rate for the infinitesimal change of length over time, the equation of receding length that is associated with time is necessary. However, K_c depends on the receding length that varies over time and there is no explicit solution for the integration of W over time. Therefore, the equation between the receding length L and time was derived numerically by fitting data for each one-hour step of evaporation.

The fitting line for distillation for 16 hours is, $L = -0.0002t^3 + 0.0065t^2 - 0.078t$, from the initial parameters of $r = 0.95$ cm, $T = 1360$ K and $P = 4.50E-05$ atm. The fitting line for growth for 400 hours is $L = 10^{-9}t^2 - 2 \times 10^{-6}t + 0.006$, from the initial parameters of $r = 0.84$ cm, $T = 1160$ K and $P = 2.52E-07$ atm. The equations of receding length for distillation and growth are shown in Fig 3.6 and Fig 3.7.

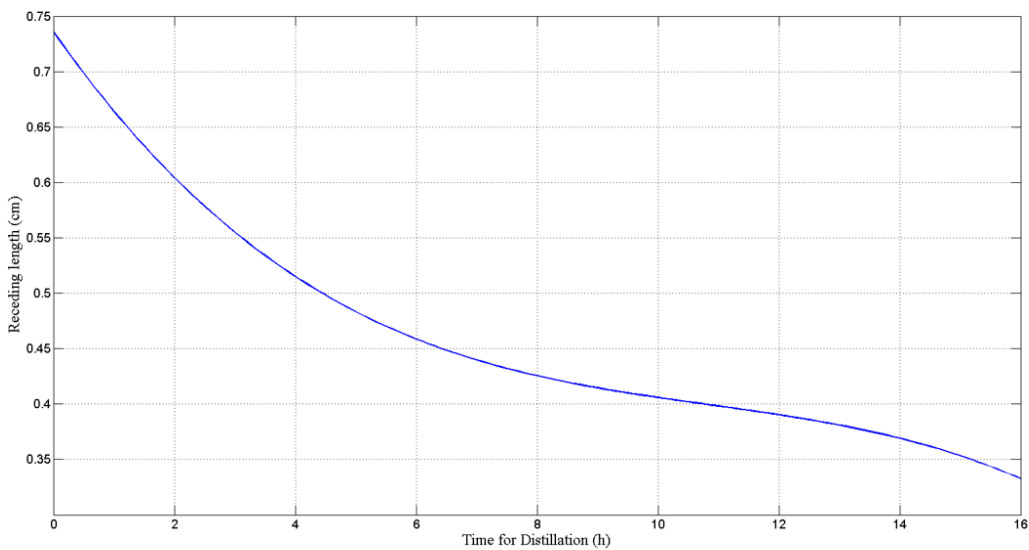


Fig. 3.6 Receding length for 16 hours distillation as a function of time

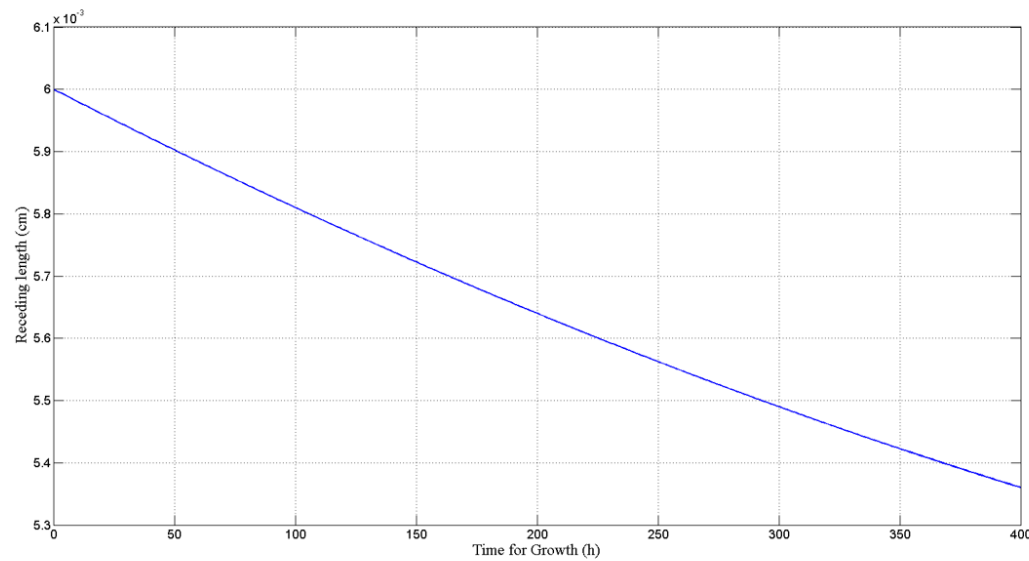


Fig. 3.7 Receding length for 400 hours distillation as a function of time

The amount of evaporated Ga for both distillation and growth in the presence of collisions is summarized in Table 6.2 with comparison to the evaporated amount for free evaporation. Since

the crucible was tilted from vertical about 26 degree, the surface area for derivation of amount was projected from 2.82 cm² to 3.14 cm².

The estimated result of 28.9 g was very close to the observation of 25 g. The difference of 3.9 g is likely because the consideration regarding the 26 degrees tilt of the Ga source crucible was not applied. Although the increase of Ga liquid surface area due to 26 degrees tilt was applied, more collisions with the wall due to the tilt and closed wall to the Ga liquid surface was not considered. The particles on the 90% of melt surface more probably collide with the crucible wall and condense back to the melt surface in the tilted crucible. Therefore, a smaller amount of Ga was evaporated in the observation than calculation. The degree of contribution by condensation in the tilted part to the evaporation amount will be discussed in a follow-up paper.

Table 3.2 Evaporation rate and evaporated amount of Ga for distillation and growth with collision and condensation effects

	Time (h)	Temperature (K)	Ga Saturation Vapor pressure (atm)	Evaporation Rate (kg/m ² ·s)	Evaporated Ga without collision (g)	Evaporated Ga with collision (g)
Distillation	16	1360	2.52×10^{-5}	2.53×10^{-3}	45.8	23.2
Growth	400	1160	4.50×10^{-7}	4.88×10^{-5}	22.1	5.7
Sum					67.9	28.9

Although the arsenic (As) background pressure of 1.5×10^{-5} torr and high vapor pressure of Ga are present together in the distillation of impurities during MBE operations, the deduction from the As pressure and Ga pressure are negligibly small compared to the impurity vapor pressures (for the impurities of Cd, Zn, Mg, Ca, Ag, In, and Mn) or too high to make the evaporation rate

negative (for the impurity of Au). Therefore, the effective background pressure due to As background and Ga evaporation was not considered in this study.

The collision and condensation effects from a receding surface in the MBE crucible were applied to the pyrolytic boron nitride (PBN) crucible (Union Carbide, Huston, TX) used in the first growth campaign. This crucible had a smaller dimension than the Veeco MBE crucible. When 25 g Ga was placed in the PBN crucible, the depth from the top of the crucible to Ga surface was 3.5 cm. For this geometry, Ga loss was expected to be ~ 0.7 g for 1 h distillation, ~ 2.4 g for 4 h distillation and ~ 6.4 g for 16 h distillation.

3.3 Molecular Distillation of Impurities

The evaporation rates of impurity elements of Ag, Au, Ge, Mg, Sn, and Zn in the distillation of Ga were calculated from equation (3.2). In the calculation, no collision and no condensation were assumed so that the particle once evaporated is not condensed back to the evaporation surface and is permanently separated from the solvent material (Ga in this study). The solution (Ga and impurities) behavior assumed to obey Raoult's law, hence the activity coefficient is 1. On the evaporation surface, impurities are assumed to be preferentially evaporated, leaving behind Ga.

The evaporation rate is proportional to the saturation vapor pressure of the species. The saturation vapor pressures from 600 K to 1400 K for the impurity elements and Ga are given by Fig. 3.8. The evaporation rates of impurities with the concentration of 1 ppm calculated as a function of distillation temperature are indicated in the Fig. 3.8, as defined in the equation (3.2). Since the

vacuum level of the MBE was $\sim 10^{-10}$ torr, the equilibrium vapor pressure of most impurity elements at the in-situ MBE distillation temperature of 1360 K was higher than the MBE vacuum pressure. Hence, the effect from the effective vapor pressure (MBE background vacuum pressure) was discarded. The evaporation rate of any impurity depends on the saturation vapor pressure of impurities at the corresponding distillation temperature. In a certain temperature range, the evaporation rates of Cd, Mg and Mg with 1 ppm concentrations are higher than that of pure Ga. However, the evaporation rates of all impurities are lower than that of pure Ga at the Purdue MBE distillation temperature of 1360 K.

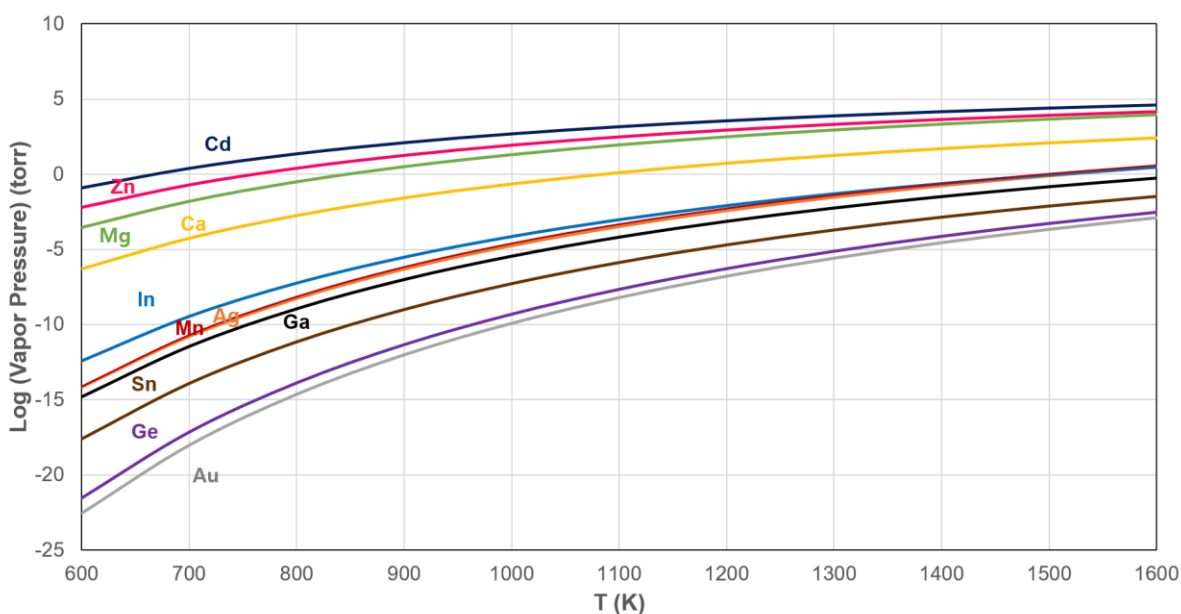


Fig. 3.8 Vapor pressures of Ga and impurities as a function of temperature

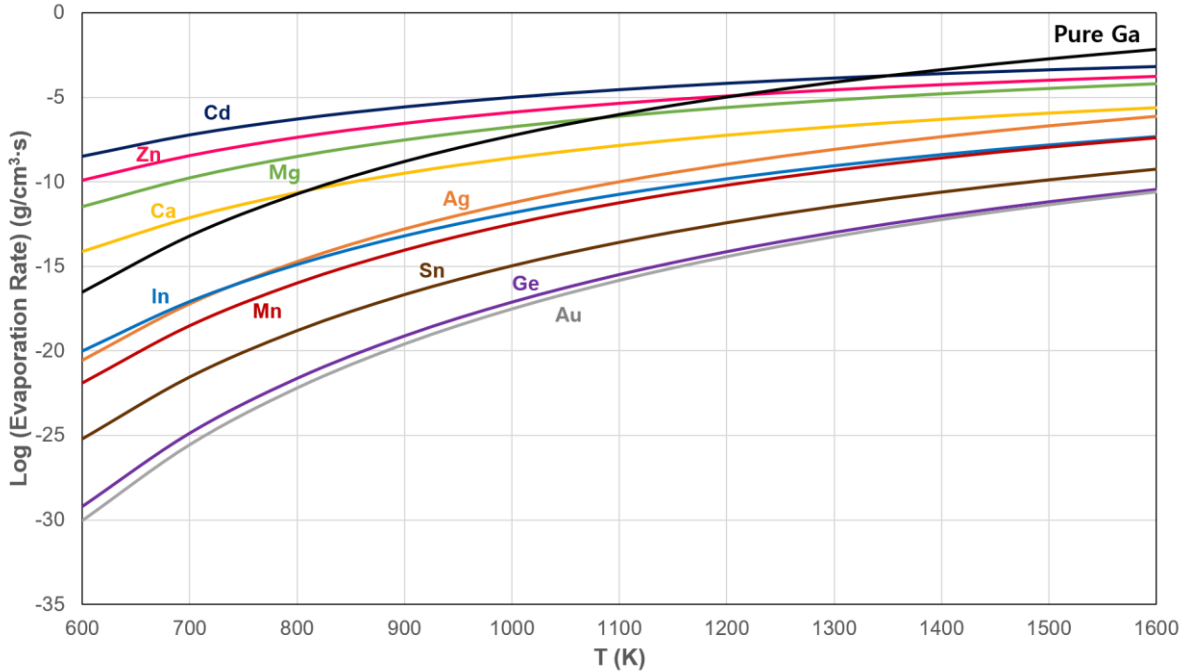


Fig. 3.9 Evaporation rate of 1 ppm impurities and pure Ga as a function of distillation temperature

3.4 Molecular Distillation Kinetics

Assuming the evaporation of solvent materials is negligible, the concentration changes over time during molecular distillation, so representing the kinetics can be obtained by converting the variables of equation (3.2). The residual concentration ($C(t)$) after distillation time t is defined by equation (3.11).

$$\frac{dC(t)}{dt} (g/s) = C(0) \cdot \exp\left(-\frac{0.0583}{m_i + \frac{M_i}{M_s} m_s} \cdot S \cdot P_i \cdot \gamma_i \sqrt{\frac{M_i}{T}} t\right) \quad (3.11)$$

where M_i and M_s are molecular weight of impurity and solvent material, m_s and m_i are initial weight of impurity and solvent material, $C(0)$ is the initial impurity concentration of impurity, and

S is the surface area of solvent. The weight of solvent material was assumed to be constant (no evaporation) and the activity coefficient was 1, as the solution obeys Raoult's law.

The residual concentrations for the overall impurities obtained from the equation (3) are indicated in Fig 3.10. For the better resolution of the graph of impurity residual concentrations over distillation time, the impurities were grouped based on the value of vapor pressure, shown in the Fig 3.11, Fig 3.12, Fig 3.13 and Fig 3.14. The equation (3.11) is the exponential function, which never reaches 0. Consequently, instead of the time for the full evaporation, the times for the half of the amount of impurities to be removed were calculated and are listed in Table 3.3.

As shown in Fig 3.10 and Table 3.3, the impurities of Cd, Mg, Zn with relatively high vapor pressure were fully distilled in a few seconds, while the impurities of Au and Ge, with relatively low vapor pressure were only slightly distilled for 16 hours of the MBE distillation time. The impurities with medium high vapor pressure relative to Ga such as Ag, In and Mn showed an overall concentration decrease during entire 16 h, but were not depleted even after 16 h distillation.

The concentration decrease tendency in the distillation from the receding surface in the MBE crucible is compared to the free evaporation as shown in Fig 3.15 for Indium (In). The Indium concentration changed from 1 ppm to ~ 10 ppq (parts per quadrillion) in the free evaporation for 16 h distillation. However, the Indium concentration change was limited to ~ 100 ppb in the evaporation from the receding surface in the MBE crucible for 16 h distillation.

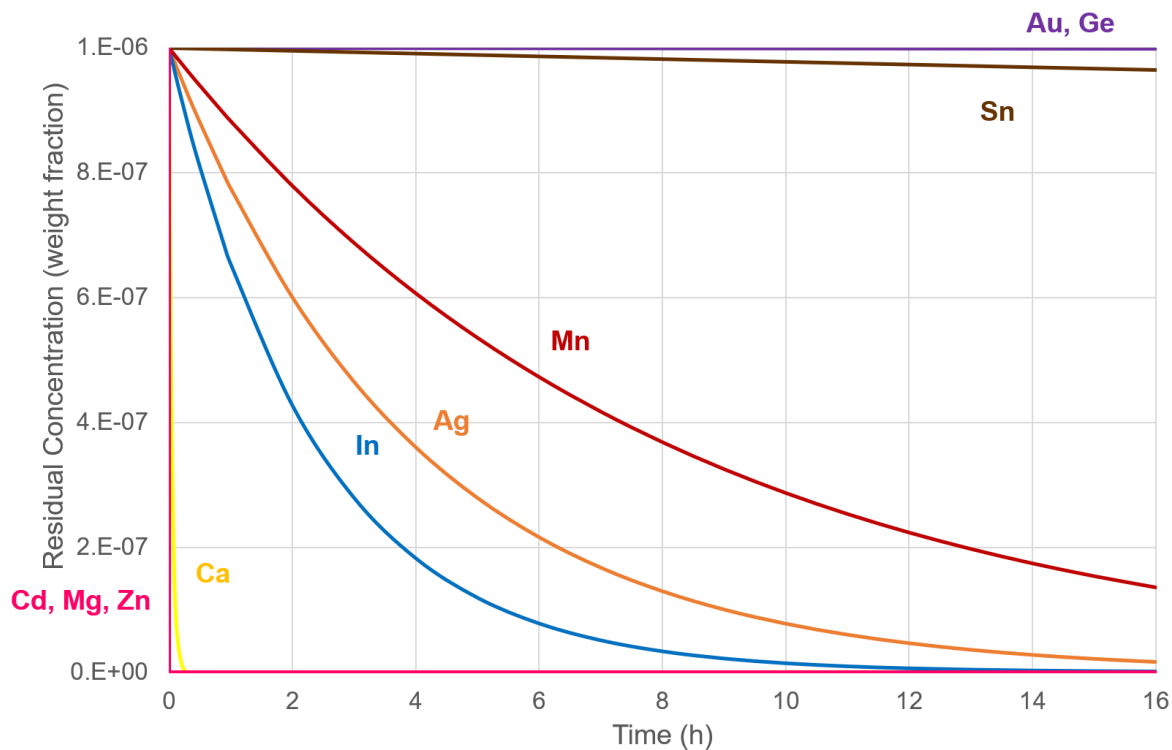


Fig. 3.10 Residual concentrations over distillation time for overall impurities with the 1 ppm initial concentrations distilled at 1360 K

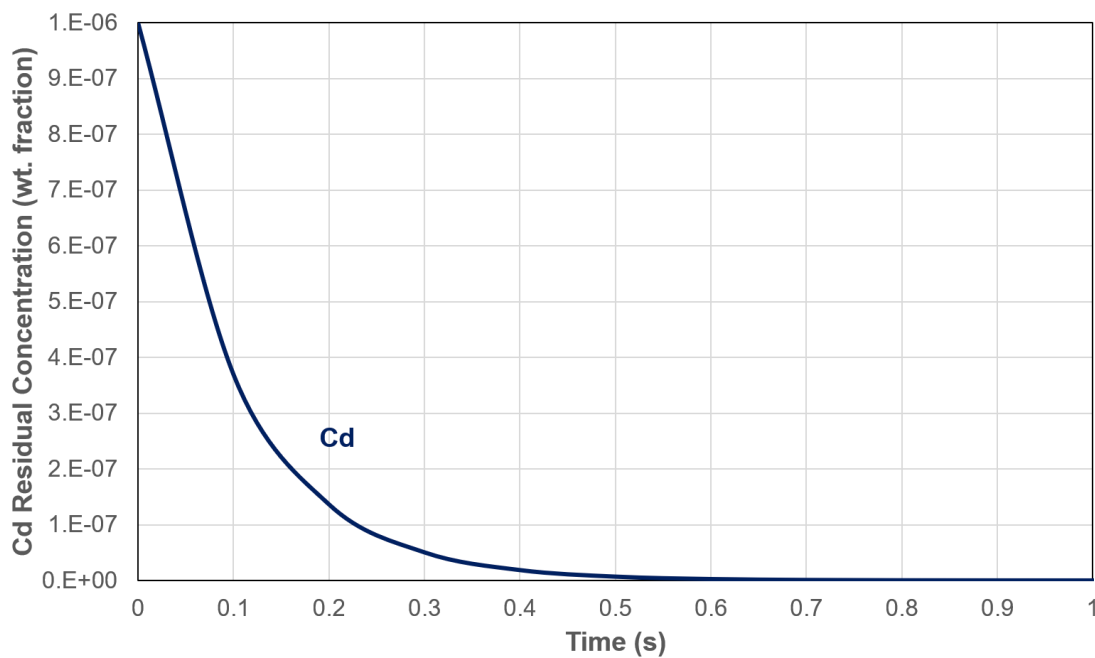


Fig. 3.11 The residual concentrations of 1 ppm Cd after distillation at 1360 K as a function of distillation time

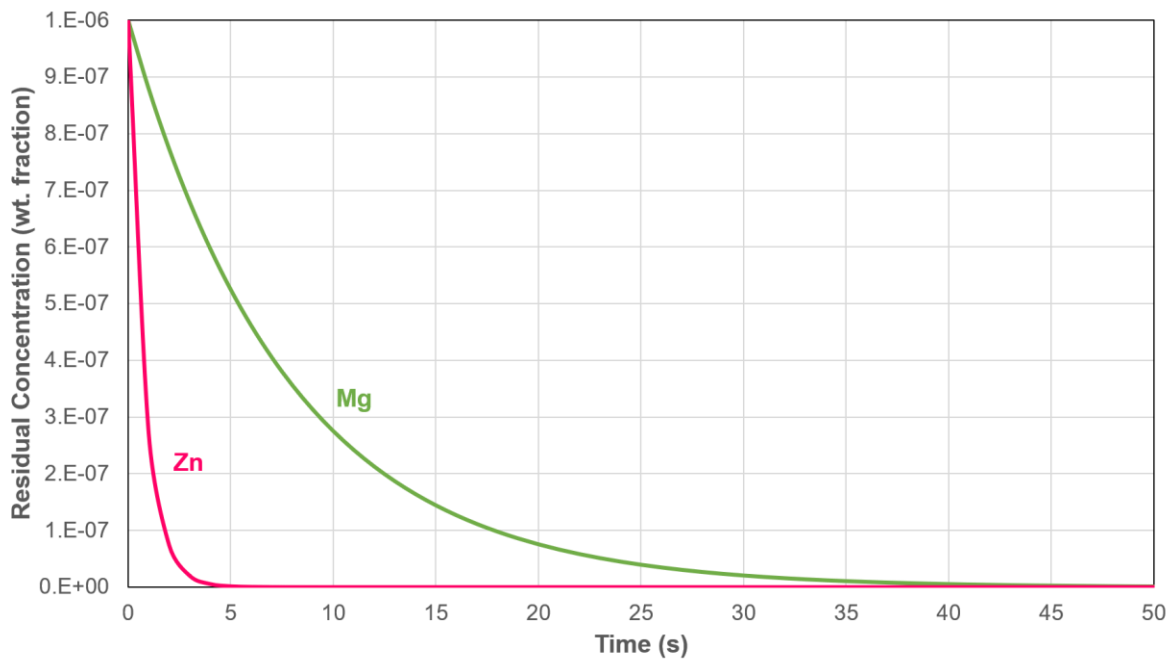


Fig. 3.12 The residual concentrations of 1 ppm Zn and Mg after distillation at 1360 K as a function of distillation time

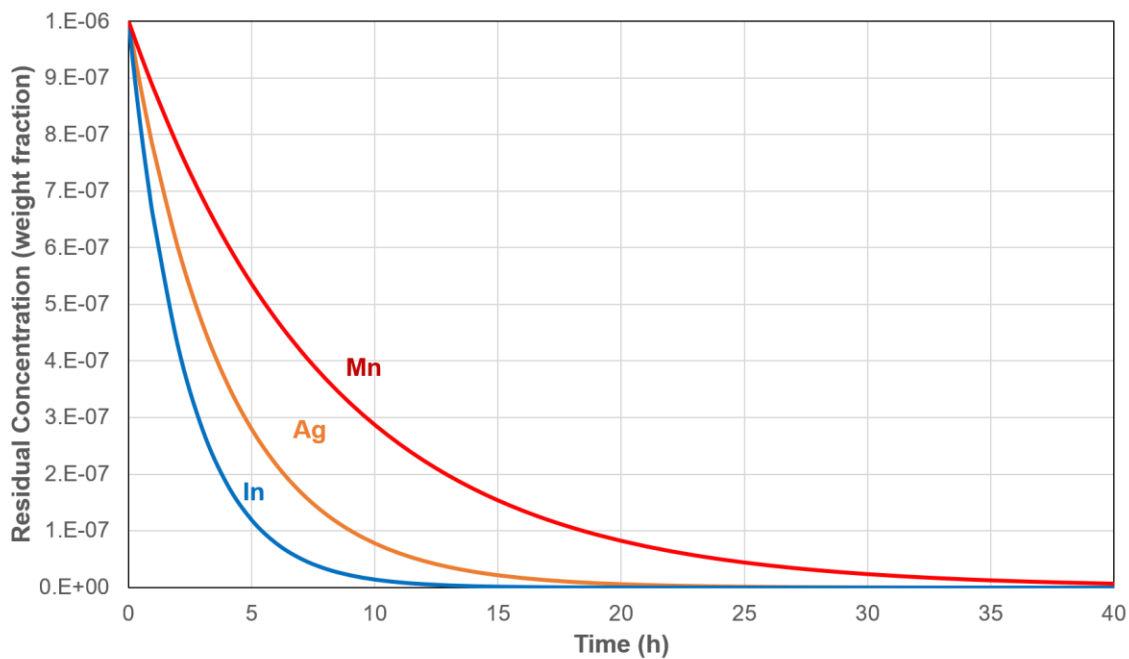


Fig. 3.13 The residual concentrations of 1 ppm Ag, In and Mn after distillation at 1360 K as a function of distillation time

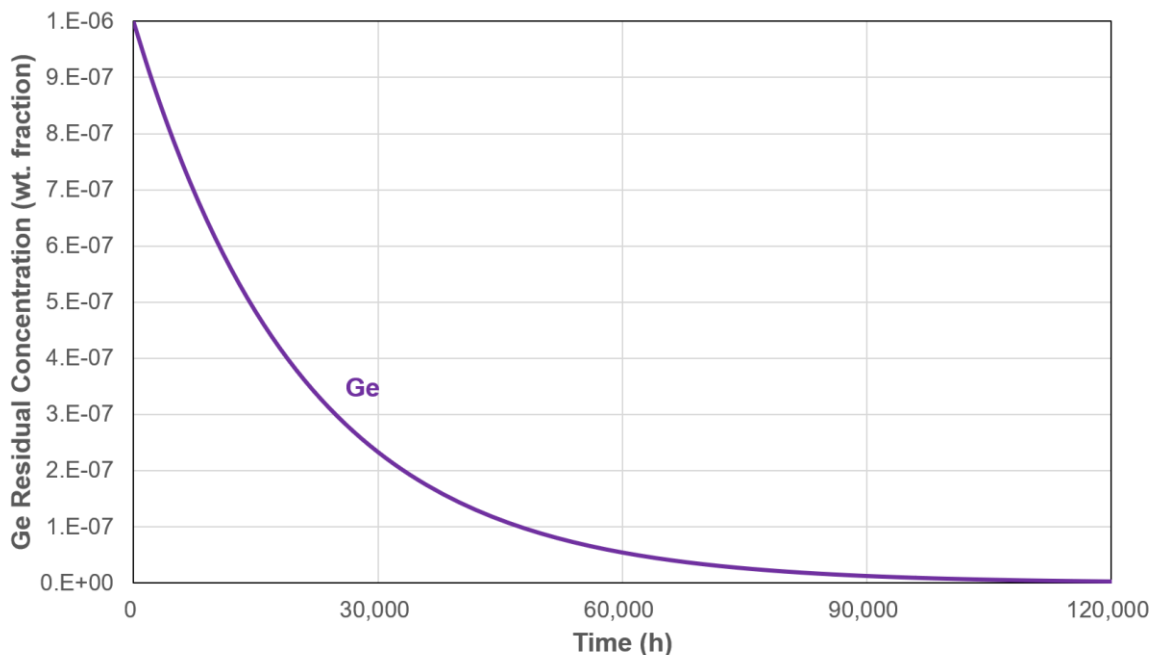


Fig. 3.14 The residual concentrations of 1 ppm Ge after distillation at 1360 K as a function of distillation time

Table 3.3 The time for an impurity concentration to reduce to the half of the initial concentration (1 ppm) at 1360 K from the MBE crucible.

Impurity Element	t(1/2)
Cd	0.07 s
Zn	0.53 s
Mg	5.38 s
Ca	112 s
In	1.63 h
Ag	2.72 h
Mn	5.55 h
Sn	307 h
Au	9000 h
Ge	14200 h

The reported activity coefficients of impurities (Ag, Au, Ge, Mg, Sn, and Zn) in Ga are listed in Table 3.4. While Zn and Sn showed positive deviations from Raoult's law, the other elements showed negative deviations. There was an eccentric aspect on Ag activity lines reported [5].

Overall activity lines of Ag in Ga showed negative deviations. However, the activity of Ag in Ga was changed to positive deviations when the fraction of Ag was close to the mole fraction of 1.

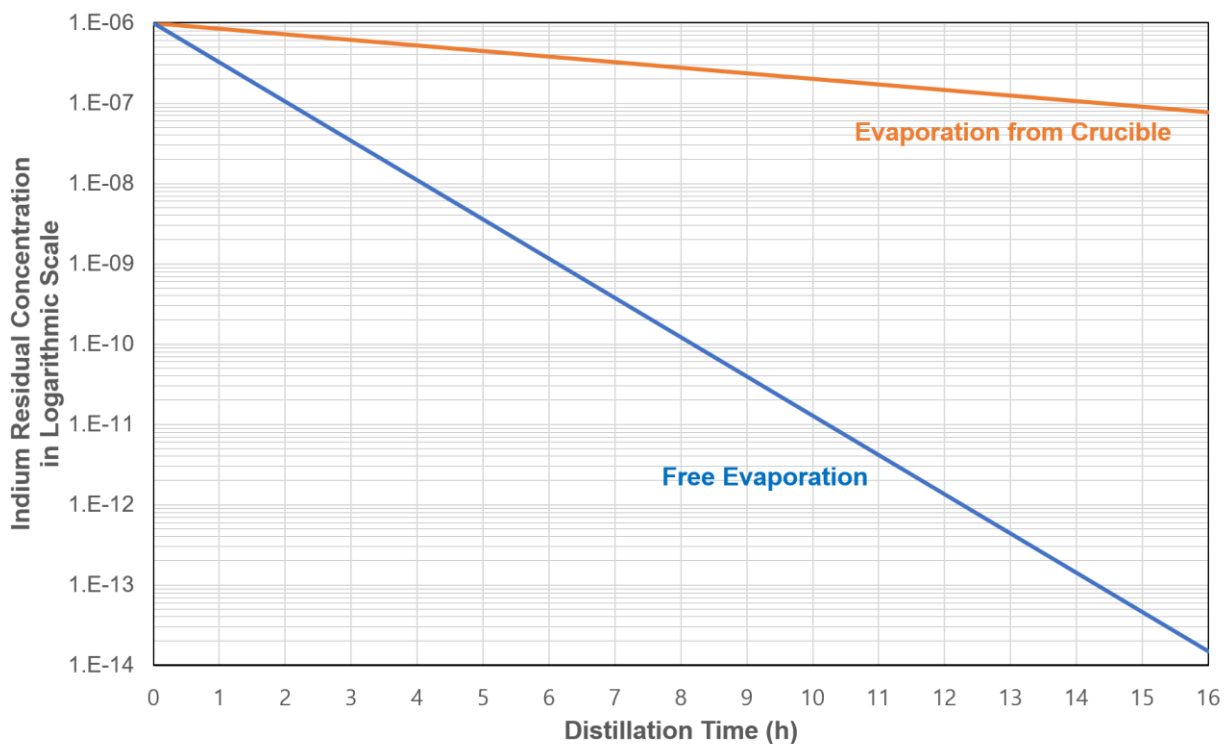


Fig. 3.15 Indium residual concentration change in logarithmic scales with the comparison of free evaporation and evaporation from receding surface in the MBE crucible

Table 3.4 Activity coefficient of impurities in Ga found in literature

Impurity	γ	Measurement conditions			Reference
		Impurity mole fraction	T	Measurement method	
Ag	< 1	Given in graph w/ all ranges of fractions	1300 K	Knudsen Cell Mass Spec	[14]
Au	< 1		1400 K	Thermodynamic calculations	[15]
Ge	1	0.0001	1273 K	Oelsen Calorimetry	[16]
Mg	0.027	~0	923 K	Calorimetry	[17]
Sn	1.54	0.05	1200 K	DTA	[18]
Zn	2.661	0.0372	723 K	DTA	[18]

4. IN-SITU MBE DISTILLATION ANALYSIS BY ICP-MS

Mobility is inversely proportional to impurity concentration in GaAs/AlGaAs 2DEG from theoretical calculations. Among the constituents of GaAs/AlGaAs, Ga is found to be more important to affect mobility from the in-situ MBE distillation. In order to clarify what specific impurities were purified and contributed to the mobility increase, the commercial ultra-pure Ga and recovered Ga after MBE distillation and growth were analyzed by ICP-MS. The ICP-MS is known to have sub-ppt detection limits. However, the detection limit of ICP-MS can be degraded by matrix effects in the analysis of inorganic materials. The Ga matrix separation should be performed in the sample preparation step to reduce the matrix effect for further lower detection limit. The dextran-based resin Sephadex G-25 is known to chemically separate the impurity Ge from Ga. The hydroxide complexes of Ga and Ge are adsorbed on Sephadex G-25 and desorbed into acid depending on pH. Viability of Ge separation from Ga by pH change was evaluated by thermodynamic calculation of the hydrolysis reaction of Ga and Ge. The speciation diagrams showing the distributions of Ga-hydroxide species and Ge-hydroxide species were derived to investigate the optimal pH range to separate impurity Ge from Ga for ICP-MS sample preparation.

4.1 Motivation of Elemental Analysis of Ultra-pure Ga

Previous work [4] showed mobility is dependent on the impurity concentrations in GaAs/AlGaAs 2DEG from theoretical calculations. Hwang and Das Sarma derived the mobility from the scattering rate calculated using Boltzmann transport theory. Since temperature was assumed to be 0 K, acoustic phonon scattering was not considered. The main contributions to scattering were

intentional dopants in the modulation doping layers and unintentional background impurities. When only unintentional background impurities are involved in the scattering, mobility is inversely proportional to the density of unintentional background impurities. When intentional dopants with the density of $10^{11}/\text{cm}^2$ were also involved in the scattering, mobility is limited to 100 million cm^2/Vs at $10^{12}/\text{cm}^3$ under the conditions of the carrier density of $3.0 \times 10^{11}/\text{cm}^2$ and the modulation doping layer of 1200 Å.

The unintentional background impurity density in the AlGaAs/GaAs heterostructures grown by molecular beam epitaxy (MBE) is very small, but limits the charge carrier mobility. There are two ways to improve the electron mobility: one is through the design of heterostructures to minimize the effect of impurities, and the other is to actually reduce the background impurity concentration of source materials [5].

The impurity concentration of the Ga source material has been found to be more important than that of the Al and As [5]. In-situ distillation within the MBE to further purify Ga was shown to result in increased electron mobility measured in the AlGaAs/GaAs heterostructures [5], [6], while the distillation of Al did not show a significant mobility increase. Ga is mainly associated to GaAs channel where electron motion is confined, while Al was only a constituent of AlGaAs barrier.

The starting Ga purity (7N vs. 8N) was also found to affect the final electron mobility attainable during an MBE growth campaign [6]. A purity grade of 7N Ga (100 ppb nominal total impurities) resulted in an electron mobility of $20 \times 10^6 \text{ cm}^2/\text{Vs}$, compared to $35 \times 10^6 \text{ cm}^2/\text{Vs}$ when a starting purity of 8N Ga (10 ppb total impurities) was used. The purity grades of the commercial Ga, 7N

and 8N, were determined by Glow Discharge Mass Spectrometry (GDMS) and the detailed GDMS analysis results for 7N and 8N are listed in Appendix B.

Measuring impurity concentrations in a GaAs thin film is the direct method to analyze the correlation of impurity concentration and mobility. The impurity concentration in GaAs corresponding to the mobility of $35 \times 10^6 \text{ cm}^2/\text{Vs}$ was calculated to be $2 \times 10^{13} \text{ cm}^{-3}$, or $\sim 0.9 \text{ ppb}$. However, there is no existing method to directly measure such low concentration in GaAs. Therefore, the impurity concentrations in the source Ga were instead measured to analyze the relation of impurity concentration to mobility. Also, the impurity concentrations in the remained Ga after in-situ MBE distillation and growth (recovered Ga) were also measured to analyze what specific impurities affect the degradation of mobility with the molecular distillation mechanism, discussed in Chapter 3.

4.2 Analysis initial ultra-pure Ga and residual Ga by ICP-MS

4.2.1 Experimental

Three commercial high-purity Ga lots with nominal purity of 6N (Allusuisse, Zurich, Switzerland) (99.9999 %, 1 ppm), 7N (Alcan, Montreal, Canada) (99.99999 %, 100 ppb) and 8N (Molycorp, Blanding, UT, USA) (99.999999 %, 10 ppb) were analyzed by ICP-MS. In addition, the recovered 7N and 8N Ga after 16 h distillation and 400 growth in the MBE were analyzed by ICP-MS.

The commercial Ga samples were ingots of ~20-g. They were broken into ~0.3-g samples (measured to 0.0001 g) using a hammer on the Ga ingots wrapped in Ta foil. Since Ta was not the target element of analysis, the Ga sample was free from contamination in the detection of target impurity elements of Ge, Sn, Zn, and Fe. The recovered Ga was in the liquid state, hence it was collected by micro-pipette with a polypropylene tip and stored in the acid-cleaned FEP test tube.

The commercial Ga pieces were dissolved in the spectroscopic pure HNO₃ (BHD Aristar Ultra) with 56% concentration in a FEP test tube. Since the recovered Ga was originally collected in the FEP test tube, the recovered Ga sample was dissolved in HNO₃ without transferring from the original container. After initiation by heating in a water bath at 70 °C for 30 min, the samples were sealed with micropara film and stored at room temperature for 4 days, until the Ga was completely dissolved. The totally dissolved Ga in 56% HNO₃ was diluted to 4% HNO₃ concentration with ultrapure water. For standard addition methods, five samples of a blank with 4% HNO₃, a stock solution of Ga dissolved in 4% HNO₃, and standard added samples with different concentrations of analyte standard solution (1 ppb, 2 ppb, 3 ppb) were added to the stock solution. For internal standardization, 1 ppb ⁸⁹Y was added to a blank and stock solution. The internal standard of ⁸⁹Y was selected because ⁸⁹Y is present in Ga in extremely low levels and has no interference with Ga.

All analyses were done in the Purdue Campus-Wide Mass Spectrometry Center using the Element 2 (ThermoFinnigan Bremen, Germany) ICP-MS with argon plasma and double focusing magnetic sector mass analyzer [19]. An Aridus desolvating sample introduction system with T1H nebulizer which reduces the formation of hydrides and oxides was used [20]. The ICP-MS parameters used are the following; RF power was 1200 W, argon flow rate at introduction system was 1 L/min and

accelerating voltage was 2000 V. The medium resolution mode with resolving power of 4000 was used.

The ICP-MS is a mass spectrometer which detects an element based on the mass/charge difference. Consequently, spectral interference can result from isobaric elements, polyatomic species or multiply charged ions with same ratio of mass to charge that are measured together and overlap with analyte signals, resulting in false readings.

Polyatomic species produced from the combination of Ar of the ICP-MS plasma, acid components of H, N and O, and air components such as N, C, O are dominant sources of spectral interference in ICP-MS. The potential interfering polyatomic species in this study are listed in Table 4.1. The Aridus desolvating introduction system can reduce the formation of hydrides and oxides from 30 times to 700 times, compared with a standard pneumatic nebulizer [20]. However, high ArO^+ intensities are measured for 0.1 % HNO_3 . Chlorine-containing species are not included because HCl was not used in this study. Also, the minor isotope ^{64}Ni from the plasma interface focusing cone of the spectrometer interferes with ^{64}Zn analyte. The presence of spectral interference by polyatomic species and isobaric elements was proved by comparison of signal ratios between different isotopes in standard solution and all possible interfering isotopes were excluded in the analysis of the ultrapure Ga.

Spectral interference can be resolved by measuring interference-free isotopes. Possible interfering polyatomic species and isobaric elements were identified and the analyte isotope that does not have interference was used for analysis.

Table 4.1 Possible Polyatomic Species Interfering with Ge, Fe, Sn and Zn for Ga in HNO₃ [21], [22]

Isotope/Abundance (at. %)		Interfering Polyatomic Species
⁷⁰ Ge	20.57	⁴⁰ Ar ¹⁴ N ¹⁶ O ⁺
⁷² Ge	27.45	³⁶ Ar ₂ ⁺ , ⁵⁶ Fe ¹⁶ O ⁺ , ⁴⁰ Ar ¹⁶ O ₂ ⁺
⁷³ Ge	7.75	³⁶ Ar ₂ ¹ H ⁺
⁷⁴ Ge	36.50	³⁶ Ar ³⁸ Ar ⁺ ,
⁷⁶ Ge	7.73	³⁶ Ar ⁴⁰ Ar ⁺ , ³⁸ Ar ³⁸ Ar ⁺
¹¹⁶ Sn	14.54	¹⁰⁰ Ru ¹⁶ O ⁺
¹¹⁸ Sn	24.22	¹⁰² Ru ¹⁶ O ⁺ , ¹⁰² Pd ¹⁶ O ⁺
¹²⁰ Sn	32.58	¹⁰⁴ Ru ¹⁶ O ⁺ , ¹⁰⁴ Pd ¹⁶ O ⁺
⁵⁴ Fe	5.85	⁴⁰ Ar ¹⁴ N, ³⁸ Ar ¹⁵ N ¹ H ⁺ , ³⁶ Ar ¹⁸ O ⁺ , ³⁸ Ar ¹⁶ O ⁺ , ³⁶ Ar ¹⁷ O ¹ H ⁺
⁵⁶ Fe	91.75	⁴⁰ Ar ¹⁶ O ⁺ , ⁴⁰ Ar ¹⁵ N ¹ H ⁺ , ³⁸ Ar ¹⁸ O ⁺ , ³⁸ Ar ¹⁷ O ¹ H ⁺
⁵⁷ Fe	2.12	⁴⁰ Ar ¹⁶ O ¹ H ⁺ ⁴⁰ Ar ¹⁷ O ⁺ , ³⁸ Ar ¹⁸ O ¹ H ⁺
⁵⁸ Fe	0.28	⁴⁰ Ar ¹⁸ O ⁺ , ⁴⁰ Ar ¹⁷ O ¹ H ⁺
⁶⁴ Zn	49.17	³⁶ Ar ¹⁴ N ₂ ⁺
⁶⁶ Zn	27.73	⁵⁰ Ti ¹⁶ O ⁺
⁶⁷ Zn	4.04	N/A
⁶⁸ Zn	18.45	⁴⁰ Ar ¹⁴ N ₂ ⁺
⁷⁰ Zn	0.61	⁴⁰ Ar ¹⁴ N ¹⁶ O ⁺

4.2.2 Results and Discussion

The impurities of Ge, Zn, Sn and Fe were detected to determine the concentration of impurities by ICP-MS. The measured impurity concentrations in Ga samples by ICP-MS are listed in Table 4.2. Although the potential detection limit of the ICP-MS was 10 ppt, the detection limit was degraded to the 1 ~ 10 ppb level. Since the ICP-MS requires the sample of Ga to be dissolved in acid, the potential detection limit of 10 ppt for the concentration of analyte in liquid sample increased to 1 ppb, as the 10 ppt was divided by dissolved Ga concentration in acid (1 wt%), for the concentration of impurity in Ga.

Table 4.2 Concentration of Ge, Zn, Sn and Fe measured in initial and recovered Ga for the grade of 6N, 7N and 8N by ICP-MS [ppb]

Element	6N Ga	7N Ga		8N Ga	
	initial	initial	recovered	initial	recovered
Ge	< 4.1	690	65	15.6	< 7.9
Zn	ND	< 2	< 2	< 2	ND
Sn	Not measured	6.8	Not measured	< 3.2	Not measured
Fe	ND	ND		ND	

ND: not determined due to contamination

4.2.2.1 Germanium Measurement

The signal of ^{72}Ge is interfered by polyatomic species in Table 4.1. Among these, $^{36}\text{Ar}_2^+$ and $^{56}\text{Fe}^{16}\text{O}^+$ cannot be differentiated in medium resolution mode because their mass difference is too small. Although they can be separated in high resolution mode, concentrations at the ppb level cannot be determined because ion transmission efficiency decreases from about 15% to 2% in the high resolution mode [23]. On the other hand, ^{74}Ge is essentially free of spectral interference, as ^{38}Ar of interfering $^{36}\text{Ar}^{38}\text{Ar}^+$ has only a very small natural abundance (0.0632%).

The spectral interference in ^{72}Ge measurement was confirmed from the signal ratio of ^{74}Ge to ^{72}Ge , measured for 6N Ga (Table 4.3). The natural abundance ratio of ^{74}Ge to ^{72}Ge is 1.32. However, higher ion intensity of ^{72}Ge was measured than ^{74}Ge in all samples due to interfering polyatomic species $^{36}\text{Ar}_2^+$ and $^{56}\text{Fe}^{16}\text{O}^+$. Also, ^{74}Ge is the most abundant Ge isotope (36.50 %). Therefore, ^{74}Ge can be measured in general without spectral interference and the concentration of Ge can be derived based on nature abundance.

Table 4.3 Signals of ^{72}Ge and ^{74}Ge in 6N Ga and their ratio

Isotope	Blank [cps]	Stock [cps]	Ge Standard Added Sample			
			0.5 ppb [cps]	1 ppb [cps]	2 ppb [cps]	3 ppb [cps]
^{72}Ge	142	1743	1332	1273	1241	1338
^{74}Ge	63	65	88	211	351	622
$^{74}\text{Ge}/^{72}\text{Ge}$	0.440	0.037	0.066	0.167	0.283	0.465

The Ge concentrations in 6N, 7N and 8N Ga measured by the standard addition method are summarized in Table 4.2. For the 6N Ga, the ^{74}Ge intensity data (Table 4.1) were graphed to determine the Ge concentration of 4.4 ppb. However, it was reported at the detection limit of 4.1 ppb (Table 4.2) because the stock solution signal was insufficient to distinguish from the blank. The detection limit was derived in the usual way by the ratio of three times the standard deviation of the blank to the slope of the graph of ion intensity of analyte versus concentration. Unfortunately, there was no GDMS result of the 6N Ga for comparison.

The concentration of Ge in the initial 7N Ga, determined in the same manner as for 6N, was 690 ppb (Table 4.2). This high value is consistent with the GDMS results (440 ppb), and thus represents an unusually high value of Ge for this particular 7N Ga, which exceeds the nominal total impurity concentration of 100 ppb for 7N; actually this result makes the nominal purity no greater than about 6N3. The concentration of Ge in initial 8N Ga were measured to be 15.6 ppb using standard addition method. This is the first known and lowest value directly measured for Ge concentration in 8N grade Ga by ICP-MS.

In the previous work of Ge detection in high-purity Ga by Xie, Nie and Tang [24], the measured concentration of Ge in a 6N Ga was 39 ppb and in a 7N Ga was below the detection limit reported as 3 ppb. These authors also reported an instrumental detection limit as low as 27 ppt from a blank sample. Since their Ga sample for the ICP-MS measurement contains HCl, the measured concentration could be derived from the interfered signals, as mentioned in the introduction. They did not mention how they determined the slope for the calculation of detection limit of ^{74}Ge from the blank measurement or how they determined the detection limit of Ge in 7N Ga.

The Ge concentration in the recovered Ga of 7N Ga was measured to be 65 ppb. Compared to the initial 7N Ga, which measured at 690 ppb, the amount of Ge lost was 64 μg , considering the Ga loss from 100 g to 75 g. The Ge concentration of the recovered Ga from 8N grade measured to be below the detection limit of 7.9 ppb. Compared to the initial 8N Ga, the Ge concentration also measurably decreased, with the Ge loss of more than 1 μg , considering 8N Ga loss of 29.6 g during MBE distillation and growth. The significant Ge loss is an unexpected result, which cannot occur by the molecular distillation mechanism, as will be further discussed in Chapter 5.

From the above results, the concentration of Ge in high-purity Ga can be determined by ICP-MS when the concentration is higher than ~ 10 ppb, which is significantly higher than sub-ppt potential detection limit in the absence of matrix effects and dilution necessary in the sample preparation of metals. Determining the actual impurity concentration (above the detection limit) at these low levels in ultra-pure Ga is a challenging problem due to the dilemma between the need for high TDS to satisfy the instrument sensitivity, and associated significant signal suppression.

4.2.2.2 Tin Measurement

The Sn concentration was measured in the 8N Ga by standard addition method and 7N Ga by internal standardization. All Sn isotopes listed in Table 4.1 are expected to be free of spectral interference; possible interference from Ru- or Pd-containing species are unlikely because low concentrations of Ru and Pd are present in Ga and the measurement environment. The concentration of Sn in 8N Ga was determined by the most abundant Sn isotope, ^{120}Sn (32.58 %). The concentration of dissolved Ga in HNO_3 was 0.19 % for the 8N Ga sample. Similar to the detection of ^{74}Ge in 8N Ga, ^{120}Sn ion intensity of the blank was higher than that of the stock solution and the ion intensity of the stock solution was lower than signal detection limit in the measurement of 8N Ga. Consequently, Sn could be only estimated as below the detection limit or < 3.2 ppb, determined in the same methods as for Ge. The Sn concentration reported for the GDMS analysis was also given as below the detection limit of 4 ppb, similar to that of the detection limit for the present ICP-MS results.

The Sn concentration in 8N Ga was determined to be 6.8 ppb by internal standardization. The concentrations of Sn in the recovered Ga of 7N and 8N grades were not measured in internal standardization due to the ICP-MS maintenance problem.

4.2.2.3 Zinc Measurement

The most abundant isotope of Zn is ^{64}Zn . The polyatomic species, such as $^{36}\text{Ar}^{14}\text{N}_2^+$, possibly interfering with ^{64}Zn , do not give a dominant effect for signal interference due to the low occurrence of ^{36}Ar . However, though not a common isotope, ^{64}Ni can be picked up from the Ni skimmer cones. Therefore, ^{64}Zn is not free from spectral interference. The next most abundant Zn isotope of ^{66}Zn is essentially free of spectral interference. Titanium (Table 4.1) is not a common environmental contaminant or impurity in Ga.

The measured ion intensities of ^{66}Zn in 7N and 8N Ga using the standard addition method are listed in Table 4.4. The results were expected to increase as the concentration of Zn added increases. However, the significant signal drops of 50 times for 7N and 4 times for 8N Ga were shown in the 1 ppb sample for both 7N and 8N Ga, having higher concentrations of Zn than the stock solutions. The dropped signals rose again in the 2 ppb sample. Then the signal in the 3 ppb sample dropped 4 times again for 8N Ga and increased only slightly for the 7N Ga.

These results were are most likely due to contamination from previously measured samples (memory effect) in high total dissolved solids sample (0.1 - 0.2 % TDS), much higher than nominal TDS of 0.01 %. Zinc is well contaminated and hence could be more transferrable to deposited Ga TDS. Considerable amounts of Zn ions may not have been delivered to the mass analyzer and may

have stayed with deposited Ga TDS, thus causing the significant signal drop in the 1 ppb sample. As the ICP-MS was washed out by HNO₃ between samples and the 2 ppb sample was loaded, well contaminated Zn ion could have been transferred to the 2 ppb sample, causing the signal increase in the 2 ppb sample.

Table 4.4 Results of ⁶⁶Zn detection in 7N and 8N Ga samples by standard addition method

Ga Grade	Blank [cps]	Stock [cps]	Zn Standard Added Sample		
			1 ppb [cps]	2 ppb [cps]	3 ppb [cps]
7N	37	926	2	755	807
8N	238	7726	1873	9023	1906

On the other hand, the measurement of the Zn standard solution itself, with essentially no TDS compared to the Ga sample, showed consistent signal increase with increasing concentration from 0.2 ppb to 1 ppb, unlike the data in Table 4.4, which contains high TDS. It was linear to a very good correlation ($R^2 = 0.9983$). This confirms the Zn signal fluctuation tendency in Table 4.4 is due to the memory effect that occurs in high TDS samples.

To test if the Zn accumulation with high TDS samples caused the signal fluctuation, washout time between samples was increased from 2 min to 3 min in the measurement of the same 7N Ga samples. The ⁶⁶Zn was measured in four different, but equivalent, samples to clarify the hypothesis that Zn accumulation from previous sample affects the next sample measurement in high TDS samples. As shown in Table 4.5, with more washout time between samples the signal fluctuation of ⁶⁶Zn was greatly reduced. This result is consistent with accumulation of Zn from the high TDS Ga sample causing signal fluctuation, because increased washout time contributed to transmit deposited ions, not to interfere with the signal in next sample.

Table 4.5 Detection of ^{66}Zn in 7N Ga in the increased wash-out time

Isotope	Blank	Stock 1 of 7N Ga	Stock 2 of 7N Ga	Stock 2 of 7N Ga	Stock 2 of 7N Ga
^{66}Zn	381	928	771	724	831

Increasing washout time helps to reduce the degree of signal fluctuation, but degrades ICP-MS capability and stability. Therefore, the internal standard method with ^{89}Y was used for Zn analysis of the high-TDS sample without increased washout time. In the internal standard method, fewer high-TDS samples are needed (only 1 high-TDS stock solution), compared to 4 high-TDS samples required for the standard addition method. Fewer samples reduces the signal fluctuation.

The signal ratio of ^{66}Zn and ^{89}Y was converted to determine the Zn concentration. The matrix effect was compensated by comparing ^{89}Y signals measured in the blank and stock solution. Since both ion intensities of ^{66}Zn in 7N and 8N Ga measured in the stock solution were below the signal detection limit, the concentration of Zn was reported at the detection limit of 2 ppb for initial 7N and 8N Ga. The Zn concentration in the recovered 7N Ga was also below the detection limit of 2 ppb. The concentration of Zn in the recovered 8N Ga was not determined because the sample of recovered 8N Ga was severely contaminated due to a storage problem. The slope for the detection limit was derived from the signal of 1 ppb ^{89}Y . The GDMS results for initial 7N and 8N Ga also reached the detection limit of 0.5 ppb for 7N and 2 ppb for 8N Ga.

4.2.2.4 Iron Measurement

Iron is very challenging for ICP-MS of ultra-pure Ga due to environmental contamination and the fact that there is no isotope free from spectral interference. The most dominant isotope, ^{56}Fe (91.75%), is interfered by polyatomic species of $^{40}\text{Ar}^{16}\text{O}^+$, $^{40}\text{Ar}^{15}\text{N}^1\text{H}^+$, $^{38}\text{Ar}^{18}\text{O}^+$, $^{38}\text{Ar}^{17}\text{O}^1\text{H}^+$ (Table 4.1). However, the mass difference of these species and ^{56}Fe in principle can be differentiated in the medium resolution mode of the ICP-MS. Hence, ^{56}Fe in 6N and 7N Ga was measured by ICP-MS using the standard addition method. As shown in Table 4.6, the ion intensity of ^{56}Fe did not show linearity with standard additions. This result is most likely from the usual sensitivity to environmental contamination, which is very difficult to control. In addition, the radical signal fluctuation was likely caused by degraded ion transmission due to previous sample deposition, as occurred in Zn measurement.

Table 4.6 Results of ^{56}Fe detection in 6N and 7N Ga by standard addition method

Isotope	Blank [cps]	Stock [cps]	Fe Standard Added Sample			
			0.5 ppb [cps]	1 ppb [cps]	2 ppb [cps]	3 ppb [cps]
6N	524	3268	814	3535	8.50×10^4	6387
7N	899	1918	-	5247	1326	1826

The ^{89}Y internal standard used in the measurement of Zn could not be used for Fe because it contains a significant amount of Fe, as measured directly on the blank sample as estimated from the ^{89}Y measurement. Under the assumption of 1 ppb Fe concentration in Ga, the concentration of ^{56}Fe in HNO_3 (stock solution) is about 0.01 ppb for 1% TDS. However, the ^{56}Fe concentration in

the blank was estimated for 7N Ga to be about 0.01 ppb, which thus overwhelms the concentration of Fe in the stock solution.

Although problems with Fe measurement are usually attributed to contamination, spectral interference can also contribute in ultra-low impurity measurements as in the present study. The Element 2 spectrometer, with a double focusing magnetic sector mass analyzer, samples the data within 150 % of mass difference and analyte peak width as the full width at 10 % of maximum. The mass difference is defined by the resolving power (4000 for medium resolution mode) [25]. The sampled $^{40}\text{Ar}^{16}\text{O}^+$ in the 150 % mass difference range should have been resolved from the overlapping ^{56}Fe in sampling the peak width as the full width at 10 % of maximum in the medium resolution mode. However, if $^{40}\text{Ar}^{16}\text{O}^+$ is dominant, parts of $^{40}\text{Ar}^{16}\text{O}^+$ can be measured as ^{56}Fe in the tail of peak sampling.

Iron was not measured in the analysis of recovered Ga because the contamination problem disturbing the concentration determination was already found in the analysis of the commercial Ga.

4.2.2.5 Matrix Effect Investigation

As high a concentration of dissolved Ga in acid as possible is preferred to obtain lower the detection limit. However, the samples with a high concentration of Ga do not always show high impurity signal response. When total dissolved solids (TDS) is greater than 0.01 wt%, matrix effects are present in ICP-MS [26], in which particles in sample are deposited on the nebulizer or

orifice of the spectrometer, disturbing ion transmission from the plasma to mass analyzer and causing overall signal suppression.

To investigate the signal depression level by a matrix effect and estimate optimal concentration of Ga in HNO₃, signal response was measured over the range which can determine the impurity concentration of 1 ~ 10 ppb. Fig.4.1a illustrates the variation of ion intensity of ⁷²Ge and ⁷⁴Ge with total dissolved solids (TDS) of 8N Ga. The analyte signals should have increased with increasing TDS, but reached a plateau above 0.05 wt% TDS due to a matrix effect. Consequently, the matrix effect is confirmed. The decreased signal tendency due to matrix effect is also shown in the ⁴⁰Ar⁴⁰Ar⁺ (Ar background) ion intensity decreasing with increasing Ga concentration.

Since ion intensities of all impurity elements are depressed in a sample having a high concentration matrix, an additionally added element that is independent of Ga and impurities of Ga also can be an indicator of matrix-induced interference. Fig 4.1b shows the variation of ion intensity of ⁷⁴Ge in 7N Ga in different TDS with those of added ⁸⁹Y and ⁴⁰Ar⁴⁰Ar⁺. The decreased ion intensity of both ⁸⁹Y (1 ppb added to each TDS sample) and ⁴⁰Ar⁴⁰Ar⁺ again confirms the matrix effect. Although the ion intensity of ⁷⁴Ge did not reach a plateau, as in the 8N Ga, it increased only slightly, much less than what it should have, in the absence of the matrix effect. These results show the 7N Ga contains more Ge than the 8N but both Ge signals are significantly suppressed due to the matrix effect.

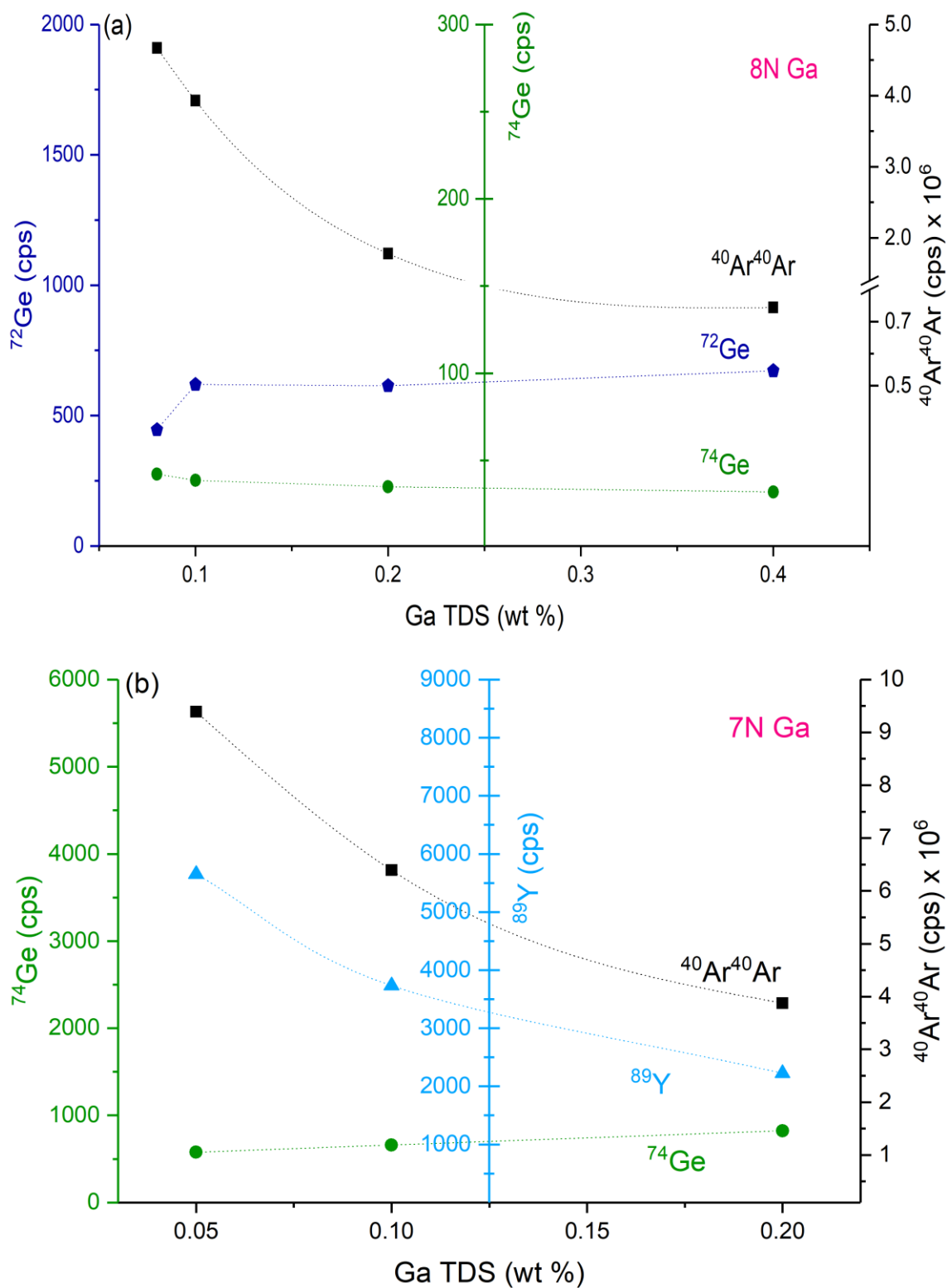


Fig. 4.1 Germanium signal comparison for 7N and 8N Ga in HNO_3 at different total dissolved solids (a) Ion intensity of ^{72}Ge , ^{74}Ge and $^{40}\text{Ar}^{40}\text{Ar}^+$ versus TDS for 8N Ga. (b) Ion intensity of ^{74}Ge , ^{89}Y and $^{40}\text{Ar}^{40}\text{Ar}^+$ versus TDS for 7N Ga.

Tan and Horlick discussed the presence of a Na ion matrix effect in the detection of Sc, Li, Al, Co, Ba, Pb and Tl impurities in a Na sample of as small as 0.01 wt % TDS, even much lower than this study [27]. However, a decreased signal tendency with increasing TDS was not clearly observed as in the present study.

Fig 4.2 shows the variation of impurity Sn signal with increasing TDS of the 8N Ga and 7N Ga with those of added ^{89}Y and $^{40}\text{Ar}^{40}\text{Ar}^+$ signals. Both the signals of $^{40}\text{Ar}^{40}\text{Ar}^+$ and ^{89}Y decrease with increasing Ga TDS, as in Ge analysis for 7N Ga with added ^{89}Y (Fig 4.1b), again clearly illustrating the matrix effect. For the 8N Ga, the Sn signal (Fig 4.2a) is greater than Ge signal (separate analyses, and measured to 0.4 % TDS) (Fig 4.1a), and the Sn signal shows more suppression at higher TDS than Ge signal. For the 7N Ga, the Sn signal Fig 4.2b) is smaller than Ge signal (Fig 4.1b) and shows more suppression.

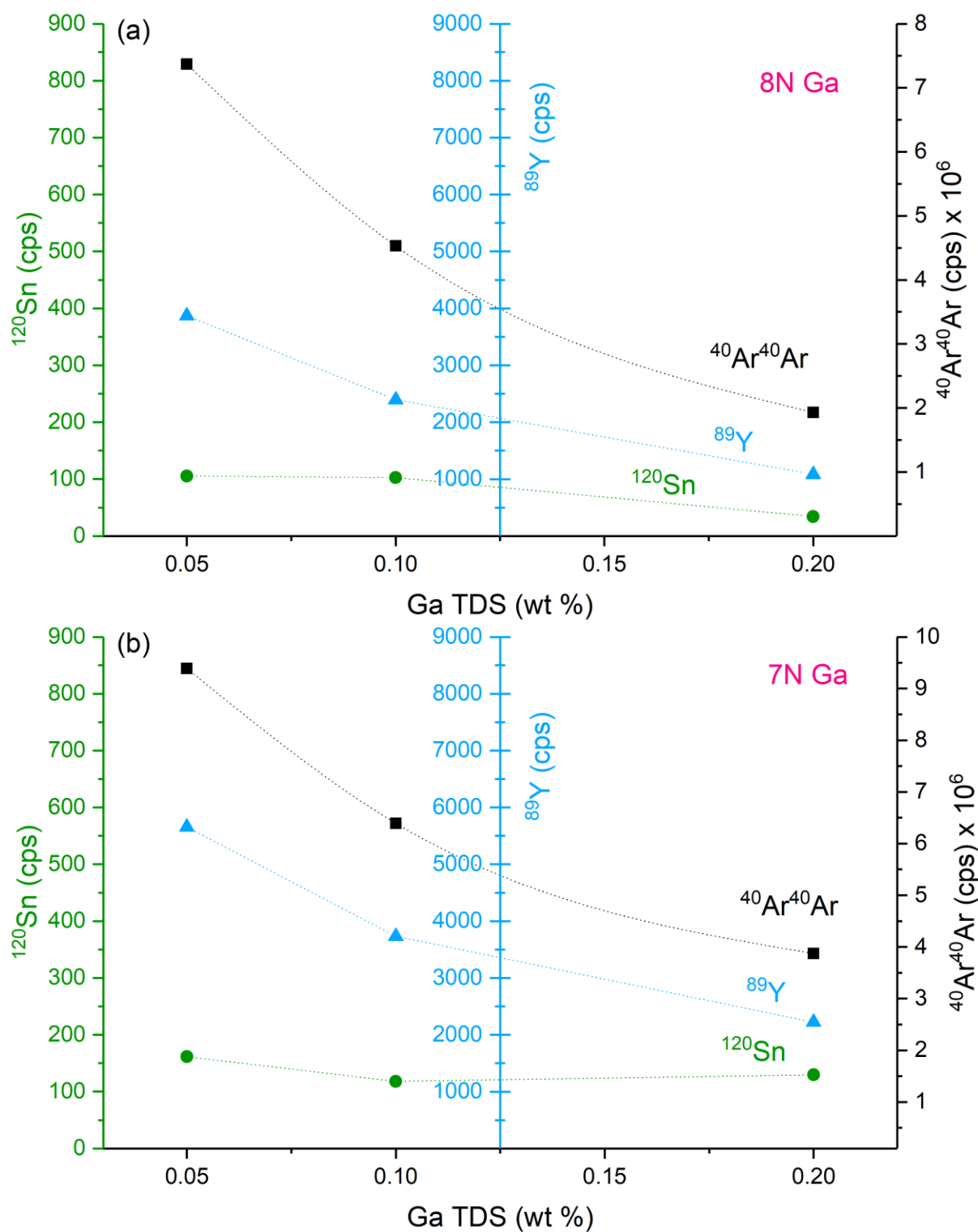


Fig. 4.2 ¹²⁰Sn signal comparison in different concentration of dissolved Ga in HNO₃, comparing to ⁸⁹Y and ⁴⁰Ar⁴⁰Ar⁺ variance. (a) Ion intensity of ¹²⁰Sn, ⁸⁹Y and ⁴⁰Ar⁴⁰Ar⁺ versus TDS for 8N Ga. (b) Ion intensity of ¹²⁰Sn, ⁸⁹Y and ⁴⁰Ar⁴⁰Ar⁺ versus TDS for 7N Ga

4.3 Implications of ICP-MS Results and Background of Chemical Separation of Ga

As pointed out in the previous section, the matrix effect present in the analysis of highly concentrated samples degraded the potential ICP-MS detection limit of 10 ppt to the 1 ppb level. As shown in the matrix effect investigation, the ICP-MS signal did not proportionally increase as concentration increased despite the higher amount of Ga in the sample. Moreover, the high TDS rather causes malfunction of the ICP-MS. Consequently, highly concentrated Ga causing the matrix effect should be decreased but there is a dilemma, as low Ga concentration does not provide enough signals ICP-MS can detect. Therefore, chemical separation of matrix Ga in the sample is recommended to achieve the full potential of the ICP-MS by removing the matrix effect.

The method of separation of Ga is different depending on impurity type. Consequently, the separation of Ga for Ge detection will be first tried, because Ge is important impurity in the MBE growth. Since Ge is a major dopant element, Ge likely plays a key role to degrade mobility in GaAs. Moreover, Si which is chemically similar and same type of donor as Ge in GaAs, is used for an intentional dopant in the GaAs/AlGaAs quantum well. If Ge is present in source Ga and transferred to GaAs during deposition, Ge would disturb the behavior of Si in addition to degrading mobility as a background impurity. Above all, Ge is not sensitive to environmental contamination, so that the separation of Ga from Ge is easy to control, establishing the Ga separation methodology for the alleviation of the matrix effect. High concentrations of Ge found in 7N Ga also can be a barometer to confirm the degree of relieved matrix effect after Ga separation.

The separation of Ga from Ge is relatively difficult compared to other impurities, because Ga and Ge are chemically similar. Hence, only a couple of methods had been reported to separate Ga and

Ge. Rafaeloff used organic solvent extraction by methyl ethyl ketone (MEK) to separate Ga from Ge and other group III elements [28]. Methyl ethyl ketone is added to the Ga sample dissolved in HNO_3 and H_2SO_4 and mechanically mixed. Then an aqueous phase and an organic phase immiscible are produced. Germanium is stripped into aqueous phase and Ga is stripped into organic phase. The extracted percentage of Ga was from 84.3 % to 99.99 %, depending on the concentration of acids such as HCl and H_2SO_4 . The Ge of 0.08 % was coextracted with Ga. This method, which requires the evaporation of strong acid mixture, had a safety issue as a bench top experiment in the cleanroom. Therefore, another method needed to be developed.

Fitzsimmons and Mausner used a Sephadex G-25 column to separate Ge from Ga [29]. The objective solution for separation containing 100 μg of Ga, Ge and Zn in HCl was adjusted to pH 13.0 with NaOH and added into the Sephadex G-25. Gallium was eluted with 0.1 M NaOH and Ge was eluted with 0.1 M HCl. The column was rinsed with water between the elution of Ga and Ge. The extracted percentage of Ga was 98 % with coextraction of 6.2% Ge in the 0.1 M NaOH elution. Germanium of 92 % was extracted with coelution of 2.3 % Ga.

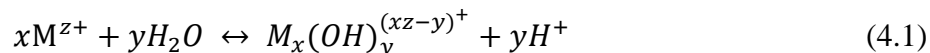
In a different study by Fitzsimmons and Mausner [30], the sample solution containing Ga, Ge, Co and Zn in HCl was adjusted to pH 12.5 with $\text{Na}_3\text{C}_6\text{H}_5\text{O}_7$ and NaOH. The eluents for Ge and Ga extraction were the same as that in their previous study, but the column was rinsed using both $\text{Na}_3\text{C}_6\text{H}_5\text{O}_7$ and water between elution. The percentage of eluted Ge was reported as a function of pH from 11 to 13.5 of the sample solution. The maximum percentage of eluted Ge was 96 % at pH 13. At pH 12, 90.8 % of Ge was eluted.

Harada and Tarutani extracted Ge in rocks using the Sephadex G-25 [31]. Germanium was preconcentrated from carbonate solution and desorbed into 0.1 M HNO₃, maintaining the ionic strength to 0.1 M with NaCl. The pH of the sample solution was adjusted to pH 12 by NaOH, and HCl was used to elute Ge. The degree of Ge extracted was evaluated by comparing the concentration of Ge adsorbed with that found in a standard rock sample. The degree of Ge adsorbed was smaller than 50 % of Ge found in all samples.

As found in the previous studies, the separation of Ge and Ga by Sephadex G-25 is influenced by pH. This is because Ga and Ge species with different solubility are produced in different percentages from the hydrolysis reaction, depending on pH [32]. Consequently, an understanding of the hydrolysis reaction of Ga and Ge, the produced Ga and Ge species distribution, and the associated separation mechanism are required to establish experimental parameters for Ga extraction. Although experimental methodology and results of Ga extracted are informed by previous studies, the experimental parameters and conditions in the previous studies are not applicable to the ICP-MS sample due to spectral interference. For example, the chloride ions in a sample solution can cause interference in the measurement of Ge by ICP-MS. Therefore, thermodynamic study for the Ga and Ge hydrolysis reactions was performed in the following section. The effect of ionic strength in the sample solution and medium concentration was evaluated. The distribution of Ga and Ge hydroxide compounds for an ideal ICP-MS sample condition for pure-Ga analysis were derived by thermodynamic calculations and the pH range over which Ge can be separated from Ga was determined.

4.4 Thermodynamic study of Ga separation by Sephadex G-25

The general hydrolysis reaction for metal cation M^{z+} is defined by [32], [33],



The corresponding equilibrium quotient of Q_{xy} , which is the concentration ratio of products to reactant, is defined by equation (4.2).

$$\text{Log}Q_{xy} = \text{Log}K_{xy} + a \frac{\sqrt{I}}{1+\sqrt{I}} + bm_x \quad (4.2)$$

Here, K_{xy} is the equilibrium constant of hydrolysis reaction, I is the ionic strength in aqueous solution (HNO_3 in this study), and m_x is the medium concentration. The medium (e.g. NaCl) does not participate as a reactant in the hydrolysis reaction, but it interacts with ions in the aqueous solution and contributes to the equilibrium quotient [33]. The coefficient a is the product of the change in charges squared for the reaction, and the Debye-Hückel limiting slope and the coefficient b are related to the interaction coefficient summed over the formation reaction for a hydrolysis product.

The speciation diagram, which shows the distribution of hydrolysis species as a function of pH, is derived from thermodynamics calculation using the relation between free energy of formation and the equilibrium quotient in equation (4.2). There are four hydroxide compounds mononuclear species formed from Ga^{3+} . Germanium(IV) with the +4-oxidation state occurs in $Ge(OH)_4$, resulting in three hydrolysis reactions. The equilibrium constant and coefficients to obtain the equilibrium quotient for each reaction of Ga and Ge hydrolysis possible are listed in Table 4.7 and Table 4.8, respectively. The species $Ge_8O_{16}(OH)_3^{3-}$ from $Ge(OH)_4$ was excluded in the analysis of

species distribution for Ge hydrolysis because it is found at the initial Ge concentration greater than 0.005 M [32]. The initial Ge concentration before the hydrolysis reaction in this study would be smaller than 1 ppm, considering the 1 ppm total nominal impurity concentration of 6N Ga.

Table 4.7 Gallium hydrolysis reaction at 25 °C [9]

Reaction	Log K_{xy}	a	b
$\text{Ga}^{3+} + \text{H}_2\text{O} \leftrightarrow \text{GaOH}^{2+} + \text{H}^+$	-2.6	-2.044	0.4
$\text{Ga}^{3+} + 2\text{H}_2\text{O} \leftrightarrow \text{Ga}(\text{OH})_2^+ + 2\text{H}^+$	-5.9	-3.066	0.4
$\text{Ga}^{3+} + 3\text{H}_2\text{O} \leftrightarrow \text{Ga}(\text{OH})_3 + 3\text{H}^+$	-10.3	-3.066	0.2
$\text{Ga}^{3+} + 4\text{H}_2\text{O} \leftrightarrow \text{Ga}(\text{OH})_4^- + 4\text{H}^+$	-16.6	-2.044	0.1

Table 4.8 Germanium hydrolysis reaction at 25 °C [9]

Reaction	Log K_{xy}	a	b
$\text{Ge}(\text{OH})_4 \leftrightarrow \text{GeO}(\text{OH})_3^- + \text{H}^+$	-9.31	1.022	-0.2
$\text{Ge}(\text{OH})_4 \leftrightarrow \text{GeO}_2(\text{OH})_2^{2-} + 2\text{H}^+$	-21.9	3.066	-0.4
$\text{Ge}(\text{OH})_4 \leftrightarrow \text{Ge}_8\text{O}_{16}(\text{OH})_3^{3-} + 3\text{H}^+$	-14.24	6.132	0.2

The ICP-MS samples were prepared to 4 % HNO_3 . The concentration of HNO_3 is directly connected to the ionic strength. The condition of the target for the hydrolysis reaction to derive speciation diagrams for Ga and Ge is the sample solution containing 10,000 ppm Ga and 100 ppb Ge in 4% (~ 0.64 M) HNO_3 . The pH for separation is adjusted with NaOH. The speciation diagrams for Ga and Ge hydrolysis were derived using parameters listed in Table 4.7 and Table 4.8. The series of nonlinear equations obtained from the relation of free energy of formation and equilibrium constant used to calculate the fraction of hydrolysis species for Ga and Ge as a function of pH were solved by Newton's method.

The relative activity of the hydrolysis reaction for each species can be estimated by the hydrolysis constant. The hydrolysis constants for each reaction of Ga and Ge are plotted as a function of ionic

strength in Fig.4.3 and Fig.4.4. Among four different mononuclear hydrolyses of GaOH^{2+} , Ga(OH)_2^+ , Ga(OH)_3 , Ga(OH)_4^- produced from Ga^{3+} , two species of interest are derived. Cases both with the presence and absence of 0.1 M medium were represented in all reactions.

Overall, the medium addition (0.1 M in the aqueous solution) does not significantly influence the hydrolysis constants, and thus does not increase the formation of hydrolyses. The effect of ionic strength change on the hydrolysis reaction is much greater than that of medium addition. While the Ga hydrolysis reaction increases, the Ge hydrolysis reaction decreases as ionic strength increases. This result shows the hydrolysis of Ga reacts opposite to the hydrolysis of Ge for mole concentration increase in the aqueous solution.

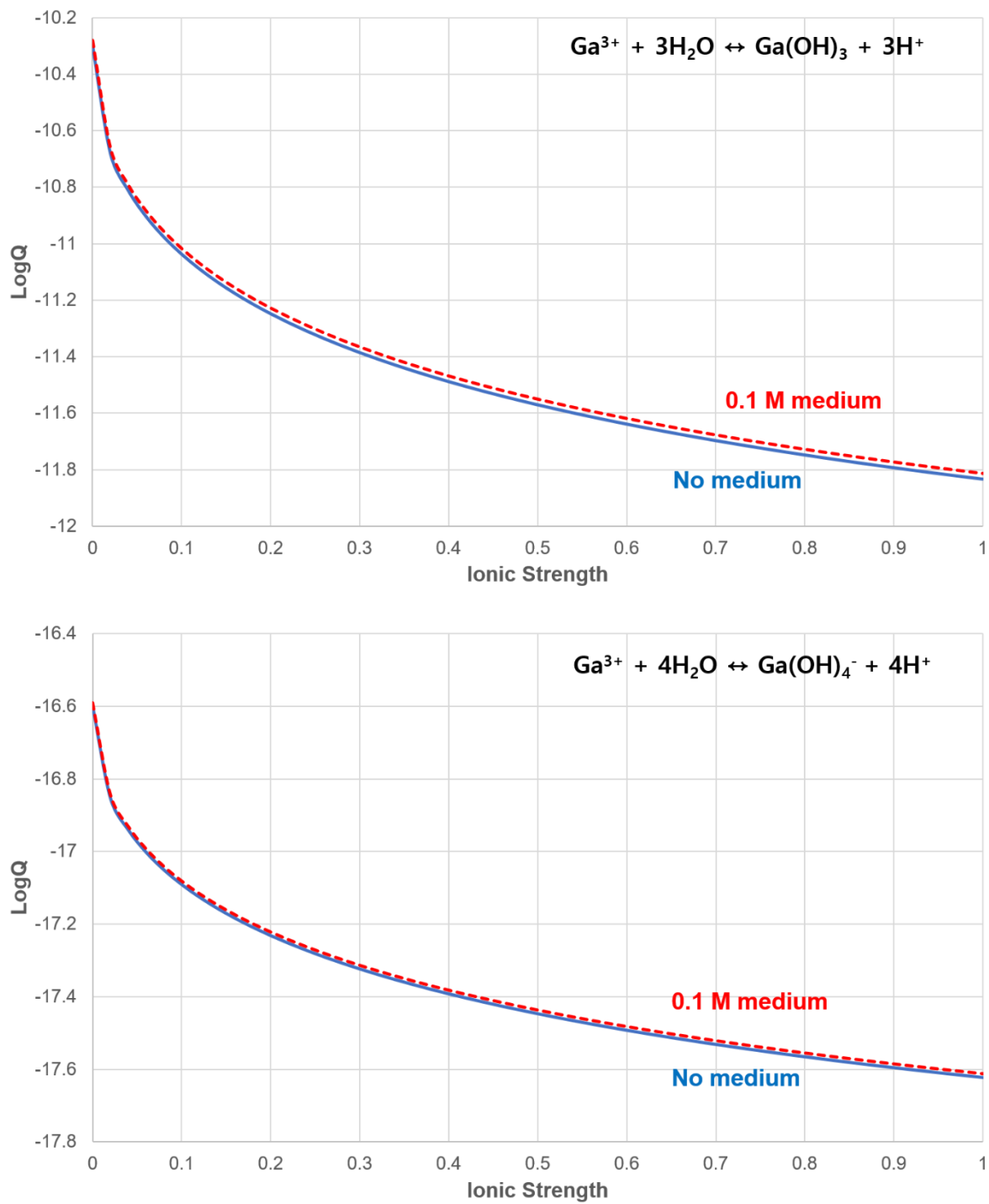


Fig. 4.3 Hydrolysis constant (quotient) of Ga-hydroxide species $\text{Ga}(\text{OH})_3$ (top) and $\text{Ga}(\text{OH})_4^-$ (bottom) as a function of ionic strength with and without 0.1 M medium

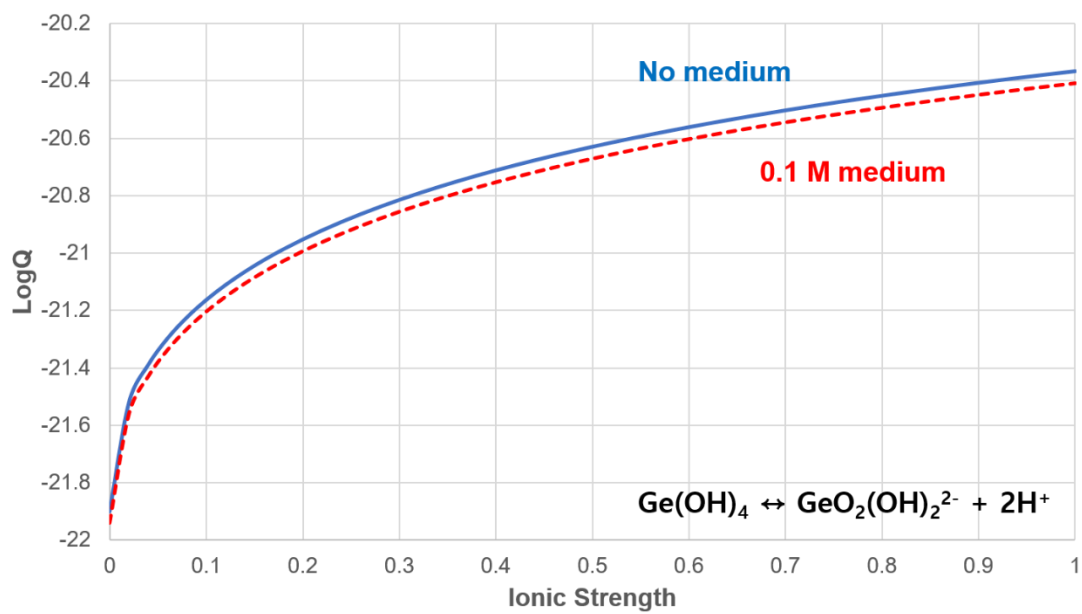
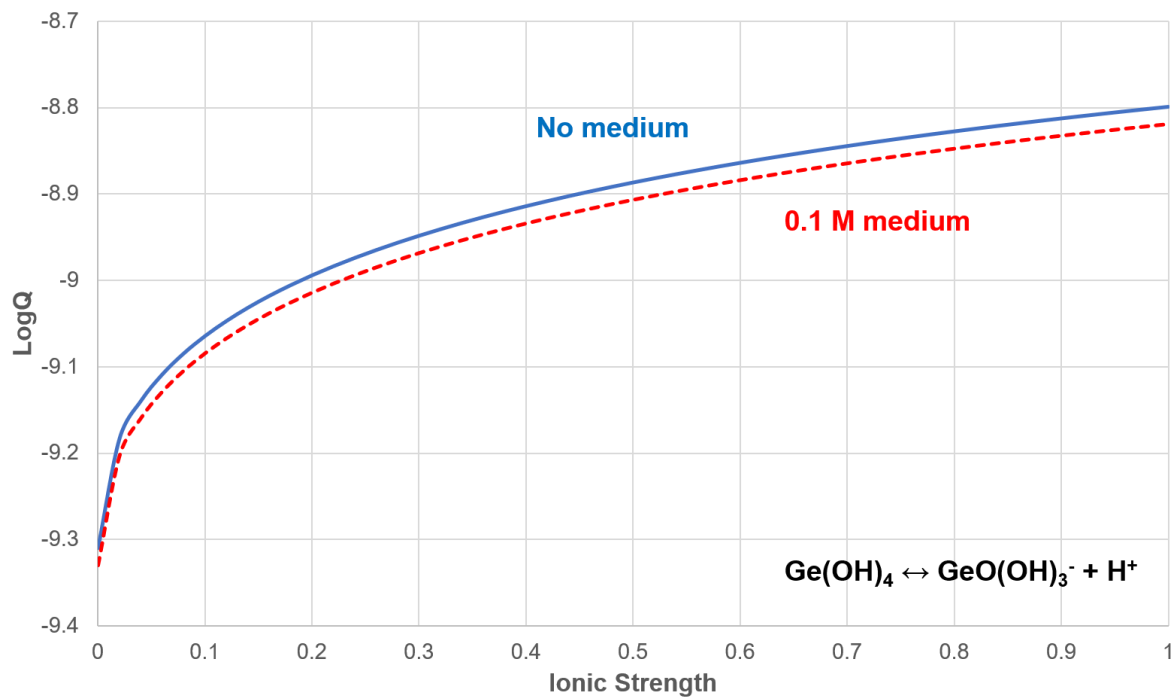


Fig. 4.4 Hydrolysis constant (quotient) of Ge hydroxide species GeO(OH)_3^- (top) and $\text{GeO}_2(\text{OH})_2^{2-}$ (bottom) as a function of ionic strength with and without 0.1 M medium

The speciation distributions for Ga and Ge hydrolysis are shown in Fig.4.5 and Fig. 4.6. Among Ga species, $\text{Ga}(\text{OH})_3$ is insoluble in the aqueous solution [29], [32]. On the other hand, Ge hydrolyses of $\text{GeO}(\text{OH})_3^-$ and $\text{GeO}_2(\text{OH})_2^{2-}$ are both soluble in the aqueous solution. In addition, Ge forms chelates with polyols, which is the hydroxyl functional group of Sephadex G-25, and the polyols are dissociated by HCl. If Ga is mostly present in the form of insoluble species of $\text{Ga}(\text{OH})_3$ and Ge is present in the form of soluble species, then the Ga stays in Sephadex G-25 and Ge can be separated when it reacts with HCl and loses the chelate form. Consequently, the pH range that insoluble Ga species of $\text{Ga}(\text{OH})_3$ and Ge can be separated is pH 10 - 11 in this study, considering the pH change in the Sephadex G-25 column during Ge elution by HCl addition.

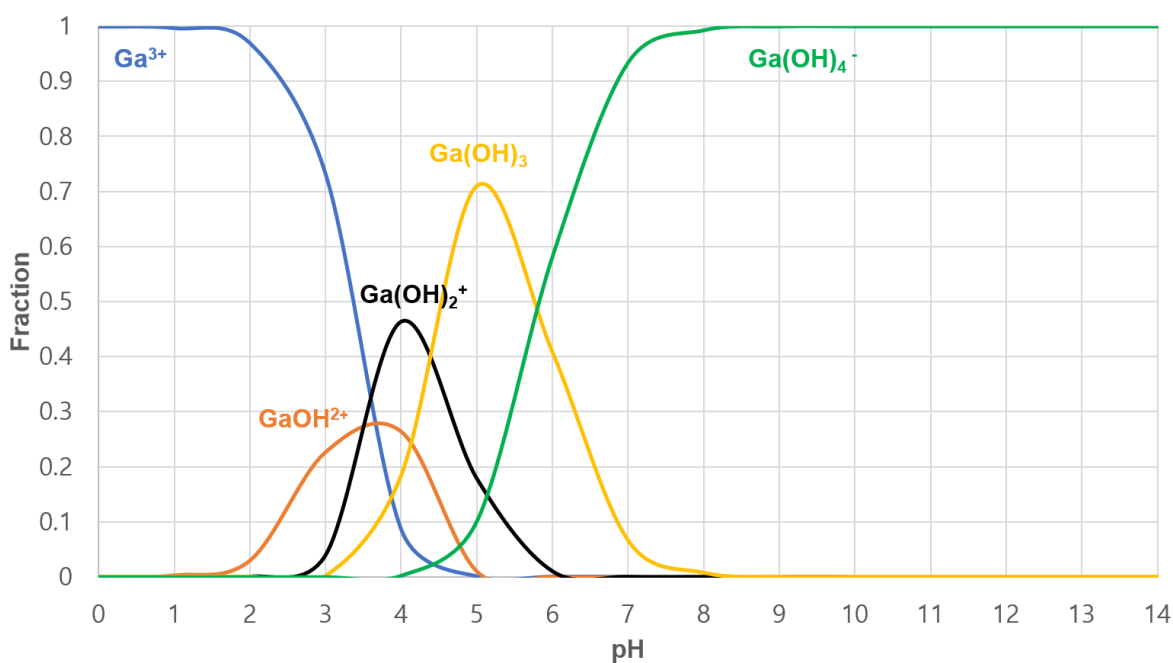


Fig. 4.5 Speciation diagram of Ga-hydroxide distribution as a function of pH, $I = 0.64 \text{ M}$ in the absence of medium

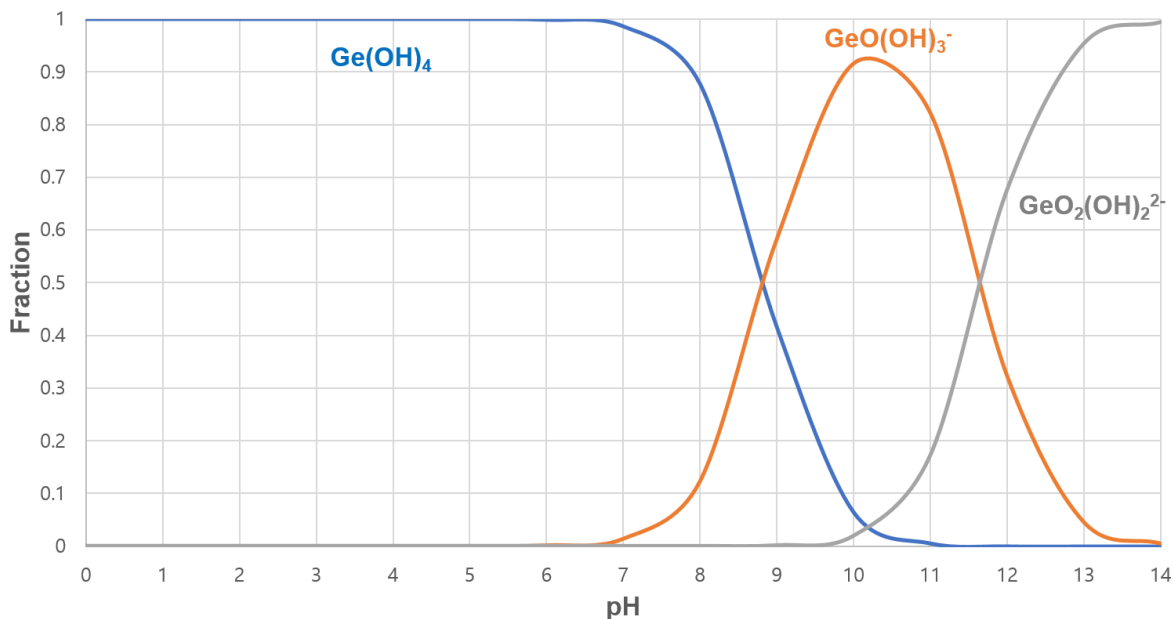


Fig. 4.6 Speciation diagram of Ge-hydroxide distribution as a function of pH, $I = 0.64 \text{ M}$ in the absence of medium

The effect of 0.1 M medium addition was also studied. However, the difference of speciation distribution was so small that speciation diagrams cannot be differentiated. In the case of increased ionic strength, all speciation diagrams showed the tendency to move toward increasing pH. This indicates a high concentration of acid in the starting sample solution needs to be adjusted to higher value of pH to obtain enough fraction of soluble species of Ge to be separated. That would be a disadvantage in ICP-MS samples, where a high amount of concentrated Ge is preferred to reach the detectable concentration, because it requires additional NaOH.

Harada and Tarutani [31] used pH 12 to separate Ge by Sephadex G-25 despite using lower concentration of 0.1 M HNO_3 where Ge was desorbed than in this study. This is because the ionic strength could be greater than our condition due to high concentration of aqueous solutions to preconcentrate Ge from the rock sample.

The Ga speciation diagram also can be derived using thermodynamic data obtained from the solubility measurement of α -GaOOH. However, a different value of the hydrolysis constant from that in Table 1 was obtained [34]. Since the thermodynamic data from the solubility measurement of α -GaOOH was based on 150 °C and extrapolated for 25 °C, the hydrolysis constant for Ga speciation diagram in this study, which targeted to the column experiment at room temperature, used the data in Table 1 based on 25 °C.

For the separation of Ge from Ga by Sephadex G-25, the hydrolysis reactions of Ga and Ge in 4 % HNO₃ at 25 °C were studied. The speciation diagrams of Ga and Ge hydrolysis were derived by thermodynamic calculation. The pH range to separate Ga and Ge by solubility difference was 10 – 11. The low concentration of acid in the starting sample has an advantage on the detection limit of ICP-MS. The effect of medium addition was negligible in the speciation distribution. This work provides the basis for attempting separation of Ga matrix for Ge analysis to improve ICP-MS. Thermodynamic analysis for the hydrolysis equation may be applied to the separation of any elements that react in hydrolysis reactions depending on pH.

5. ACTIVE OXIDATION OF GERMANIUM

The significant amount of Ge loss found in the recovered of 7N and 8N Ga after in-situ MBE distillation and growth cannot be explained by atomic Ge evaporation. In order to explain high Ge loss, a Ge active oxidation hypothesis that Ge additionally evaporates as GeO(g) was proposed. The vapor species diagram representing the distribution of P(GeO) corresponding as a function of background P(O₂) was constructed from thermodynamic study of Ge oxidation. Using the free energy of formation for the reactions of Ge oxidation, the vapor species diagram for pure Ge-O system was constructed. The vapor species diagram for dilute Ge in solution in Ga was also developed, representing essentially a shift in P(O₂) to higher value in proportion inversely to logarithmic value of Ge concentration. The vapor species diagram for dilute Ge showed a high enough amount of GeO can be produced even at extremely low P(O₂) conditions in the MBE. Although the amount of oxygen in the MBE system calculated from background P(O₂) at one moment was not sufficient to consume the amount of Ge found to be lost in the ICP-MS analysis, the estimated oxygen flux striking the liquid Ga surface, considering the MBE operation over 1 year, suggested the sufficient amount of oxygen was supplied to the MBE system.

5.1 Calculations of Ge Atomic Evaporation

The evaporation rate and distilled amount of impurity of Ge in the case of free surface evaporation can be calculated by the Langmuir-Knudsen equation (3.2) [10]. The impurity evaporation depends on the concentration (mole fraction) and the activity coefficient that describes the degree of relative association of the impurity solute and solvent. In the ideal case that all atoms are equivalently

associated with each other such as in a monoatomic gas, the system obeys Raoult's law and the activity coefficient is unity. In a binary solution of Ge and Ga, Ge is negatively deviates from the ideal behavior in the Ga solution [16]. Kostov, Zivkovic and another Zivkovic reported the activity coefficient of Ge in Ga derived from heat enthalpy measured in Oelsen Calorimetry. The reported activity coefficient was close to 1 for 0.006 wt% Ge in Ga. Since our concentration of Ge in Ga was 690 ppb, which is smaller than the value in the Kostov's study, the activity coefficient should be even closer to 1, obeying Raoult's law.

Germanium vapor species are composed of monoatomic species and diatomic species. By applying the existing saturation vapor pressure data [35] for monoatomic species to the Langmuir-Knudsen equation, the evaporated amount of Ge was calculated to be ~ 34 ng at 1360 K for 16 h distillation, and ~ 5 ng at 1160 K for 400 h growth. Although Ga was stored for over a year at idle temperature of 923 K, the evaporated monoatomic Ge is merely 11 pg for a year at this temperature.

The saturation vapor pressure for Ge diatomic species was derived from the reaction of (5.1),



The saturation vapor pressure for the diatomic Ge vapor species can be obtained from the free energy of formation of the reaction (5.1) and the following relations.

$$\Delta G_T^0 = -RT \ln \frac{P(\text{Ge})^2}{P(\text{Ge}_2)} \quad (5.2)$$

Using the obtained vapor pressure of diatomic Ge from (5.2), the evaporated amount of Ge in the form of diatomic species was 0.1 ng during 16 h distillation and 38 pg during 400 h growth. Compared to the monoatomic evaporation rate, these values contribute negligibly to the Ge evaporation.

The Ge loss found in the ICP-MS analysis was 64 μg , while total Ge evaporated amount calculated using Langmuir-Knudsen equation (3.2) was only ~ 39 ng. If the collision and condensation effects in the evaporation from the crucible with receding liquid Ga surface are applied, as discussed in Chapter 3, the significant decrease in the distilled Ge amount is inevitable, which does not even need the crucible effect calculations.

In addition, the concentration of Ge in the ICP-MS should rather have increased, since ~ 25 g in 7N Ga and ~ 29.6 g in 8N Ga were evaporated together with impurities in the calculation of Ga evaporation from the receding liquid surface in the crucible [36]. It was thus found that molecular distillation alone was not sufficient to explain high loss of Ge from the distillation analysis. Therefore, a possible alternative way to explain high loss of Ge is proposed and evaluated in the following section.

5.2 Germanium active oxidation hypothesis from Si active oxidation model

As indicated in the previous section, the molecular distillation of Ge in Ga as a single atom results in only a small amount of Ge evaporation, which cannot explain the high Ge loss found in the ICP-MS results. Consequently, an alternative explanation is required for the high loss of Ge. To fabricate metal oxide gate materials, the method of compound evaporation has been utilized. Also, there is a report that gaseous metal oxide enhances the rate of evaporation of metal vapors by Turkdogan, Grieveson and Darken [37]. From the fact that the metal oxide contributes to increasing the rate of metal evaporation, Ge oxide can be considered to be formed and evaporated

during MBE growth and distillation, thus causing Ge loss. However, oxygen is extremely deficient in the UHV MBE system, and thus the formation of metal oxide seems less probable.

However, there is a case in which the oxidation can occur under extremely low partial pressure of oxygen. Silicon, which has similar oxide forms as Ge, is known to have active oxidation behavior in that Si is oxidized to volatile gaseous oxide at low oxygen partial pressure [38]–[40]. Therefore, Ge has a possibility to be actively oxidized, and thus the gaseous Ge oxide could have caused the removal of Ge in Ga during MBE distillation and growth. To validate the formation of Ge gaseous oxide in MBE conditions, thermodynamic analysis of Ge oxidation will be performed in the following.

5.3 Germanium oxidation analysis

The most-known Ge oxide is solid Ge oxide of $\text{GeO}_2(\text{s})$, produced from the reaction of $\text{Ge}(\text{s})$ and $\text{O}_2(\text{g})$ as written in (5.3)



Kubaschewski and Alcock reported the free energy of formation of $\Delta G_T^0 = -137330 + 44.86T$ (cal/mole) (600 ~ 1173 K) [41]. Although the explanation how it was derived was not given by Kubaschewski and Alcock. Turkdogan [42] also used the equivalent free energy of formation data from Kubaschewski and Alcock's for the Ge oxidation in (5.3).

The equilibrium $P(\text{O}_2)$ at which $\text{GeO}_2(\text{s})$ starts to form is represented as a function of temperature in Fig 5.1. At the distillation temperature, the equilibrium $P(\text{O}_2)$ of the formation of $\text{GeO}_2(\text{s})$ is

above the background $P(O_2)$ of MBE system for both best vacuum condition of $P(O_2) = \sim 10^{-15}$ atm and general vacuum condition of $P(O_2) = \sim 10^{-13}$ atm. However, at the growth temperature, the equilibrium $P(O_2)$ of the $GeO_2(s)$ formation is below the background $P(O_2)$ of MBE system. Therefore, $GeO_2(s)$ can be produced during growth, but cannot be produced during distillation.

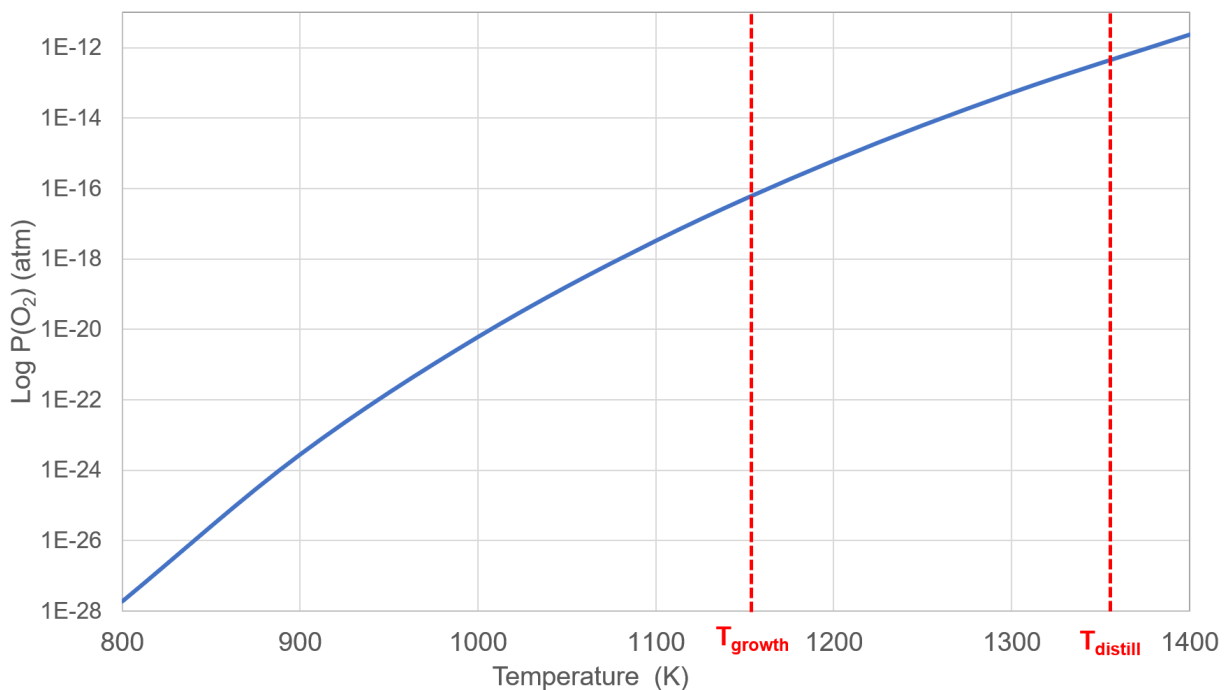
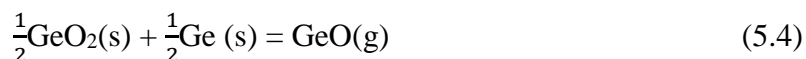


Fig. 5.1 Equilibrium $P(O_2)$ of the formation of $GeO_2(s)$ in the reaction of (1)

Germanium has a gaseous oxide form of $GeO(g)$. The experimentally known $GeO(g)$ formation is the reaction of $GeO_2(s)$ and $Ge(s, l)$ (5.4). Because the reaction (5.4) occurs at relatively high $P(O_2)$, it was experimentally detected earlier.



The experimentally determined free energy of formation of (5.4) is $\Delta G_T^0 = 54600 + 6.9T \log T - 62T$ (cal/mole) ($T = 298 \sim 860$ K) [43].

Another reaction to form gaseous Ge oxide is the direct reaction of Ge with oxygen as shown (5.5). There is no experimental data for the reaction (5.5). The free energy of formation was thus derived by the sum of the existing data of free energy of formation of (5.3) and (5.4). It is $\Delta G_T^0 = -14065 + 6.9T \log T - 39.57T$ (cal/mole).



There is another reaction to form solid Ge oxide by combining gaseous Ge oxide with oxygen (5.6). This reaction is also experimentally unknown. Likewise, the free energy of formation of (5.6) was also derived by the subtracting the free energy of formation data of (5.5) from (5.3) and it is $\Delta G_T^0 = -123265 - 6.9T \log T + 84.43T$ (cal/mole)



The free energy of formation can be derived from the existing thermodynamic data of heat enthalpy and entropy at room temperature, and heat capacity, y equation (5.7) [41].

$$\Delta G_T^0 = \Delta H_{298}^0 + \int_{298}^T \Delta C_p dT - T\Delta S_{298}^0 - T \int_{298}^T \frac{\Delta C_p}{T} dT \quad (5.7)$$

If the contribution of heat capacity terms to the free energy is not large, equation (5.7) can become approximate form (5.8) [41].

$$\Delta G_T^0 = \Delta H_{298}^0 - T\Delta S_{298}^0 \quad (5.8)$$

To evaluate the experimental data of free energy of formation for reactions 5.3) and (5.4), the free energy of formation was derived at 1160 K and 1360 K using existing thermodynamic data. For the reaction (5.3), the free energy of formation from experimental data had only slight relative

error, 3.5 % at 1160 K and 4.9 % at 1360 K, to the derived one using thermodynamic data. However, for the reaction of (5.5), there was a big difference. The relative error of experimentally observed free energy of formation was 100 % at 1160 K and 1783 % at 1360 K to the derived one using thermodynamic data.

Thermodynamic data used for these calculations are listed in Table 5.1. The heat capacity of GeO(g) was not given in the published fitting equation, but a heat capacity value at each temperature point was available. Consequently, the fitting equation was derived using heat capacity data from 298.15 to 1400 K. Since deriving entropy from the temperature dependent term in (5.7) has a large uncertainty due to heat capacity change over temperature, the experimentally observed free energy of formation is considered to be more accurate than the derived one using thermodynamic data. Therefore, the published experimental data were used in this study.

Table 5.1 Thermodynamic data of Ge, Ge oxide, and oxygen

Element	ΔH_{298}^0	ΔS_{298}^0	ΔC_p	Reference
Ge(s)	0	7.43	$5.16 + 1.4 \times 10^{-3}T$	[44], [45]
O ₂ (g)	0	49	$7.16 + 10^{-3}T - 0.4 \times 10^{-5}T^2$	[46], [47]
GeO (g)	-7330	53.5	$34.26 + 2.33 \times 10^{-3}T - 3.82 \times 10^{-5}T^2$	[48]
GeO ₂ (s)	-138600	9.5	$15.92 + 2.77 \times 10^{-3}T - 4.24 \times 10^{-5}T^2$	[49]

5.4 Construction of vapor species diagram of Ge-O system

A vapor species diagram is the distribution of vapor pressure of volatile species as a function of the corresponding vapor pressure of oxygen involved in the oxidation. The vapor species diagram facilitates identification of the formation of condensed oxide or volatile oxide at any particular temperature. Consequently, the vapor pressure of GeO as a function of $P(O_2)$ at the growth and distillation temperatures determines the oxide type produced at those conditions, so providing the equilibrium vapor pressure of GeO at a given $P(O_2)$.

5.4.1 Pure Ge

The free energy of formation can be represented by the logarithm of the equilibrium constant K , as shown in equation (5.9).

$$\Delta G^0 = -RT \ln K = -4.575 \log K \quad (5.9)$$

The equilibrium constant K can be represented by the ratio of activities of products and reactant in the particular Ge oxidation. Assuming the activity of pure condensed phases is one, the logarithmic linear relation of the equilibrium constant, $P(\text{GeO})$, and $P(O_2)$ is for the Ge oxidation of (5.3), (5.5) and (5.6), derived in the form of (5.10),

$$\log K = A \log P(\text{GeO}) + B \log P(O_2) \quad (5.10)$$

where A and B are stoichiometric constants for the particular equilibrium. Applying equation (5.10) to the Ge oxidation of (5.3), (5.5) and (5.6) at specific temperature and fitting on the plot of $\log P(\text{GeO})$ vs. $\log P(O_2)$, the vapor species diagram for Ge-O system of Fig 5.2 is obtained.

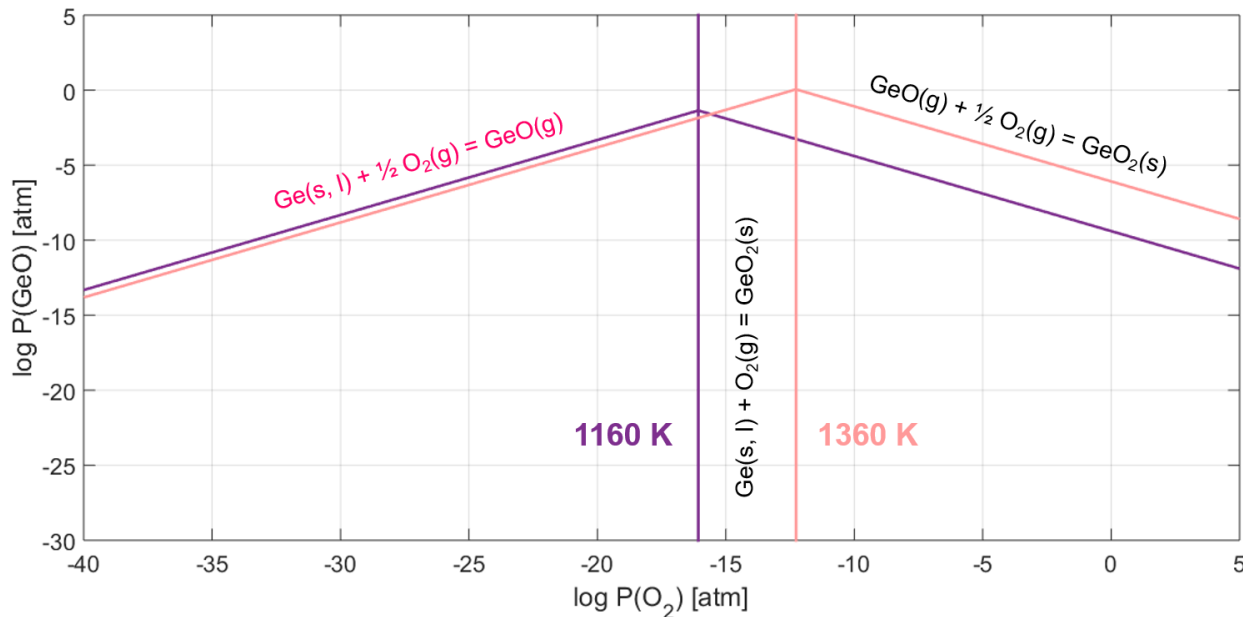


Fig. 5.2 Vapor species diagram for pure Ge-O system at growth and distillation temperature

Below the equilibrium $P(\text{O}_2)$ of 8.5×10^{-17} atm at 1160 K and 5.4×10^{-13} atm at 1360 K where the solid Ge oxide of GeO_2 starts to form, Ge is directly oxidized to gaseous oxide of $\text{GeO}(\text{g})$ with relatively high equilibrium $P(\text{GeO})$. This implies Ge can be actively oxidized at an extremely low $P(\text{O}_2)$ condition. Above the $P(\text{O}_2)$ of 8.5×10^{-17} atm at 1160 K and 5.4×10^{-13} atm at 1360 K, the solid Ge oxide of GeO_2 becomes stable and $P(\text{GeO})$ starts to decrease as Ge is passively oxidized.

In the typical elemental oxidation, the solid oxide should be deposited and visibly shown above the equilibrium $P(\text{O}_2)$ of the solid oxide. However, for elements with both solid and gaseous oxide such as Si and Ge, different oxidation tendencies and mechanisms are expected. According to Wagner's model [38], [39] for Si active oxidation, solid Si oxide of $\text{SiO}_2(\text{s})$ formed on the Si surface is readily reduced to $\text{SiO}(\text{g})$ from the reaction of $\text{Si}(\text{s}, \text{l})$ and $\text{SiO}_2(\text{s})$ until $P(\text{O}_2)$ reaches a critical $P(\text{O}_2)$ which is well above the oxidation pressure of the solid oxide. From a simplified analysis [38], [39] the critical $P(\text{O}_2)$ is twice the equilibrium $P(\text{SiO})$ multiplied by the square root

of the diffusivity ratio of gaseous oxide and oxygen, which was obtained from the net transport rate of oxygen on the surface of the solid oxide on Si under the steady state conditions.

Likewise, Ge reacts with the GeO_2 produced after the equilibrium $P(\text{O}_2)$ at which GeO_2 starts to form, actively being oxidized to GeO, as confirmed in the Ge oxidation of (5.6). This indirect active oxidation, where GeO is formed after previously produced GeO_2 , continues until the $P(\text{O}_2)$ reaches the critical $P(\text{O}_2)_{crit}$ defined by the equation (5.11),

$$P(\text{O}_2)_{crit} = \frac{1}{2} \left(\frac{D_{\text{GeO}}}{D_{\text{O}_2}} \right)^{\frac{1}{2}} P(\text{GeO})_{eq} \quad (5.11)$$

where D is diffusivity of GeO and O_2 . The equilibrium $P(\text{GeO})$ is obtained from the relation of equilibrium constant and $P(\text{GeO})$ in (5.10). Assuming the diffusivity ratio of GeO and O_2 is 1, the critical $P(\text{O}_2)$ is obtained from the half of the equilibrium $P(\text{GeO})$ in (5.10).

When the system $P(\text{O}_2)$ is higher than critical $P(\text{O}_2)$, the Ge oxidation of (5.10) tends to maintain the status of GeO_2 rather than forming GeO. Consequently, Ge is only passively oxidized to $\text{GeO}_2(\text{s})$ and the critical $P(\text{O}_2)$ becomes the transition point from active to passive oxidation. The transition point from active to passive oxidation of the critical $P(\text{O}_2)$ as a function of temperature is given by Fig 5.3. The transition point is 0.02 atm at 1160 K and 0.56 atm at 1360 K. This pressure is surprisingly high, as it is for in the Si/SiO/SiO₂ system. It indicates that active oxidation would occur at oxygen pressure nearly up to atmospheric pressure.

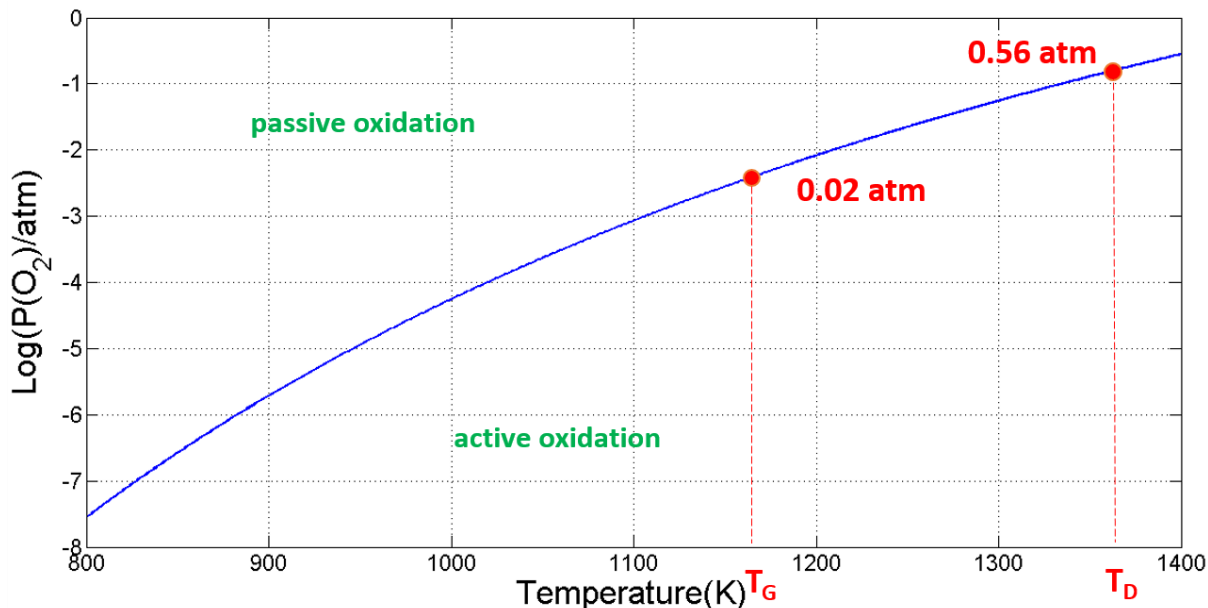


Fig. 5.3 Transition points of active oxidation to passive oxidation for pure Ge
(T_G: 1160 K for growth, T_D 1360 K for distillation)

In conclusion, for the pure Ge-O system, Ge is oxidized to GeO in direct active oxidation of (5.8) until the system P(O₂) reaches the equilibrium P(O₂) where the solid Ge oxide of GeO₂ starts to form. The equilibrium P(O₂) is 8.5×10^{-17} atm at 1160 K and 5.4×10^{-13} atm at 1360 K. After the equilibrium P(O₂), Ge is oxidized to GeO in the indirect active oxidation of (5.4). This indirect active oxidation continues until the system P(O₂) reaches the critical P(O₂) in Fig 5.3. After the critical P(O₂), Ge is passively oxidized to GeO₂.

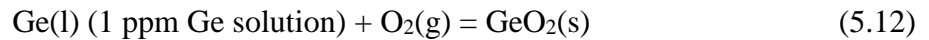
Shalav and coworkers [50] derived the oxidation stability diagram for pure Ge at 933 K at different temperatures from this study. However, the source of thermochemical data used to derive the oxidation stability diagram was not evaluated in their work. The transition point from active to passive oxidation was calculated from the maximum value of P(GeO), which does not follow the method provided by Wagner's model [38], [39]. Consequently, the occurrence of indirect active

oxidation in the region above the equilibrium $P(O_2)$ of the reaction (5.3) was discarded, which was caused by driving force due to relative flux difference of $P(GeO)$ and background vapor pressure.

5.4.2 Dilute Ge in Ga(l)

Germanium oxidation in the in-situ MBE distillation is not the oxidation for pure Ge, but for dilute Ge of 690 ppb in pure Ga. The oxidation of Ge in dilute solution should be evaluated in a different way due to the difference in the activity of Ge to oxygen and the presence of the activity of Ge to Ga. The vapor species diagram for Ge-O system developed in the previous section is for pure Ge. In order to understand the Ge oxidation in dilute solution, the vapor species diagram for the pure Ge system will be converted to the 1 ppm Ge closed to 690 ppb in a Ga system in the following.

The oxidation of Ge as 1 ppm Ge dilute solution in liquid Ga to produce solid Ge oxide is as written by equation (5.12).



The change of free energy of formation of (5.12) and (5.13) can be represented by the logarithmic ratio of equilibrium constants of (5.12) and (5.13). Then the equilibrium constant can be represented by the activity ratio of products and reactants. Since the only difference of activities in (5.12) and (5.13) is 1 ppm Ge versus pure Ge, the change of free energy of formation can be represented by the ratio of 1 ppm Ge activity (h) to Ge activity (a) as shown in the equation (5.14).

$$\Delta G_{13}^0 - \Delta G_5^0 = -RT \ln \frac{a}{h} = -4.575 \log \frac{a}{h} \quad (5.14)$$

The a is Ge activity defined in Raoultian reference frame. The activity in Raoultian reference frame is proportional to mole fraction of Ge with the activity coefficient of γ . The 1 ppm Ge activity of h is the activity defined in dilute solution (Henrian) frame of 1 ppm. The activity is represented by the product of the activity coefficient and concentration. For convenience, the concentration of 1 ppm Ge is assumed to be one in the 1 ppm dilute solution frame. Since the activity coefficient of Ge in Ga in dilute solution is 1, the activity of 1 ppm Ge in 1 ppm dilute solution frame is 1. When the activity, which is assumed to be 1 in the 1 ppm frame, is read in Raoultian reference frame that 1 mole fraction is assumed to be 1, it becomes 10^{-6} times activity, assuming the atomic weights of solute and solvent are same. Therefore, the ratio of Henrian activity to Raoultian activity is 10^6 , and thus the relation of free energy of formation at 1 ppm frame with Raoultian frame is defined by equation (5.15)

$$\Delta G_2^0 = \Delta G_1^0 - 4.575T \log 10^{-6} \quad (5.15)$$

In general, the relation of free energy for the concentration of C in a dilute solution compared to that for the pure liquid is,

$$\Delta G_{dilute}^0 = \Delta G_{pure}^0 - 4.575T \log C \quad (5.16)$$

Using the derived free energy of formation for 1 ppm Ge, the vapor species diagram for 1 ppm Ge-O system was constructed, as shown in Fig 5.4. The Ge oxidations of (5.3) and (5.5) contain 1 ppm Ge in the reactant. Consequently, the free energy of formation for 1 ppm Ge increased as much as $(4.575 \times 6)T$ over that for pure Ge and thus causing the vapor species diagram being shifted to the right as much as 6 orders of magnitude. As the diagram is shifted to the right, $P(\text{GeO})$ is decreased to 10^6 times lower, and the equilibrium $P(\text{O}_2)$ where solid Ge oxide of GeO_2 starts to

form increased 10^6 times higher. In other words, the lower activity of Ge requires a higher $P(\text{O}_2)$ for oxidation.

Germanium oxidation, according to the equilibrium of (5.6), does not contain 1 ppm Ge, and the reactants of GeO and O_2 in (5.6) are independent of the dilute 1 ppm Ge. Hence, the free energy of formation of (5.6) in a 1 ppm Ge-O system is equivalent to that in the pure Ge-O system. However, the occurrence of the Ge oxidation of (5.6) was confined by the equilibrium $P(\text{O}_2)$ starting the Ge oxidation of (5.3). Therefore, the $P(\text{O}_2)$ that the Ge oxidation of (5.6) starts was also increased by a factor of 10^6 . Due to the $P(\text{O}_2)$ increase of 10^6 and $P(\text{GeO})$ decrease of 10^6 , the maximum $P(\text{GeO})$ in 1 ppm Ge-O system decreased by 10^3 .

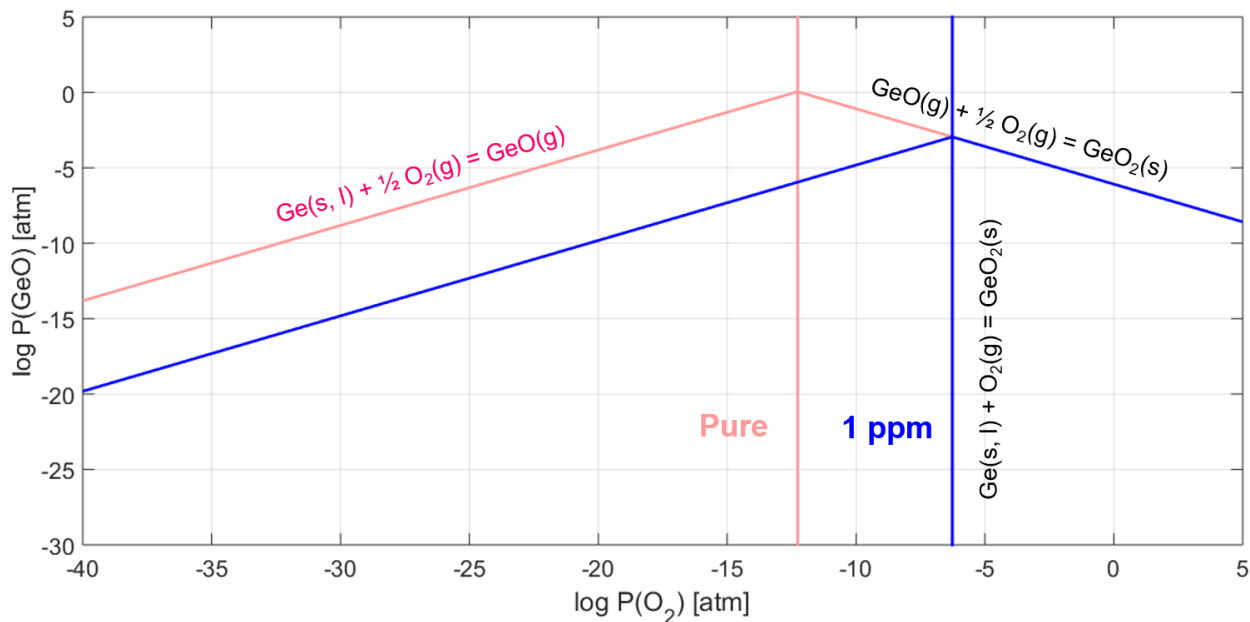


Fig. 5.4 Vapor Species diagram comparison of 1 ppm Ge-O system and pure Ge-O system at 1360 K

The transition point from active to passive oxidation at 1 ppm Ge-O system as a function of temperature is shown in Fig 5.5. Equations (5.4) and (5.9) were used to derive the transition point as for the transition point for pure Ge-O system. The difference from the pure Ge-O system was the reference frame change because of the decreased concentration to 1 ppm. Similar to the derivation of the vapor species diagram for 1 ppm Ge-O system, the free energy of formation of the reaction (5.4) for 1 ppm Ge was converted with the term from the reference frame change. Since the reaction of (5.4) contains a half mole of 1 ppm Ge in the reactant, the concentration term becomes half order, as shown in the equation (5.17).

$$\Delta G_{dilute}^0 = \Delta G_{pure}^0 - 4.575T \log C^{\frac{1}{2}} \quad (5.17)$$

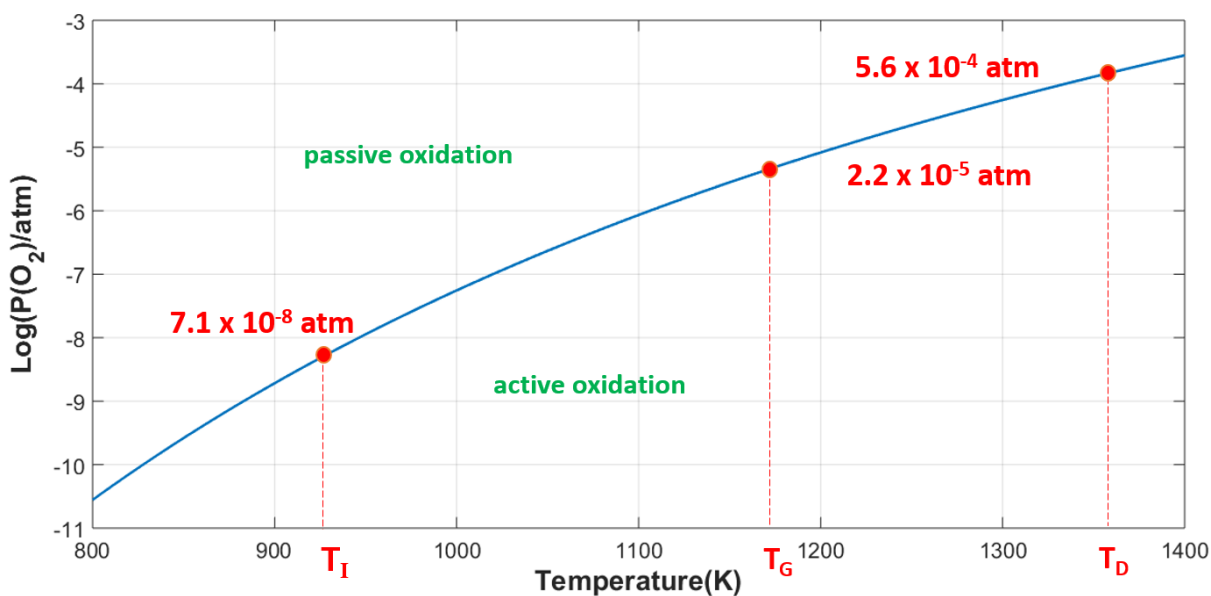


Fig. 5.5 Transition points of active oxidation to passive oxidation for 1 ppm Ge

5.4.3 The oxidation and evaporation behavior of 1 ppm Ge in Ga in MBE system

The dilute solution of Ge in Ga in the MBE system passed through three different temperature conditions of 923 K for idle condition, 1160 K for growth and 1360 K for distillation. For the three temperature conditions, the vapor species diagram for 1 ppm Ge-O system was constructed, shown in Fig 5.6. As confirmed in the vapor species diagram for pure Ge-O system of Fig 5.3, higher temperature yields higher maximum $P(\text{GeO})$ at the higher equilibrium $P(\text{O}_2)$ at which $\text{GeO}_2(\text{s})$ becomes stable. However, the lower temperature, the $P(\text{GeO})$ slightly higher at the same $P(\text{O}_2)$ below the equilibrium $P(\text{O}_2)$ at which $\text{GeO}_2(\text{s})$ becomes stable. This implies larger active oxidation occurs at lower temperature when the active oxidation is confined within the direct active oxidation region.

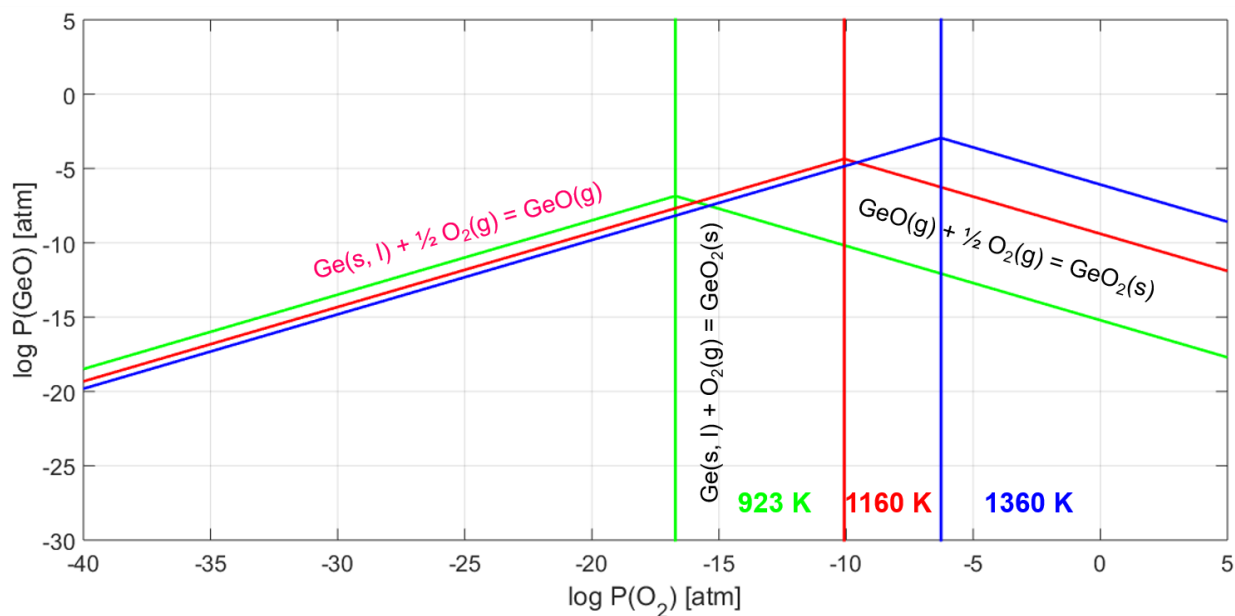


Fig. 5.6 Vapor species diagram of 1 ppm Ge-O system at 923 K, 1160 K, and 1360 K

The background $P(O_2)$ in the MBE operation was 3×10^{-15} atm at best, and 10^{-13} atm in the normal vacuum condition. For the background MBE $P(O_2)$ of both best and normal conditions, distillation (1360 K) and growth (1160 K) both fall into the direct active oxidation region. In the background $P(O_2)$ in the MBE, the equilibrium $P(GeO)$ is quite high at both 1160 K and 1360 K. Since $P(GeO)$ is 100 times higher than the background vapor pressure, the evaporation of Ge as GeO is driven. Germanium thus can be actively oxidized even in the very low $P(O_2)$ condition of MBE and thus the high Ge loss found in the ICP-MS results can be explained by this Ge active oxidation hypothesis.

On the other hand, the MBE $P(O_2)$ is higher than the equilibrium $P(O_2)$ where $GeO_2(s)$ starts to form at the idle temperature condition of 923 K. Since the transition point from active to passive oxidation at the idle temperature is 7×10^{-8} atm, and both normal and best MBE $P(O_2)$ are below the transition point of 7×10^{-8} atm, the oxidation behavior of 1 ppm Ge at the idle temperature of 923 K is predicted to occur by indirect active oxidation. Germanium present in Ga combines with the produced GeO_2 , emitting GeO. The indirect active oxidation requires the precedent formation of GeO_2 before the formation of GeO. Thus, the speed of GeO formation in the indirect active oxidation mechanism is expected to be slower than the direct active oxidation, in which Ge directly reacts with oxygen without forming GeO_2 first.

The maximum evaporation rate of GeO is obtained by equation (2.1). The saturation vapor pressure of $P(GeO)$, which is proportional to the maximum evaporation rate of GeO, can be obtained from the vapor species diagram corresponding to the temperature and $P(O_2)$. At the normal vacuum condition of 10^{-13} atm, $P(GeO)$ was 1.2×10^{-9} atm at 923 K in the region of indirect

active oxidation and 2.4 atm at 1160 K and 0.78 atm at 1360 K in the region of direct active oxidation. At the best vacuum condition of 3×10^{-15} atm, $P(\text{GeO})$ at 923 K increased to 1.2×10^{-8} atm because $P(\text{GeO})$ increases as $P(\text{O}_2)$ decreases in the region of indirect active oxidation. The $P(\text{GeO})$ decreased in the best vacuum to 2.4 atm at 1160 K and 0.078 atm at 1360 K in the region of direct active oxidation.

Since $P(\text{GeO})$ at 923K is relatively much lower than $P(\text{GeO})$ at 1160 K and $P(\text{GeO})$ at 1360 K for both cases of vacuum conditions, Ge is less probable to be lost at 923 K. However, in the region of direct active oxidation, the lower temperature showed higher $P(\text{GeO})$. Hence, Ge can be lost more as GeO during growth than distillation. If enough Ge is not lost during distillation ahead of growth, Ge can be transferred to the thin film of GaAs, causing the degradation of electron mobility. This agrees with the result that the peak mobility of 7N Ga with high Ge was lower than 8N Ga with low Ge in Gardner and coworkers' report [6], even though Ga passed through distillation before growth.

5.5 Justification of Active Oxidation by Mass Balance and Flux Calculations

Atomic Ge evaporation cannot explain the ICP-MS results, however, Ge active oxidation and evaporation as GeO showed the possibility of high Ge loss even in the very low MBE $P(\text{O}_2)$ condition. Although the MBE $P(\text{O}_2)$ condition satisfied the Ge loss in Ge active oxidation, it was not proved there was enough oxygen for Ge loss of 64 μg , corresponding to the decrease from 690 ppb (out of 100 g Ga) to 65 ppb (out of 75 g). Therefore, here, it will be investigated whether the oxygen amount was sufficient to make the 64 μg of Ge lost in the MBE system during growth

campaign (idle + growth + distillation) in mass balance. The ideal closed system will be discussed first and then the open system for MBE will be discussed.

According to GDMS analysis for the initial 7N Ga (Appendix B), the oxygen concentration dissolved in Ga was 10 ppb. For 100 g initial Ga, the amount of oxygen is 1 μg as well as $\sim 3.1 \times 10^{-8}$ mole. One oxygen molecule makes two GeO molecules in direct active oxidation. The GeO produced from the 3.1×10^{-8} moles of O_2 is 6.3×10^{-8} moles, and the amount of GeO becomes 4.5 μg from the GeO molecular mass of 88.64 g/mol.

In addition to oxygen dissolved in Ga, there were oxygen molecules available to combine with Ge from the background. The RGA spectrum [51] measured the vacuum level of molecules that can be an oxygen source. Assuming the volume of the MBE system is 0.5 m^3 and the temperature of MBE system during operation is 300 K, the oxygen molecules present in the MBE chamber are 3×10^{-12} mole by ideal gas law. This makes a Ge loss of only 0.2 ng, which is negligible even compared to that possible by oxygen dissolved in Ga.

In the closed system cases, the amount of oxygen Ge can combine with is only 4.5 μg , which is the sum of dissolved oxygen and oxygen sources from background (one time) without matter exchange with surroundings. In the closed system, Ge is actively oxidized to GeO(g) in the crucible with the volume of $\frac{26}{3} \text{ cm}^3$ at 1360 K, assuming that the only oxide form produced by the oxidation is GeO(g). The initial $P(\text{O}_2)$ is 10^{-15} atm and no further increase in $P(\text{O}_2)$ is assumed. Consequently, as GeO is produced, $P(\text{O}_2)$ would decrease.

Below 10^{-15} atm at 1360 K, Ge is actively oxidized in direct active oxidation. As GeO is produced, O_2 is consumed. For a decrement in $P(O_2)$ from 10^{-15} atm to 10^{-16} atm, the amount of GeO produced is 1.40×10^{-19} moles, and the increased $P(GeO)$ due to the increased amount of GeO is 1.80×10^{-15} atm. As the Ge oxidation reaction proceeds, the amount of O_2 and the corresponding $P(O_2)$ decrease for the crucible volume and temperature of 1360 K and the amount of GeO increases and the corresponding $P(GeO)$ increases. The ratio of the increased amount of O_2 to GeO is 1:2, as defined in the reaction (5.5), and the ratio of vapor pressure change of O_2 to GeO also obeys the ratio of 1:2 for the fixed volume and temperature where the reaction occurs because pressure is proportional to the mole number according to the ideal gas law.

The $P(GeO)$ approaches 2×10^{-15} atm as the Ge oxidation proceeds, but never reaches 2×10^{-15} atm. When the system reached equilibrium, the $P(O_2)$ is 6.55×10^{-42} atm at $P(GeO)$ of $\sim 2 \times 10^{-15}$ atm, following the equilibrium state of (5.5) and the equation describing the equilibrium of $\log K = \log P(GeO) - \log P(O_2)$. The equilibrium constant of K for the reaction (5.5) is 5.6 at 1360 K. When the system reached the equilibrium, the possible maximum Ge loss in GeO vapor is 1.55×10^{-19} moles in the number of moles and 2.14×10^{-21} g in weight.

In the closed system, as oxidation occurs, the speed of Ge oxidation, and evaporation as GeO, is predicted to become faster. However, the maximum amount of oxygen is limited, so maximum amount of GeO that can be produced from the limited oxygen is $4.54 \mu\text{g}$. This cannot explain the ICP-MS results of $64 \mu\text{g}$ Ge loss.

However, the MBE chamber is actually an open system. Although the MBE background $P(O_2)$ is maintained to 10^{-15} atm in the best and 10^{-13} atm in the normal condition by several cryopumps, there is matter exchange with surroundings and consumed oxygen can be replaced. Therefore, a flux calculation is more accurate than only a mass balance calculation to evaluate whether enough oxygen is present in the system in the open system over a sufficiently long time.

Flux (Γ) is defined by the following equation of (5.18) [52]

$$\Gamma \left(\frac{1}{m^2 \cdot s} \right) = P \sqrt{\frac{N_A}{2\pi M k_B T}} \quad (5.18)$$

where P (Pascal) is vapor pressure, M (kg/mol) is molecular weight, k_B is Boltzmann constant (1.38×10^{-23} m²·kg/s²·K), and T (K) is temperature.

Oxygen flux at selected MBE temperatures as a function of partial pressure of oxygen is shown in Fig 5.7. At the best vacuum condition of 10^{-15} atm, the flux of oxygen striking with Ga surface is 2 to 5×10^{16} (m²·s⁻¹). For the Ga surface of 4.12×10^{-4} m² in the crucible, the number of O₂ molecules striking the Ga surface per second is 4.86×10^{19} . Considering MBE growth campaigns continued more than 1 year and Ga was stored in the crucible in the cell during that time, the total oxygen amount in the MBE system is ~ 2543 moles over 1 year, and this is enough to make Ge of 70.02 g be lost in GeO.

In the open system, $P(O_2)$ is constantly maintained, though oxygen is consumed by active oxidation of Ge. The produced GeO is removed by being pumped out or being transferred to the MBE tunnel, and hence $P(GeO)$ never reached the equilibrium state.

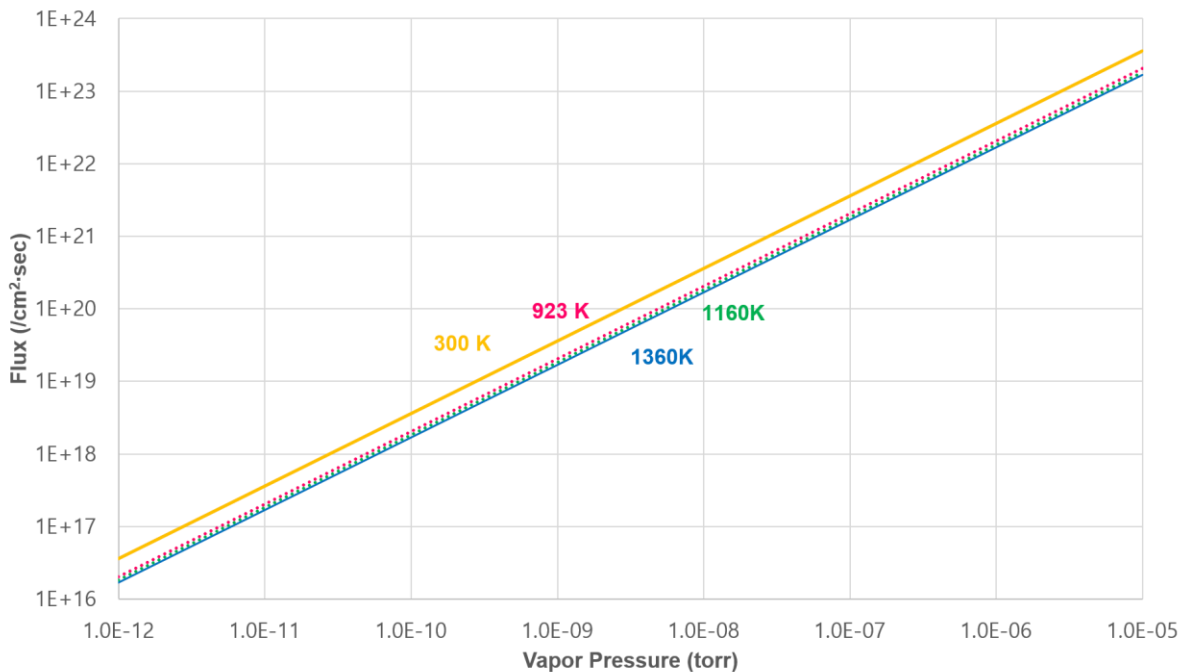


Fig. 5.7 Oxygen flux change upon $P(O_2)$ in the system

5.6 Consideration of other volatile compound evaporation causing Ge loss

5.6.1 The formation of GeO from N_2O or NO_2 involvement

Gaseous Ge oxide of $GeO(g)$ can be produced from the reaction of Ge with NO_2 or N_2O , as shown in the eq (5.19) and (5.20). The free energy of formation of (5.19) is $G_T^0 = 6340 + 39.08T$ and that of (5.20) is $-26940 + 39.29T$. Both free energies of formation of (5.19) and (5.20) are negative at distillation and growth temperatures, and thus there is a driving force to produce GeO without additional external force [53], [54].



In the RGA spectrum measured before distillation and growth, the peak of mass number of 44 for $\text{N}_2\text{O}(\text{g})$ was 7×10^{-11} torr. However, there are other compounds sharing the same mass number of 44 such as $\text{CO}_2(\text{g})$. Considering the composition of $\text{NO}_2(\text{g})$ in the air ranges from a trace to 0.000002 % while $\text{CO}_2(\text{g})$ is 0.0350 %, the measured peak in the RGA is regarded as CO_2 . The RGA peak for the mass number of 46, corresponding to NO_2 , was below the detection limit of 10^{-13} torr. Therefore, the probability that GeO is produced from the reaction of Ge with NO_2 or N_2O is very low due to the rare presence of NO_2 and N_2O .

5.6.2 Volatile GeCl_4

Germanium can be evaporated in other volatile compounds. One example is GeCl_4 . The vapor pressure of pure GeCl_4 is significantly high compared with the vapor pressure of Ge itself, which already reaches 1 atm at ~ 337 K. Therefore, a distillation technique was applied to Ga under a chlorine atmosphere, or Ga chlorine compounds to purify Ga, in the previous study, Nisel'son et al. purified GaCl_3 by a factor of 20 ~ 100, also decreasing the impurities of Fe, PbCl_2 , CuCl_2 and Mg. Pure Ga was obtained from decomposing purified GaCl_3 by distillation in other processing techniques. However, there was no Cl source in the MBE. Although a small quantity of HCl was used to etch vacuum components, these are considered to be all removed during hardware (cell and crucible) outgassing before Ga sample loading.

6. MOLECULAR DISTILLATION EXPERIMENT

A molecular distillation experiment was conducted to confirm the active oxidation of impurity Ge and investigate the evaporation behavior of Ga and its other impurities. A custom chamber was prepared to evaporate and condense Ga under high vacuum conditions with heating of the Ga in an MBE cell to 1360 K. A Residual Gas Analyzer (RGA) was also incorporated to monitor vacuum level and gaseous species from the Ga and impurities and their possible interaction with background during distillation. The same ultra-pure Ga of 7N Grade (but with unusually high Ge concentration) as in the in-situ distillation experiments in the MBE analyzed in Chapter 5 was used as a sample for the distillation experiment. The distillation was performed at 1360 K for 16 hours and the residual Ga was extracted and analyzed by GDMS for Ge and a broad range of other impurities. The results are compared to the in-situ MBE distillations experiments and discussed in terms of the thermodynamics and kinetics analysis presented in Chapter 5.

6.1 Setup of Vacuum Chamber for Materials Distillation

A cylindrical stainless steel vacuum chamber was prepared to evaporate and condense Ga from an MBE cell under ultra-high vacuum (UHV). The chamber was originally purchased and set up in the Turner Lab in the School of Materials Engineering, but saw only limited use. The chamber referred to as 'Materials Distillation Chamber' had 17 flanges, including an openable glass window flange and a closed glass flange. The nominal dimensions of the chamber were 41 cm (16.5 in) diameter and 51 cm (20.5 in) high with the volume of ~ 0.08 m³. As shown in Fig 6.1, initially five flanges of the chamber were open. The open flanges were closed with blank flanges or left to connect to the equipment such as Residual Gas analyzer (RGA), Ion Gauge Tube, leak valve,

angle/inline valve, and heavy duty molecular drag pump. The ConFlat(CF) flanges with feedthroughs were replaced by blank flanges and the 8 inch openable glass flange was replaced by blank flange. The inside and outside of the chamber were cleaned by methanol, acetone, and isopropanol. The chamber was installed upright on a unistrut stand, as shown in Fig 6.2.

In the following, each piece of equipment attached to the Materials Distillation Chamber will be described. Since a detailed history of the chamber was not available, and to trace the initial status of the chamber for future use, the equipment installed is described in detail based on the drawing of Fig 6.1.

The heavy duty molecular drag pump (BH2-60HD, Drivac, Inc., Furlong, PA) was connected to the chamber to decrease the vacuum pressure of the chamber and maintain the high vacuum. The molecular drag pump could provide a backing pressure of 10^{-5} torr for the turbo extension in the UHV system [55]. The pump connector size was equivalent to ISO63. The pump was connected to the chamber through Standard Angle/Inline Valves (Kurt J. Leker Jefferson Hills, PA) installed on the upper flange of the left side of the chamber with an O-ring gasket. The operating pressure range of these valves is rated from atmospheric pressure to 10^{-9} torr, with a leak rate 2×10^{-9} std. cc/sec and maximum temperature (for bakeout) of 150 °C.

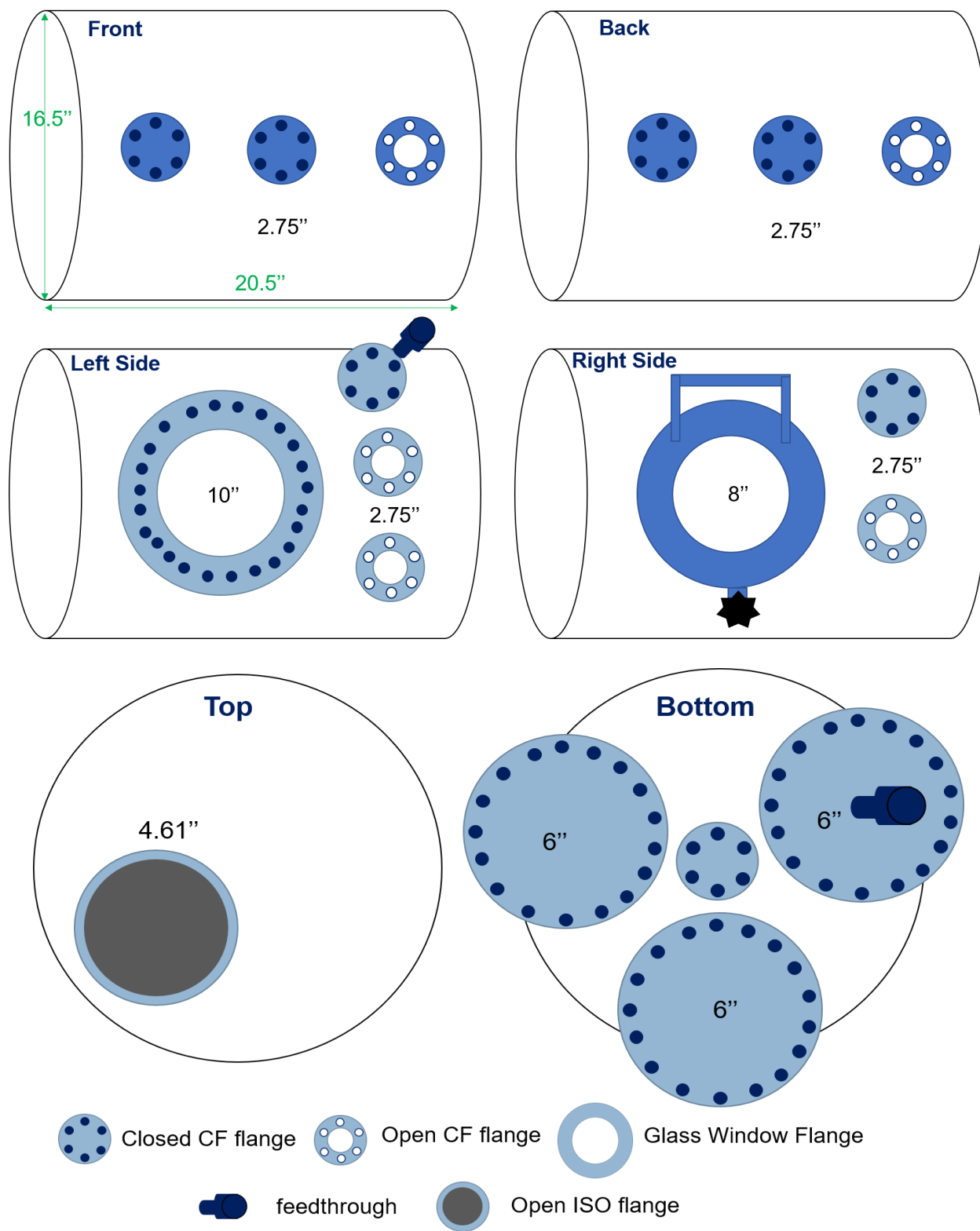


Fig. 6.1 Materials distillation chamber drawing

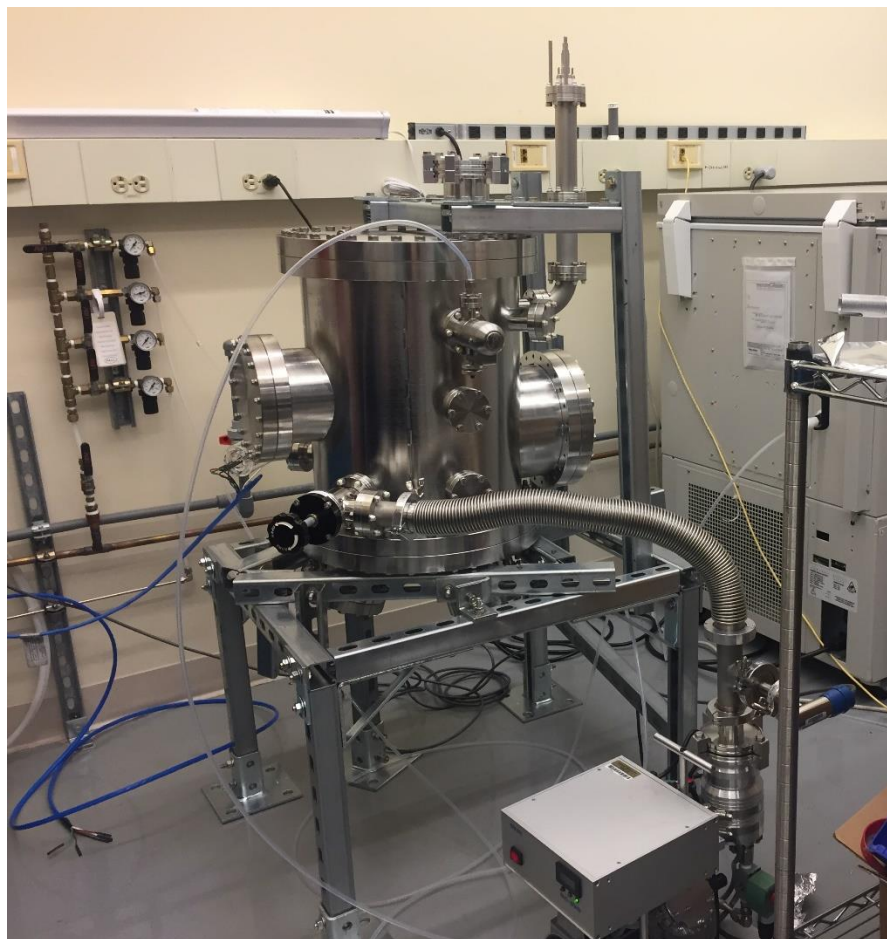


Fig. 6.2 Installed materials distillation chamber

Since the vacuum chamber for materials distillation should be maintained clean even during venting for replacing components and loading samples and equipment, a leak valve (Model 951-5106, Serial No. 85230) (Varian, Torino, Italy) was installed to the chamber for Ar injection during venting. The leak valve is made of stainless steel, sapphire, OFHC copper and a copper alloy. The maximum leak rate of the leak valve was 10^{-9} torr·L/sec. The operating vacuum range of the leak valve was atmospheric pressure to below 10^{-11} torr, with the maximum inlet gas pressure of 500 psi. The allowed temperature range was up to 450 °C .

The overall vacuum pressure of the chamber was measured by a Hot Filament Ion Gauge Tube (Kurt J. Lesker, Jefferson Hills, PA) and Granville-Phillips 350 Ionization Gauge Controller (MKS Instruments, Inc., Longmont, Co). The Ion Gauge Tube was installed on the lower flange of left side of chamber . The filament of the ion gauge tube was made of iridium. Contamination of the ion gauge tube naturally degrades the measurement efficiency, and thus degassing was employed to clean the tube and remove the contamination. Among two possible types of degassing methods, resistive heating (I2R) and electron bombardment, the ion gauge tube connected to the chamber used resistive heating of the double helical grid. The gauge has a linear response from 10^{-4} torr to 10^{-9} torr, whereas the controller could read from 10^{-2} torr to 10^{-11} torr.

An additional vacuum gauge was connected to the heavy molecular drag pump for use during venting or initial pumping before reaching 10^{-2} torr of total vacuum pressure of chamber. This system, with vacuum measurement controller of Granville-Phillips Convectron 472 (Vacuum Barrier Corporation, Woburn, MA), could read to 0.5 millitorr calibrated in N_2 .

The RGA 200 (Stanford Research System, Sunnyvale, CA) was installed on the top flange of back of the chamber to monitor the gases inside the vacuum chamber. The installed RGA 200 was a quadrupole mass spectrometer able to measure a gaseous element with the mass number of 1 to 200 amu [56]. Two types of detector modes, Faraday cup and Electron multiplier (CDEM), were available. The operating pressure range of the Faraday cup mode was 10^{-4} torr to UHV and CDEM mode was 10^{-6} torr to UHV. The detection limit of the Faraday cup mode was 5×10^{-11} torr and CDEM mode was 5×10^{-14} torr. Both modes were used in the in-situ MBE distillation. The maximum operating temperature of the RGA 200 was $70^\circ C$ and recommended bake-out

temperature was 200 °C. Although the partial pressures measured by RGA are given by three significant figures, only the order of magnitude of the partial pressures is confident for the absolute measurement. In this study, most RGA data were used to investigate the relative difference of each partial pressure of gas and the change of partial pressure over time. Since most RGA data were used not for the absolute number but for the comparison, the RGA data was reported with one significant figure despite of the order of magnitude accuracy.

Once the instruments were installed to Materials Distillation Chamber, the RGA was turned on and measured the first spectra of partial pressure of gaseous element inside the chamber at the total pressure of 1.8×10^{-5} torr as measured by the Ion Gauge. The first RGA spectrum shown in Fig 6.3 indicates the initial dirty vacuum state with the peaks of overall elements from 1 to 200 amu including the high peaks of H_2 , H_2O , and N_2 .

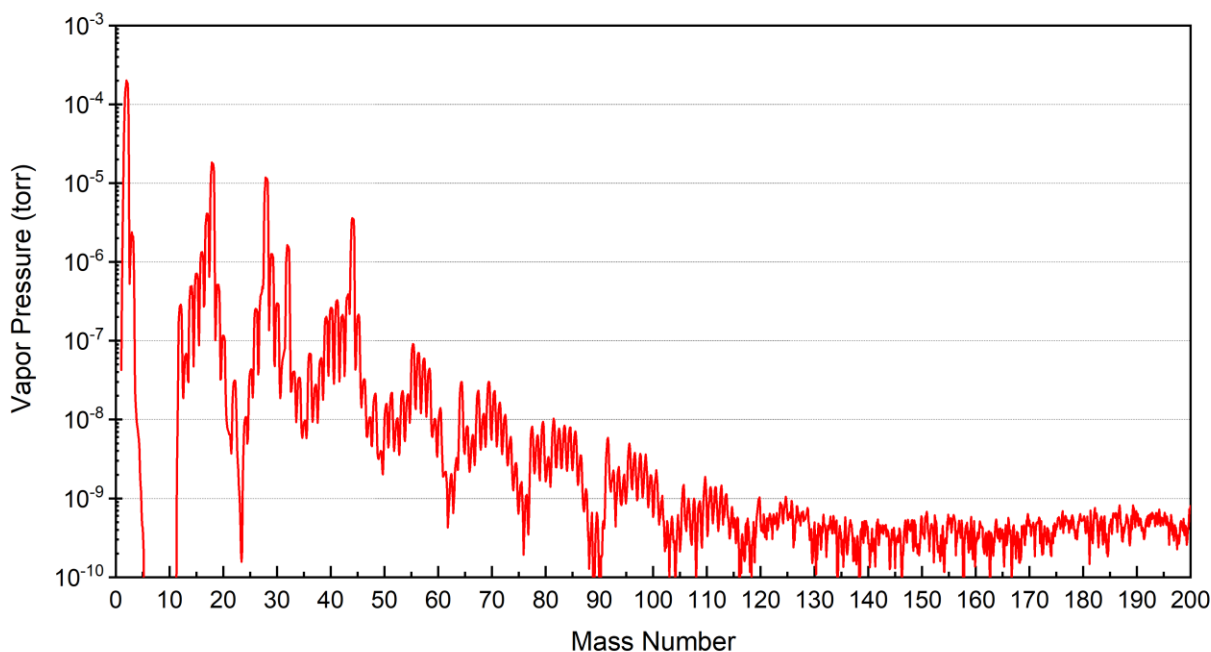


Fig. 6.3 The first RGA spectrum of materials distillation chamber after installation

After measuring the first RGA spectrum, the RGA was turned off and the source cell without the crucible was installed through the bottom 2.75 in CF flange of the chamber. The source cell (Varian E7-026, Serial No. 981-4314) was previously used as an aluminum cell in the MBE for GaAs/AlGaAs growth. As shown in Fig 6.4 and Appendix A, the source cell was composed of a heater for radiative heating covered with tantalum sheet. A thermocouple touching the bottom of the crucible measured the cell temperature. The power supply used to heat the cell was a GENH 20-38 (TDK-Lambda, Hamburg, Germany) capable of operating to 28 V and 30 A in DC.

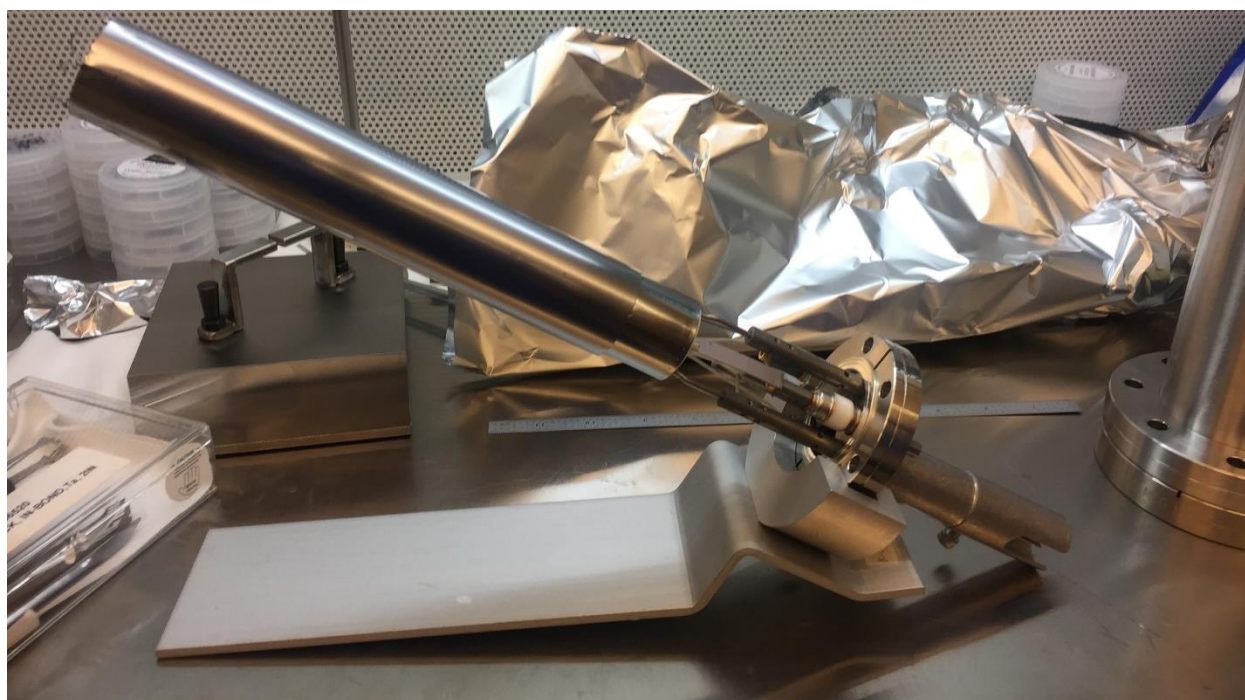


Fig. 6.4 Source cell (see Appendix A for detailed schematic)

Two days after installing the source cell, and with continued pumping, another RGA spectrum was measured as shown in Fig 6.5. The RGA spectrum showed a cleaner chamber than previously. Almost all elements with the mass number above 50 were removed and the amplitude of signals

of the elements with major peaks in the first spectra decreased in the spectra after the additional two days pumping.

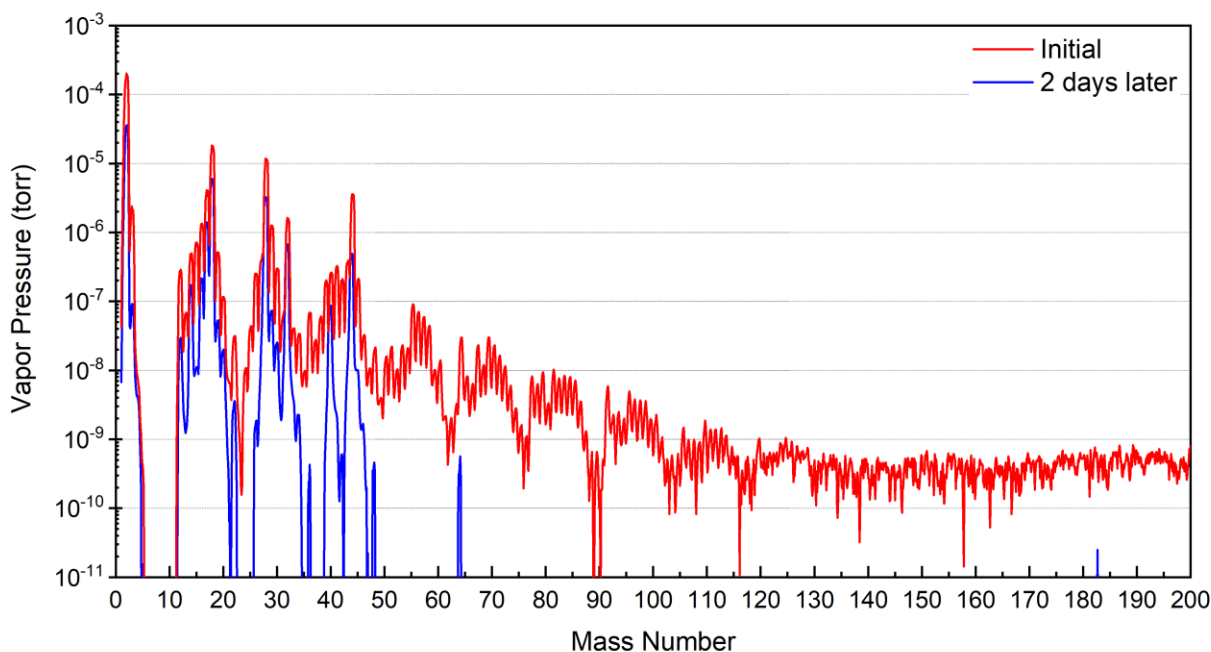


Fig. 6.5 RGA spectra from the chamber initial vacuum level (red) and after two days additional pumping (blue)

6.2 Chamber Baking and Leak Testing

In order to remove contaminants and improve the vacuum level, the chamber was baked with heating tape wrapped around the outside and also by heating the source cell inside, which also provided initial outgassing of the cell. Thus, the source cell was heated to ~ 733 K over five days and maintained at this temperature until the baking was finished. The total pressure of vacuum measured at the ion gauge before starting the cell heating was 7.8×10^{-6} torr. During heating of the

cell, the total pressure kept increasing and stabilized around 1.5×10^{-5} torr before baking of the chamber started.

For baking the chamber, heating tapes were attached to the chamber, as shown in Fig 6.6, and connected to a power supply. In order to insulate the chamber and reduce heat loss during baking, the chamber was covered with Al foil, as shown in Fig 6.7. Thermometers were placed on the surface of Al foils in order to monitor the temperature, which was not to exceed ~ 250 °C, as dictated by the allowed maximum temperature of each component of the chamber. Baking of the chamber started at low power (15%) held constant for 7 days. The temperature of the chamber measured from 80 to 120 °C depending on the location. The power was then increased to 50% over 3 days and held constant for 2 days more. Temperature measured from 150 to 250 °C, depending on the location.

The total pressure before baking the chamber and with the source cell at ~ 733 K was 1.5×10^{-5} torr. The total pressure during baking increased to as high as 4.9×10^{-5} torr due to the activated gases by increased temperature inside the chamber. The total pressure after baking and cooling the chamber to room temperature, but with the cell still at 733 K, was 1.6×10^{-5} torr, which was unexpectedly slightly higher than the total pressure before baking.

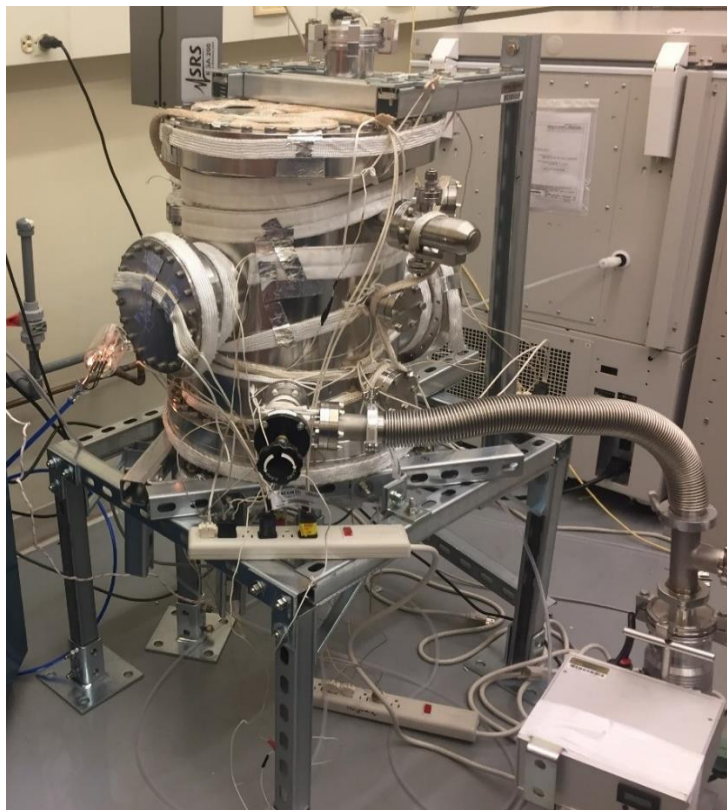


Fig. 6.6 Materials distillation chamber surrounded with heating tapes

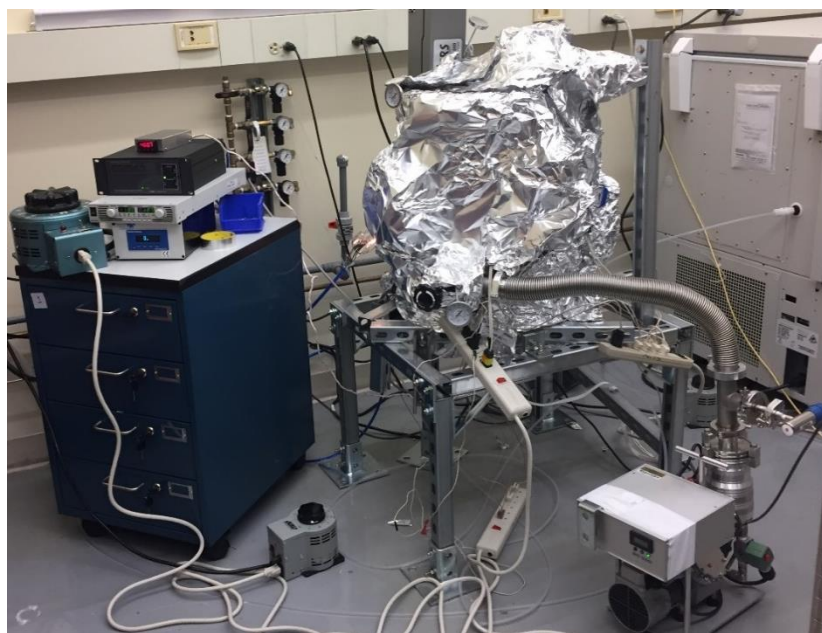


Fig. 6.7 Materials distillation chamber Al foils are covered with

The RGA spectra in Fig 6.8 also shows increased partial pressure of each gaseous element at room temperature after cell heating and chamber baking, compared with initial vacuum level. It shows high mass number are gone after the treatment. Figure 6.9 shows the RGA spectra before and after baking but before the cell cooling. Interestingly, the spectra are very similar, except after cooling there is a noticeably high amount of mass numbers 50 to 80 compared to before baking. Since these elements were appeared after baking started in the cell heating, there could be contaminants hidden and spread over the chamber during baking. These elements were not shown anymore after cell cooling. Consequently, the contaminants could be removed during cell heating after the completed baking or depressed below the detection limit as the cell temperature decreased. The molecules and elements with the mass number above 80, which mostly indicate organic film type contaminants in the spectrum after baking, slightly lower than that in the spectrum before baking, implying baking contributed to remove the contaminants. However, most gaseous elements below the mass number of 80, including air components such as N_2 , O_2 , and H_2O , rather increased after baking.

With the slightly increased total pressure from 1.5×10^{-6} torr to 1.6×10^{-6} torr, the increased partial pressure of most gaseous elements below the mass number of 80 could be due to the gaseous elements coming from the corner of chamber components previously hidden. However, this could be evidence of a leak, considering increased partial pressures of air components N_2 , O_2 , and H_2O . Therefore, the leak test was performed to check where the leaking point was.

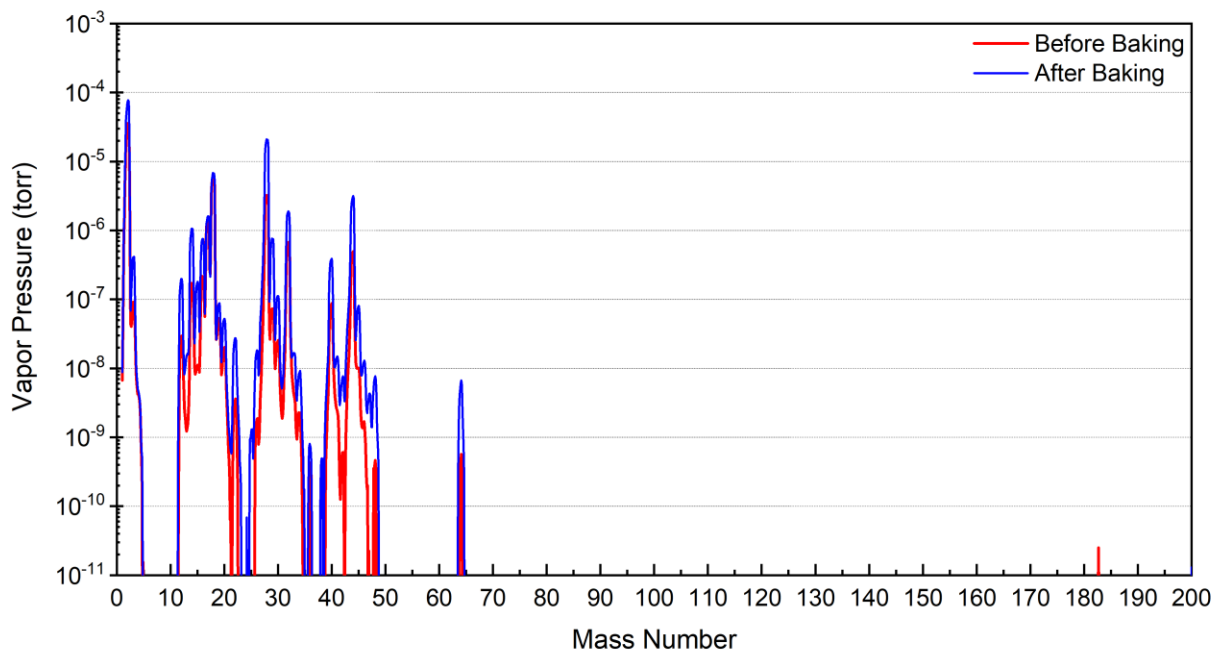


Fig. 6.8 RGA Spectra before (red) and after (blue) cell heating and chamber baking, chamber and cell at room temperature

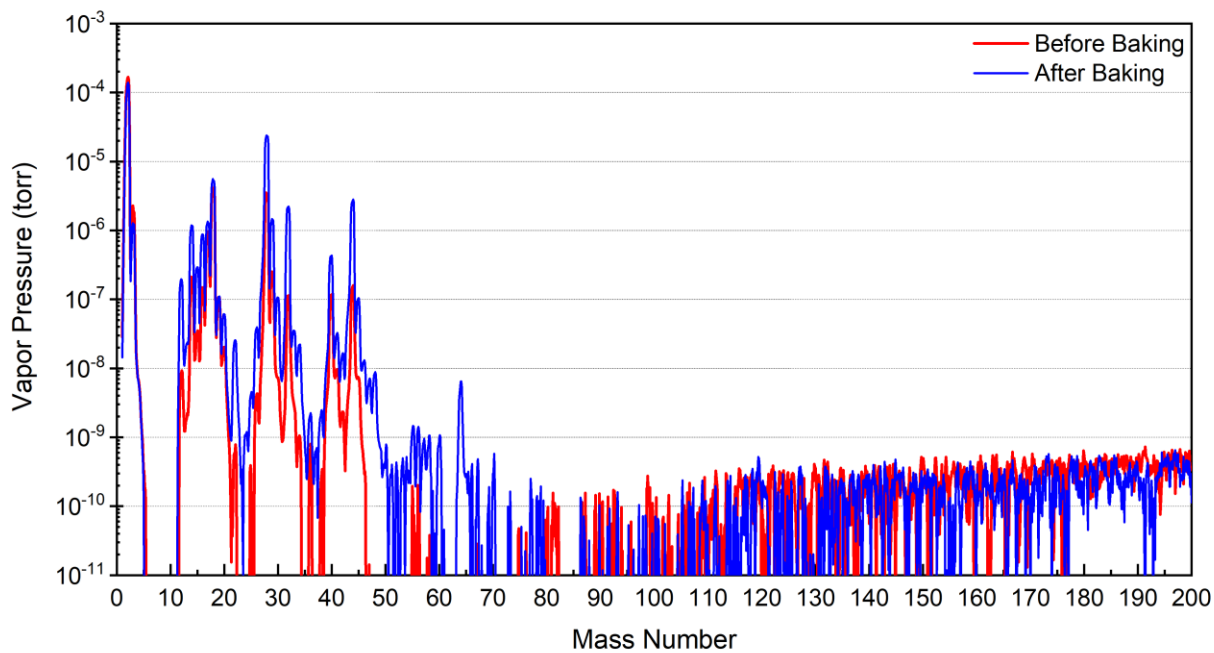


Fig. 6.9 RGA spectra before (red) and after (blue) chamber baking and cooling to room temperature, with cell at $460\text{ }^{\circ}\text{C}$ (733 K)

The leak test was performed using He gas tracking with the partial pressure of He measured by RGA. Flanges and components of chamber were isolated from each other by bagging each component to clarify the leaking point. Leaks were found in two 6-in flanges in the bottom of the chamber and the source cell and small leak was found in the 2.75 in CF flanges of the angle valve and pump connector and a 2.75 in CF flange placed near RGA.

After venting with Ar, the flanges with leaks were reinstalled, replacing gaskets. The small leaks found in 2.75 in CF flanges were fixed by installing again. However, leaks in the two 6-in flanges and the source cell in the bottom of chamber were not fixed. Investigating inside the chamber near the leaking flanges confirmed there was a 1-mm scratch on the knife edge causing the leak in the 6 in flange near the angle valve, as shown in Fig 6.10. Consequently, the scratched surface was ground lightly using honing stone to reduce the leak.

Another 6 in flange near the glass window also had a leak. It was discovered that the size of the flange on the chamber side was smaller than the standard gasket size and a larger gasket had been placed crookedly in the flange, which did not seal properly. The gasket was reduced by machining, and etching, then replaced to the 6 in flange. The 2.75 in CF flange of in the bottom for source cell installment had a misaligned gasket, which was repaired in a similar way.

After smoothing the scratch on the 6 in CF flange of chamber and replacing gaskets and reinstalling the source cell and another 6 in CF flange, the degree of leaking decreased. The total pressure of chamber was 1.20×10^{-6} torr at room temperature after pumping for a day. This is the decreased value compared with 1.56×10^{-6} torr before fixing the leaks.

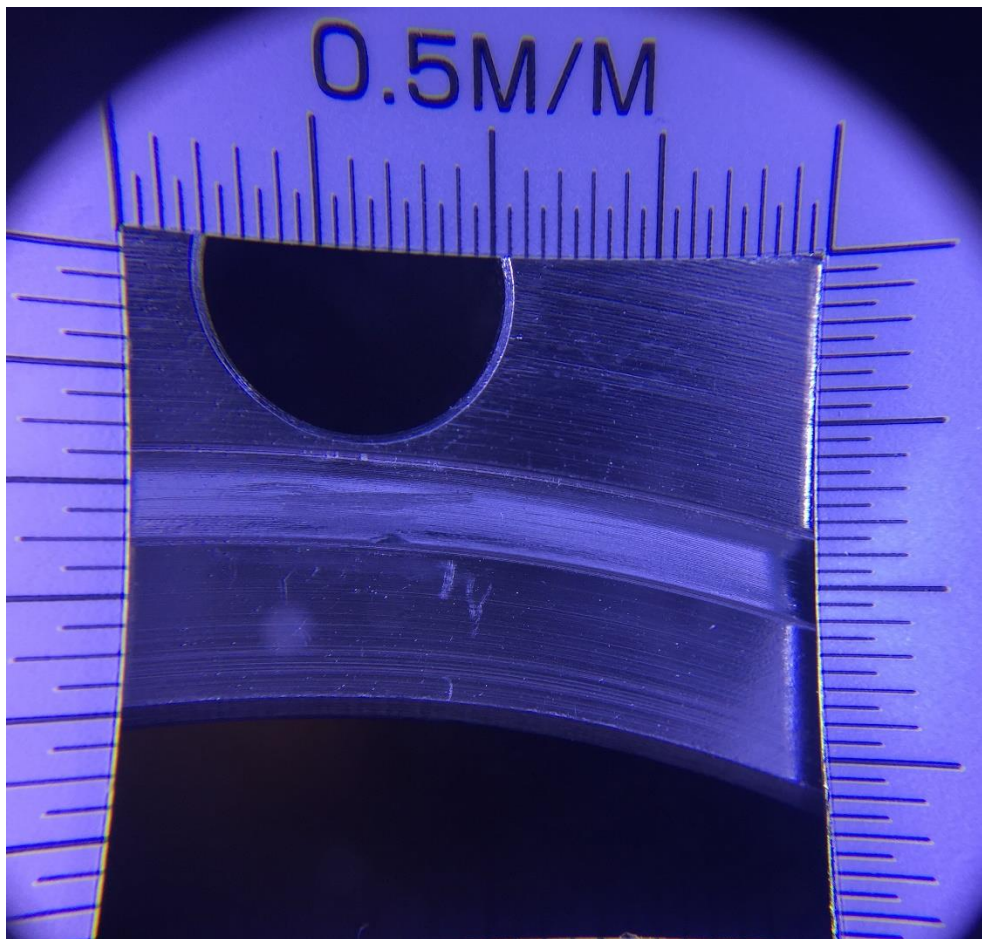


Fig. 6.10 Scratch approximately 1 mm long on knife edge of 6-in. CF flange on chamber bottom

6.3 Preliminary Experiment for Distillation of 7N Ga (Cell Outgassing, Crucible Outgassing and Power Increase Test)

After chamber backing, cell outgassing was performed again through 11 days to clean the cell. By increasing the power supply current in increments of 0.1~ 0.15 A, the cell temperature increased step by step at about 150 degrees per day, avoiding radical increase of total pressure of chamber due to contaminants coming off. When the cell temperature increased to 711°C, the power supply

reached the available current limit. Therefore, the power supply was replaced by GENH80-9.5 (TDK-Lambda, Hamburg, Germany) available to 80 V and 9.5 A in DC.

The cell was not totally cooled down when the power supply was replaced. Consequently, the second cell outgassing started from 523 K and heated with the higher current increase of ~ 0.5 A because cell was cleaner and thus smaller increase in total pressure was observed. The cell temperature increased to 1478 K, which was ~ 100 degree above the distillation temperature of 1360K, and maintained at the temperature for 1 h. The current and voltage producing the temperature of 1478 K were 4.85 A and 48.72 V corresponding to 237 W. The current and voltage producing the distillation temperature of 1360 K were 4.35 A and 41.56 V corresponding to 181 W. Once the cell was outgassed at the peak temperature of 1478 K, cooled down and maintained at ~ 877 K for a day and ~ 762 K for another day. Then the cell was cooled down to room temperature for venting to load the crucible

The crucible loaded for distillation experiment was pyrolytic boron nitride (PBN) crucible (Union Carbide, Huston, TX) of lot number 5353 and serial number H6814. As shown in Fig 6.11, the shape of PBN crucible was conical with concave curvature of bottom. The wall thickness was X mm and the contained volume of the crucible was 13 cm^3 . The crucible was loaded to the cell and the chamber through Ar bag as shown in Fig 6.12.

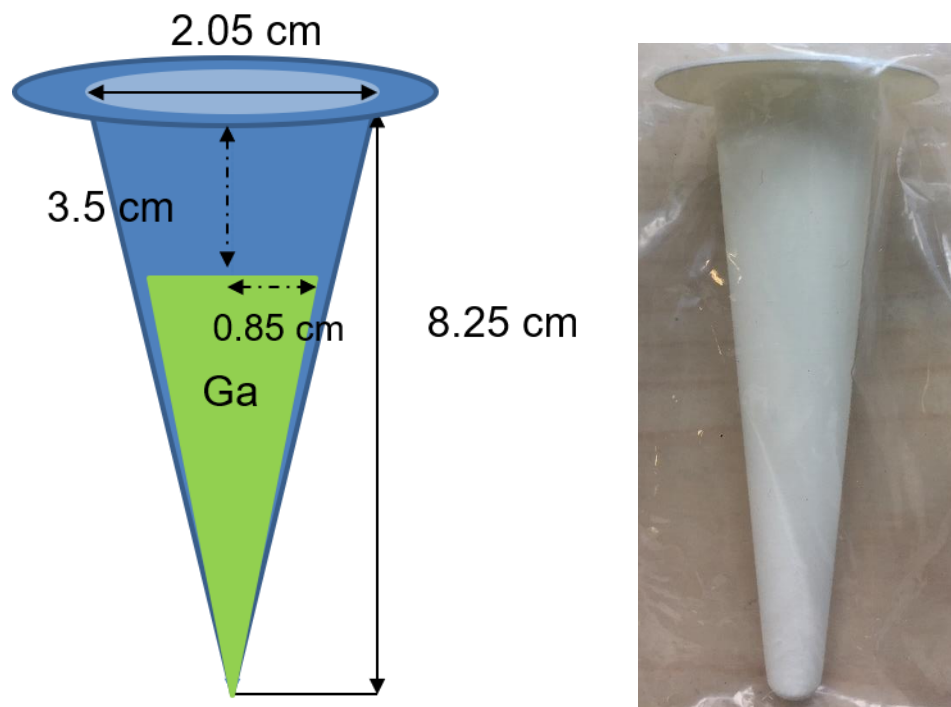


Fig. 6.11 Schematic drawings and picture of PBN crucible

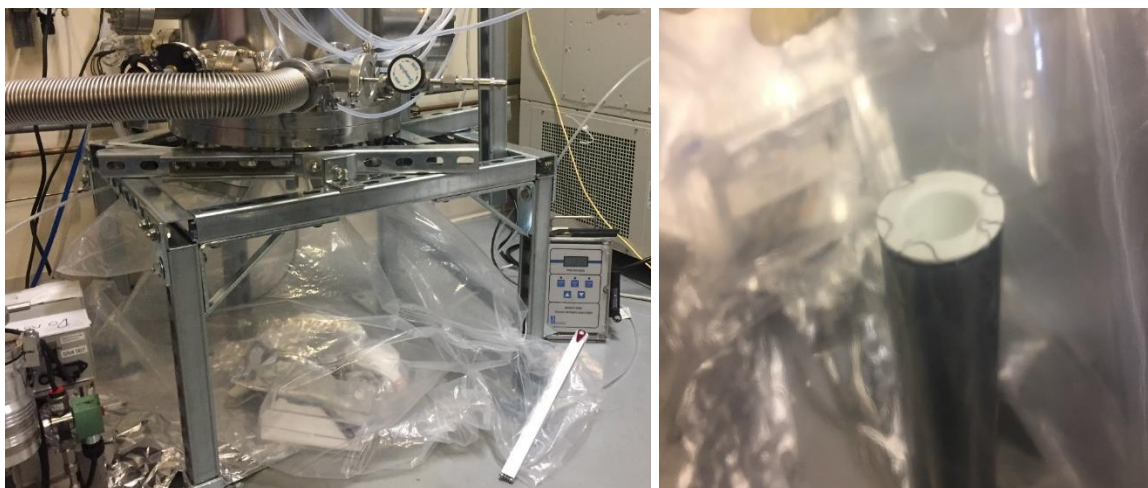


Fig. 6.12 Ar bag placed below chamber for crucible loading and the loaded crucible to the cell inside the Ar bag

Before loading and outgassing, the PBN crucible was cleaned by the following procedure.

1. Rinsed the crucible with DI water (in cleanroom) 2~3 times.
2. Soaked the crucible in 20% HNO₃ (diluted from 69 % Aristar Ultra HNO₃) for 24 hours (in Teflon bottle).
3. Rinsed the crucible with DI water again 2~3 times.
4. Soak the crucible in DI water for 15 min.
5. Nitrogen Purging.
6. Covering with cleaned UHV aluminum foil (UHV foil cleaned by standard isopropanol and methanol)
7. Crucible heated in the O₂ flow furnace, drying the crucible.

Crucible outgassing was performed four times; once purely for outgassing crucible to eliminate contaminants, and the other three times for the investigation of the temperature response of crucible in the cell to the power supplied and for minimization of the transient temperature.

In the first crucible outgassing, the crucible and the cell were heated to 1490 K, which is ~ 130 K above the distillation temperature of 1360 K. The starting total pressure was 1.1×10^{-5} torr. The current was raised in ~ 1 A increments, as shown in Fig 6.13, considering the cell outgassing data of temperature response to the current applied and the fact that the cell already experienced outgassing. Because significant amounts of compounds remained on the crucible due to acid washing and emitted as gases during heating, these intensified the total pressure with the activated gases due to the temperature increase. Therefore, once the current increased and thus temperature

increased with increasing total pressure, approximately 30 min was required until the total pressure stabilized then depressed.

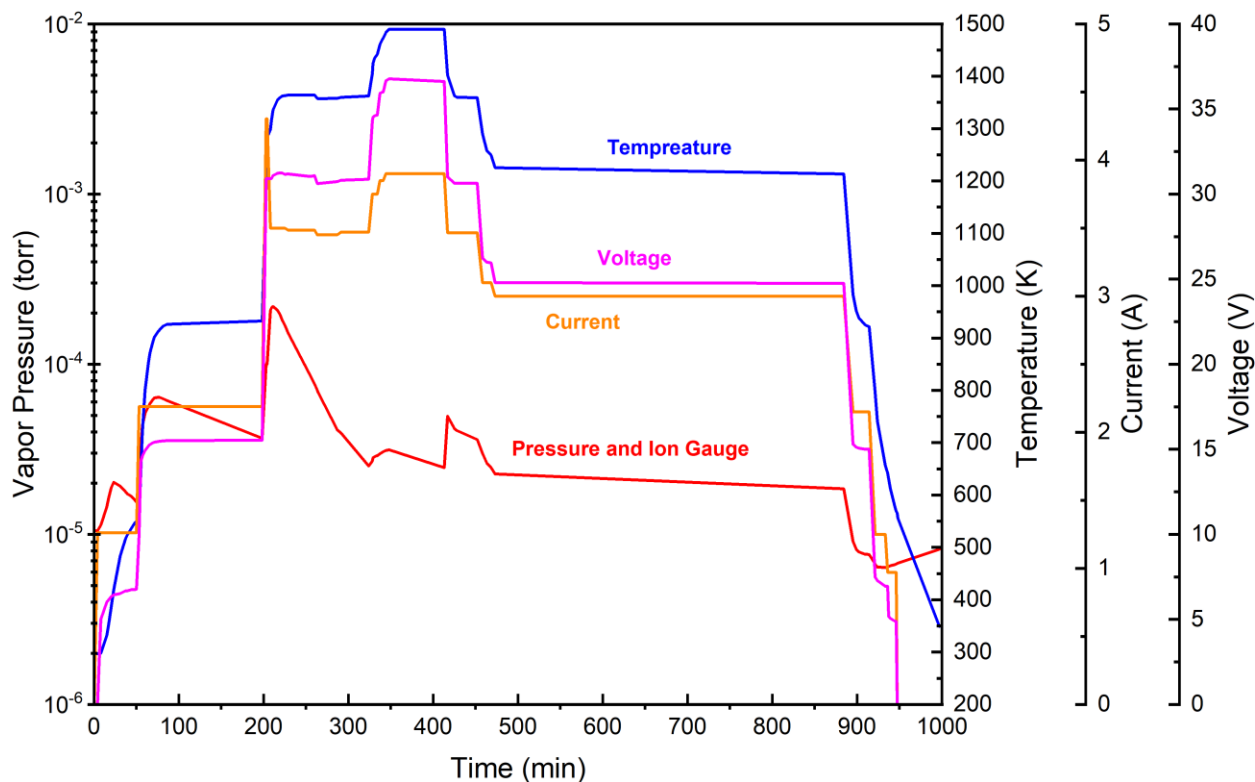


Fig. 6.13 Experimental parameter change during the first crucible outgassing

When the current was 2.2 A, the current increased to directly 4.3 A instead of 3.2 A. This is because the temperature reached ~ 932 K at 2.2 A and was expected to increase to the distillation temperature by setting 4.3 A. However, the rate of increasing temperature was too large, and thus the total pressure radically increased to above the 2×10^{-4} Torr. The current immediately changed to 3.5 A to decrease the rate of increasing temperature and depress the total pressure. After the temperature reached 1490 K, at the current of 3.9 A and the voltage of 36.62 V, corresponding to the power of ~ 143 W, the crucible outgassed for an hour at the 1490 K. After an hour, the temperature of the crucible and cell decreased to 1213 K and stayed at that temperature for 8 hours.

The current and voltage at the distillation temperature of 1360 K were 3.465 A and 30.63 V, corresponding to the power of ~ 106 W. Compared to power of ~ 181 W at the 1360 K for the cell alone being heated, about 75 W decreased in the crucible outgassing. The temperature decreased until 566 K by decreasing the current to 1 A and then power was turned off.

Unlike MBE systems where the cell is automatically heated to the preset temperature, with a temperature ramping rate of 25 ~ 30 degree/min fixed by the PID controller, the cell of Materials Distillation Chamber was heated to the temperature by manually controlling the power supply. If the time in transient temperature was significant, particularly near the distillation temperature of 1360 K, the evaporation in the transient temperature would not be negligible. Consequently, the transient time should be minimized.

However, directly increasing the current of power supply to the current corresponding to the distillation temperature of 1360 K, in order to minimize the time at transient temperature would cause the total pressure of Materials Distillation Chamber to increase 1000 times higher than the total pressure of MBE system and over the operation limit of RGA, as experienced in the first crucible outgassing. Moreover, for the safety of the cell and crucible, the rate of temperature increase should be maintained to 25 ~ 30 degree per minute.

For these reasons, additional crucible outgassing steps were performed to simulate the heating and cooling of the Materials Distillation Chamber in the sample loading, minimizing the transient temperature and optimizing the increasing rate of current. In the second crucible outgassing as shown in Fig 6.14, the current applied at each step was determined based on the first crucible

outgassing, and then applied to the power supply, while still monitoring the total pressure and the rate of increasing temperature. Unlike the first crucible outgassing where there was large increase in total pressure due to the gaseous elements emitted from the crucible surface, the total pressure was maintained below 10^{-4} torr in the second crucible outgassing because the crucible was once cleaned by the first crucible outgassing. However, in the temperature range of 1100 ~ 1140 K, a larger temperature increasing rate than 30 deg/min was observed and there was a spare to increase the temperature faster in other temperature ranges. Consequently, additional outgassing was performed.

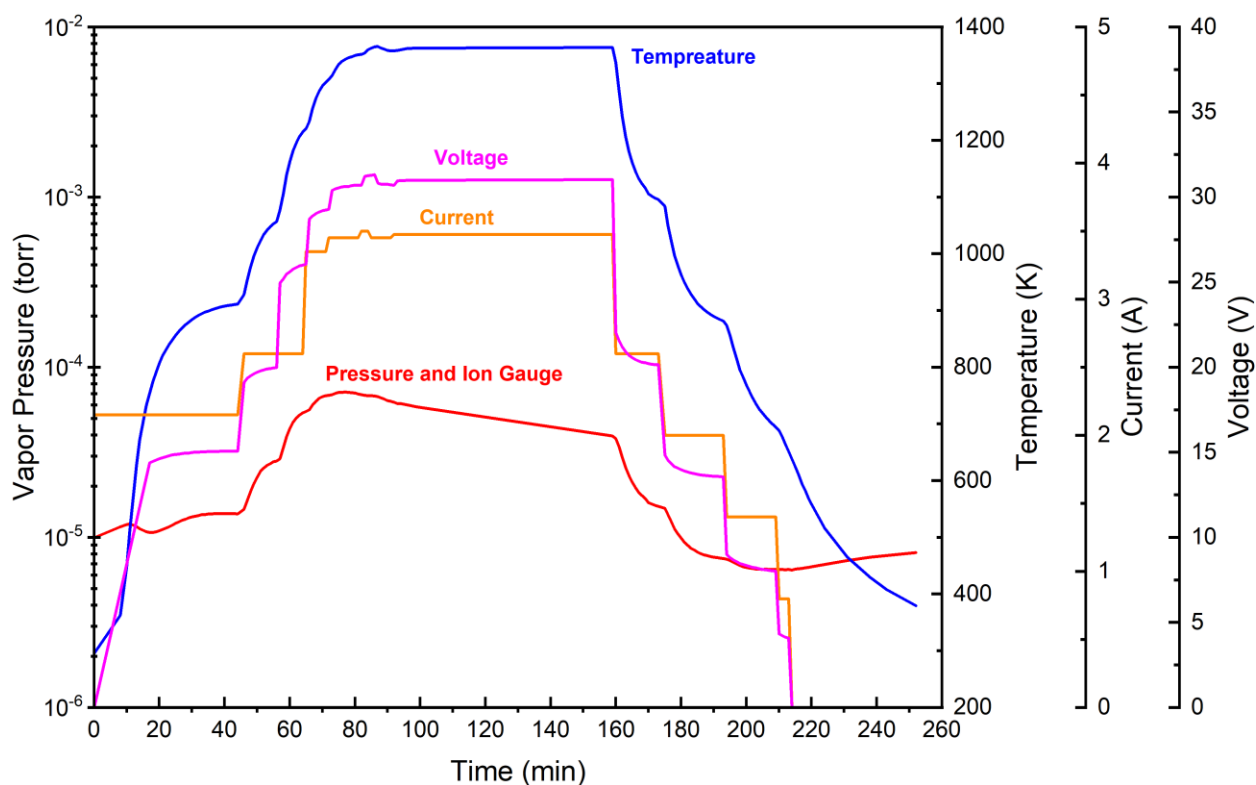


Fig. 6.14 Experimental parameter change during the second crucible outgassing

In the third outgassing, the current increased immediately after the temperature ramping rate fell below 17/min. As shown in Fig 6.15, the time at transient temperature during heating decreased to

about an hour. In the cooling of the third outgassing, the current decreased by ~ 0.3 A. However, the temperature decreasing ramp rate was not faster than increasing ramp rate when the same current applied in the heating. For an additional test for the optimization in cooling, the temperature increased from 972 K again for the fourth outgassing as shown in Fig 6.16. In the cooling of the fourth outgassing, the current decreased by 0.4 A within a shorter time than for the third crucible outgassing. The temperature decreased to 947 K, and was maintained at that temperature until the venting for a Ga sample loading to keep clean the chamber.

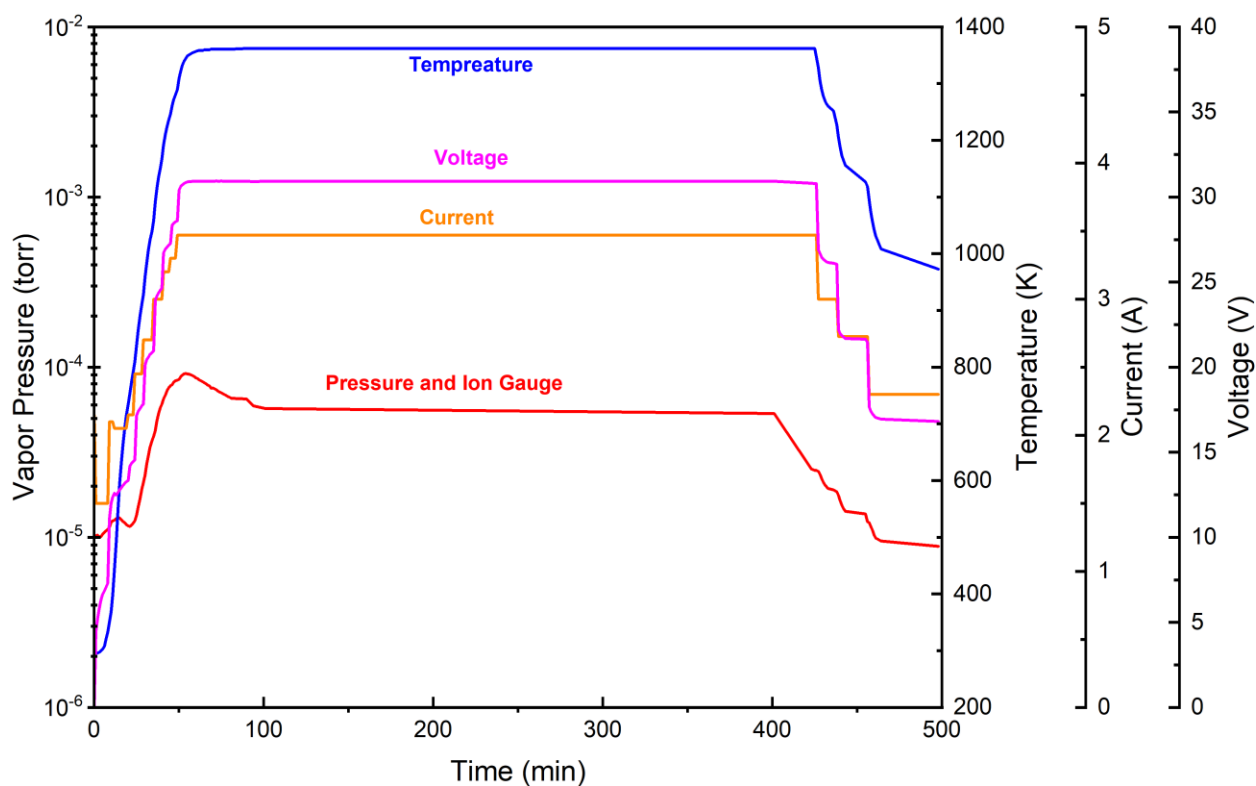


Fig. 6.15 Experimental parameter change during the third crucible outgassing

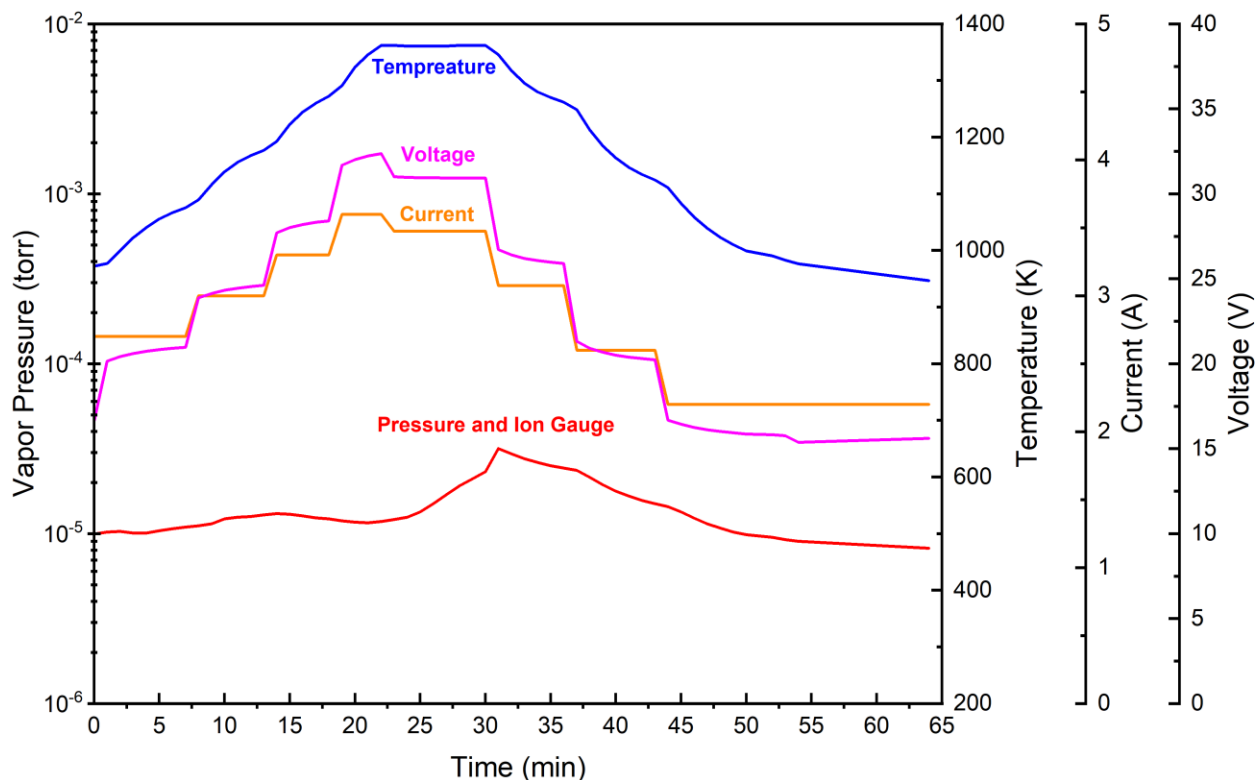


Fig. 6.16 Experimental parameter change during the fourth crucible outgassing

From the multiple tests of crucible outgassing, the current that generated the temperature of 1360 K was confirmed to 3.47 A when the crucible and cell were together. When Ga loaded to the crucible, the required current to reach the 1360 K was expected to be slightly lower than the 3.47 A because less power was required due to the Ga sample loading. Although the required current at the 1360 K in the distillation of Ga was expected to be lower than 3.47 A, the current to 3.47 A was employed near and below the distillation temperature, and then decreased the current when the temperature reached the target temperature. This was to reach the target temperature as soon as possible and minimize the time at transient temperature.

6.4 Distillation Experiment

The sample of the distillation experiment was a 7N Grade Ga single ingot of 25g (Alcan, Lot No. AEM 7/605). For the sample loading, the vacuum chamber was vented with Ar injection. Near the cell, an Ar bag was attached as was performed in the crucible loading in Fig 6.12 to maintain the clean chamber during venting and sample loading. Inside the Ar bag, the cleaned tools and the sample of 7N Ga wrapped with double polyethylene bag were placed. The quality of Ar bag was monitored with an oxygen center not to be higher 100 ppb, injecting Ar frequently. When the chamber was totally filled with Ar, the cell with the crucible was extracted inside the Ar bag. The polyethylene vinyl of Ga sample was removed while still inside the Ar bag and the Ga sample was directly loaded to the crucible on the cell. Then the cell was quickly loaded to the chamber. Since the Ga sample ingot was irregular but close to a rod shape, the Ga sample was able to put in the crucible due to the smaller circumference of the sample than crucible inner circumference, although some part of Ga sample stuck out of the conical shape of the crucible.

After completing the Ga loading, the chamber was pumped down for 24 hours. The total pressure measured at the ion gauge for this spectrum was 9.3×10^{-6} torr. The RGA spectra of the chamber at room temperature immediately before the cell heating for distillation is indicated in Fig 6.17. The starting condition of $P(\text{O}_2)$ was 3.0×10^{-6} torr, $P(\text{N}_2)$ was 3.2×10^{-6} torr and $P(\text{H}_2\text{O})$ was 5.8×10^{-6} torr. All species above the mass number of 50 were shown to be cleaned to the below the detection limit of 10^{-12} torr except for the specie with mass number 64, which is presumed to be SO_2 at $\sim 2 \times 10^{-9}$ torr.

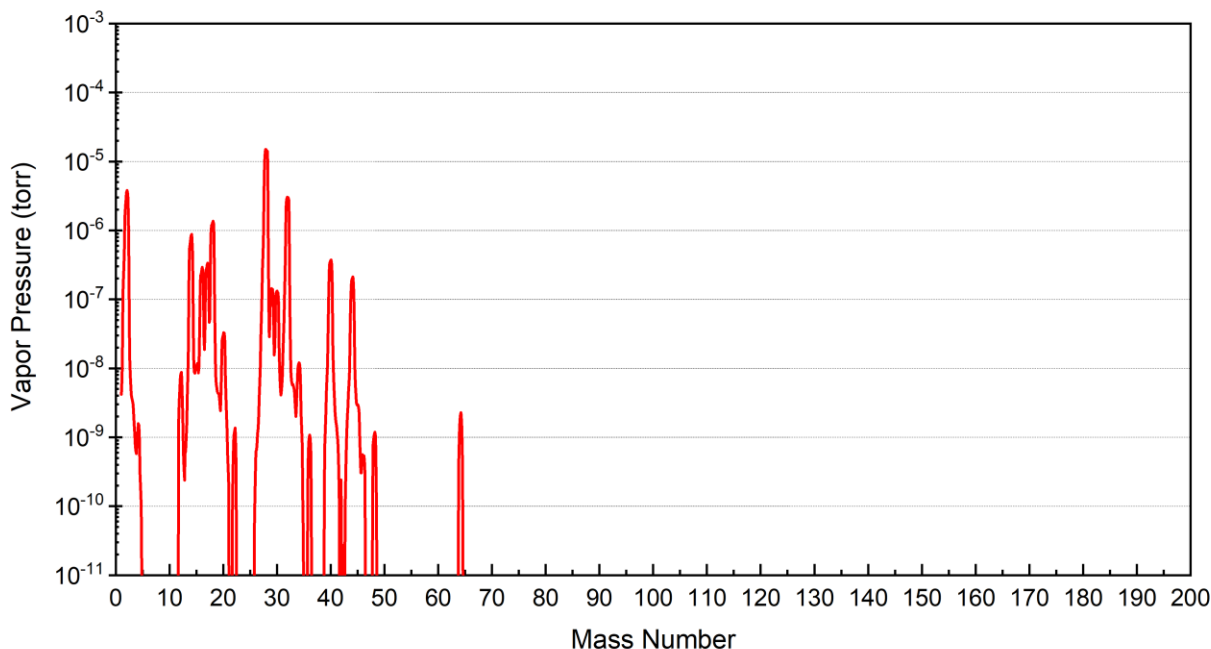


Fig. 6.17 RGA spectrum of the Materials Distillation Chamber before distillation experiment

The in-situ MBE distillation was performed for 16 h with 400 h distillation resulting in high Ge loss. Since the distillation and growth were performed together in the in-situ MBE distillation, the stage when Ga and impurities are lost was not uncertain. However molecular distillation theory suggested more Ga and impurity losses are expected. Also, the efficacy of Ge loss through Ge active oxidation at the distillation temperature should be proved in the molecular distillation experiment. Therefore, same time range of 16 h as the in-situ MBE distillation was applied to the molecular distillation experiment. The calculation of Ga evaporation from the PBN crucible suggested the Ga loss of ~ 6.4 g for 16 hours distillation (as explained in Chapter 3). In order to protect the pump from possible excessive Ga flux in the distillation experiment during high temperature heating for 16 hours, additional bellows were installed between the chamber and pump and soaked into liquid nitrogen, as shown in Fig 6.18, to trap the evaporated Ga through condensation in the bellows. This trap in liquid nitrogen contributed to lowering the total vacuum

pressure slightly from about 1.0×10^{-5} torr to 9.3×10^{-6} torr at room temperature before cell heating for the distillation experiment.



Fig. 6.18 Traps connected to the chamber in liquid nitrogen

The experimental parameters for the distillation of ${}^7\text{N Ga}$ are indicated in Fig 6.19. During heating, the temperature reached the distillation temperature of 1360 K in 73 min. The distillation at 1360 K was performed for 16 hours. During cooling, the temperature was controlled down to 773K and then the power was turned off. Throughout the entire experiment, the RGA was turned on to monitor the chamber spectra. Since the total pressure exceeded the limitation of CDEM mode operation, the RGA was operated only in the Faraday cup mode.

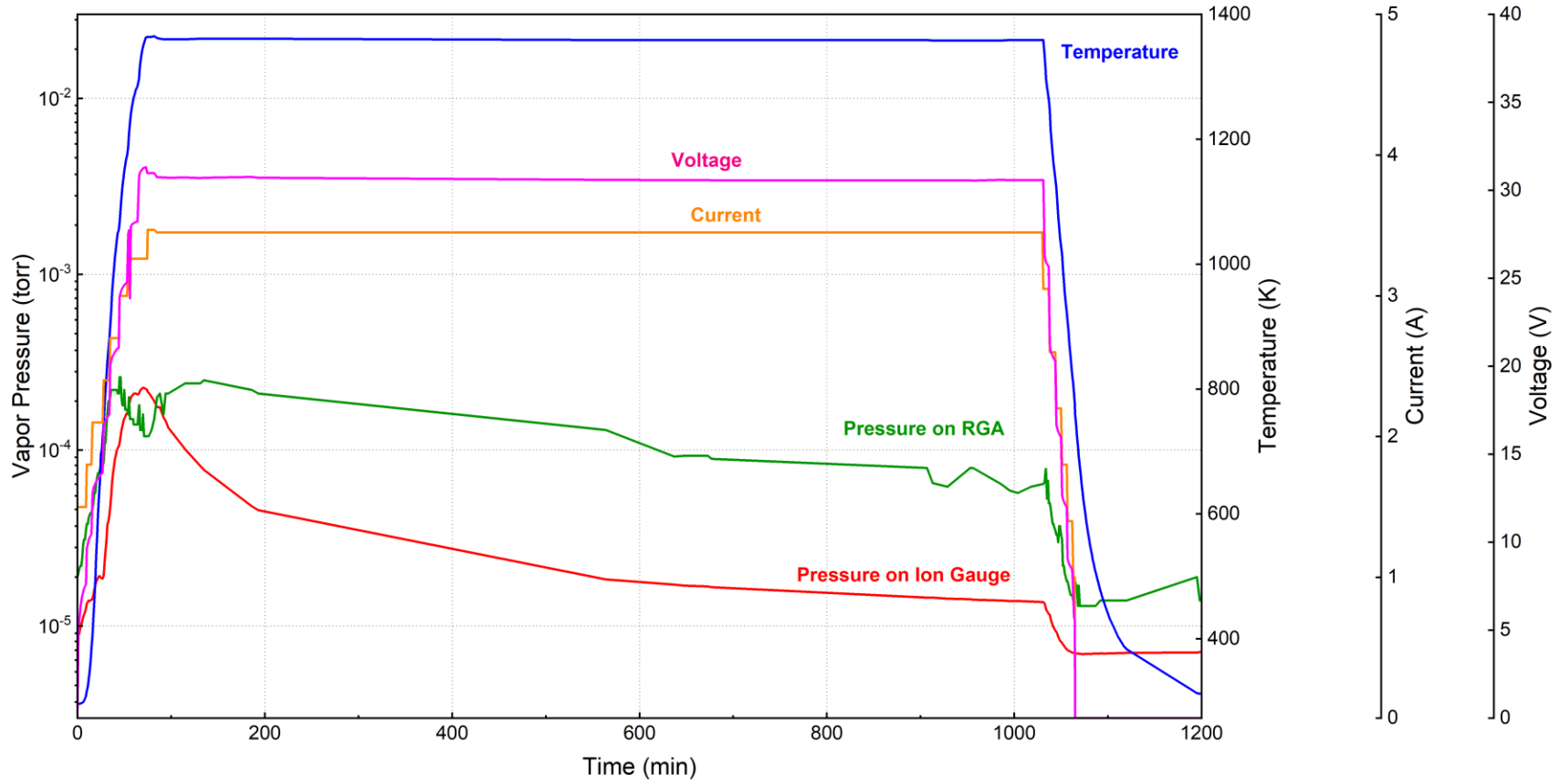


Fig. 6.19 Changes of experimental parameters during distillation of 7N Ga

The cell was placed 9.1 in (24.1 cm) below the top of the chamber, as shown in the schematic diagram in Fig 6.20. However, the distance from the top of the crucible to the top of the chamber is expected to be ~ 24 cm, slightly smaller than 24.1 cm. The crucible was almost fit to the empty space of the cell right above the thermocouple, but slightly flush with the top of the cell as shown in Fig 6.12. Thus, the distance from the top of the crucible to the top of the chamber was smaller than that from the top of the cell.

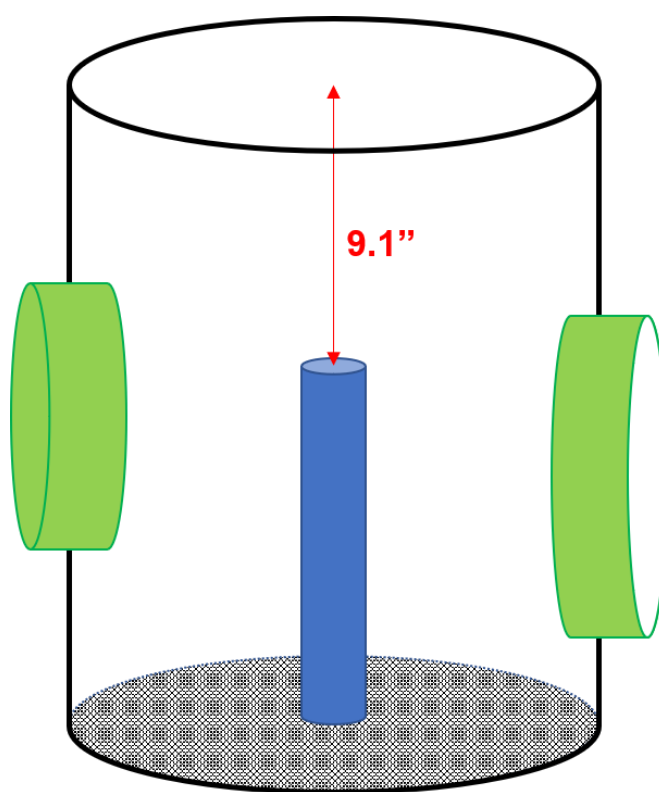


Fig. 6.20 Schematic diagram of the chamber cell installed

As mentioned earlier, the single 7N Ga ingot was placed in the crucible. As shown in left picture of Fig 6.21 some part of it stuck out above the crucible, when 7N Ga sample was loaded to the chamber before heating. Nine minutes later, the cell heating was started. When the cell temperature was 309 K, the Ga ingot was found to be melted inside the crucible, as confirmed in the center

picture of Fig 6.21. At the distillation temperature of 1360 K (1087 C), the crucible was glowing hot, consistent with the high temperature, as shown in right picture of Fig 6.21.

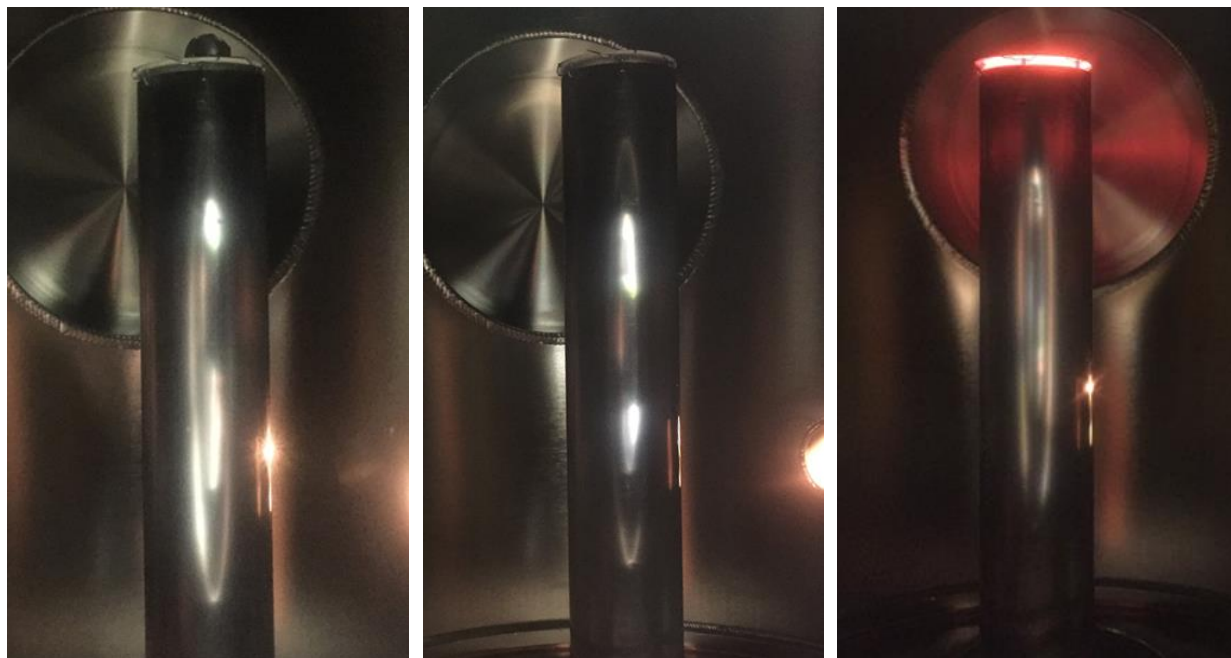


Fig. 6.21 Gallium sample in the crucible before heating (left) , 10 min later heating started and at 309 K (center) and during distillation at 1360 K (right)

About 24 hours after completing the distillation experiment, the chamber was vented and the remaining Ga from the distillation was extracted. Through the 10-in flange under an Ar bag, the crucible was pulled out of the cell and moved to the acid-cleaned PTFE bottle and the lid of bottle was closed. The PTFE bottle was moved out of the Ar bag and weighed on the scale for Ga weight change during the distillation experiment. After measuring the weight of the PTFE bottle with the crucible, the bottle was moved back to the Ar bag, the lid was opened, and the recovered Ga sample was poured to the cleaned 15 ml polypropylene test tube and enclosed with the lid and then micropara film for GDMS analysis.

6.5 Results and Discussion

The molecular distillation experiment was analyzed in three different ways. One is the measurement of Ga loss by weighing Ga before and after distillation. Another is the impurity concentration measurement by GDMS analysis, comparing with the GDMS analysis of the starting 7N Ga (same high-Ge lot as the in-situ MBE distilled and recovered Ga). The last method was the RGA monitoring during the distillation time.

6.5.1 Gallium Recovered

Direct measurements indicated only 0.2 g or about (1%) of Ga loss during the molecular distillation experiment. This is smaller than the Ga loss from the in-situ MBE distillation and growth campaign (~25%) due to the much longer overall MBE time of distillation, growth and idling at high temperatures. The measured amount is also smaller than predicted by the upper-bound analysis for molecular evaporation of Ga at 1360 K for 16 h.

6.5.2 GDMS Analysis

The recovered Ga sample after distillation was analyzed by GDMS. The GDMS results of the recovered Ga were compared with the GDMS analysis for the 7N Ga in the same lot as the recovered Ga. The elements that decreased and increased in concentration are listed in Table 6.1 and Table 6.2, respectively. The full details of GDMS results are given in Appendix B.

Table 6.1 Decreased element in distillation

Element	Before Distillation (ppb)	After Distillation (ppb)
S	0.6	< 0.5
Ge	440	< 10

Table 6.2 Increased element in distillation

Element	Before Distillation (ppb)	After Distillation (ppb)
O	10	300
Na	< 0.1	1.1
Al	< 0.1	0.3
Si	< 0.5	2
Cl	0.8	3
Fe	< 0.1	0.8
Zn	< 0.5	2
In	< 0.1	10

Sulfur concentration decrease, but the difference was negligibly small and near the detection limit. Thus, those concentrations are considered to be the same. The major concentration decrease was found in Ge, from 440 ppb to below the detection limit of 10 ppb. This corresponds to a Ge loss of 10 μg , neglecting the small Ga loss. Following the evaporation analysis earlier, the maximum possible (upper-bound) Ge loss solely by atomic evaporation is only ~ 24 ng from the crucible of Fig 6.11 for 16 h distillation at 1360 K. Therefore, the large loss of Ge in the molecular distillation experiment cannot be explained in the Ge atomic evaporation.

In Chapter 5, the vapor species diagram was discussed to explain Ge oxidation for the dilute Ge in Ga, and the equilibrium vapor pressure of GeO was significantly larger than the vapor pressure of Ge even at very low $P(\text{O}_2)$. From the vapor species diagram of 440 ppb Ge as shown in Fig 6.22, the Ge oxidation mechanism was found to be direct active oxidation at the $P(\text{O}_2)$ of 3×10^{-6} torr. The equilibrium $P(\text{GeO})$ at the $P(\text{O}_2)$ of 3×10^{-6} torr was 4.22×10^{-5} atm (0.032 torr), which was about 1000 times higher than the equilibrium vapor pressure of Ge. Using the derived equilibrium

$P(\text{GeO})$ and the evaporation rate equation of (2.1), the maximum Ge loss in GeO is ~ 0.02 g at the Ga surface area of 2.27 cm^2 for 16 h distillation. Consequently, the Ge loss of $10 \text{ }\mu\text{g}$ found in the GDMS analysis can easily be explained by Ge active oxidation into GeO. The formation and evaporation of GeO will be investigated further in the analysis of RGA spectra.

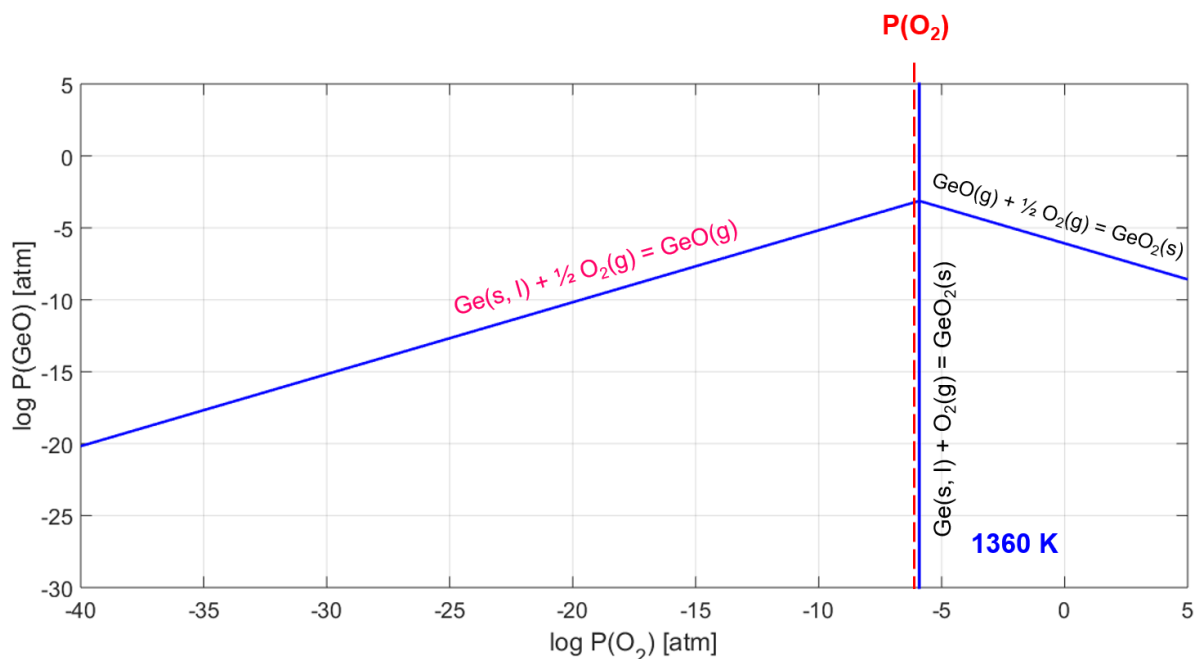


Fig. 6.22 Vapor Species diagram for 440 ppb Ge-O system at 1360 K

6.5.3 Analysis of RGA spectra during distillation

During the entire distillation, the gases inside the chamber from the mass number of 1 to 200 were monitored by RGA in vapor pressure (torr) unit. Since GeO is a gaseous species, the GeO produced can be measured in the mass numbers of 86 ($^{70}\text{Ge}^{16}\text{O}$), 88 ($^{72}\text{Ge}^{16}\text{O}$) and 90 ($^{74}\text{Ge}^{16}\text{O}$). Hence, the $P(\text{GeO})$ and $P(\text{O}_2)$ measured in the RGA were plotted with the cell temperature and total vapor pressure measured on the ion gauge in Fig 6.23. As shown in Fig 6.23, the vapor pressure signals

above the detection limit were measured for the mass numbers of 86, 88 and 90. The amplitude of signal reached $\sim 9 \times 10^{-9}$ torr at the maximum value when the temperature just reached the distillation temperature. The amplitude of signal decreased but lasted for additional ~ 8 hours. During this time, $P(\text{O}_2)$ decreased as temperature increased and distillation proceeded. Moreover, $P(\text{O}_2)$ decreased even as total pressure increased. When the $P(\text{O}_2)$ was minimum, the RGA signals of mass numbers of 86, 88 and 90 were at their maximum.

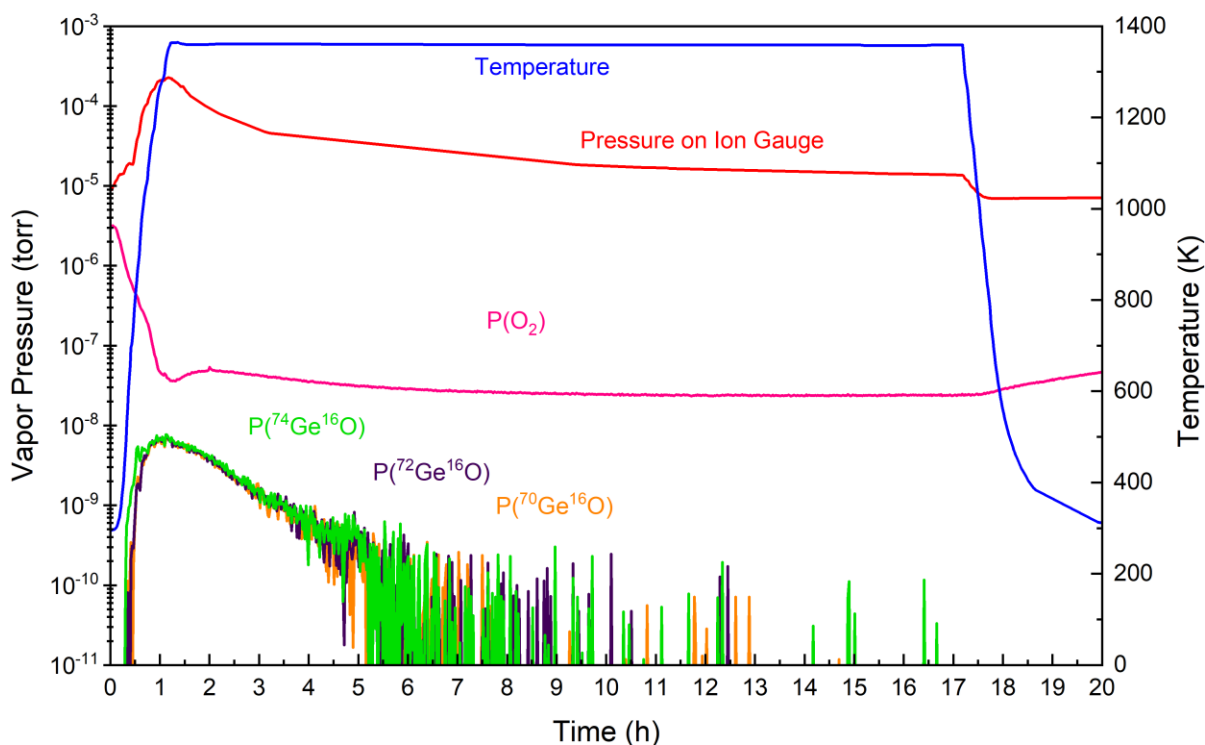


Fig. 6.23 RGA monitoring for $P(\text{O}_2)$ and $P(\text{GeO})$ with total pressure during distillation of 7N Ga

The behavior of $P(\text{O}_2)$ was different from other gases in Fig 6.24. The RGA signals of most gases increased as total vapor pressure increased and temperature increased during the transient time. Although $P(\text{N}_2)$ decreased once during temperature ramp up transient time, it radically increased by almost 100 times and then was stabilized as the total pressure was stabilized. In summary, most

pressures of major gases measured in the RGA had behavior similar to the total pressure, while $P(\text{O}_2)$ radically decreased and then stabilized at significantly lower signals than the initial signal, regardless of total pressure increase, as temperature increased.

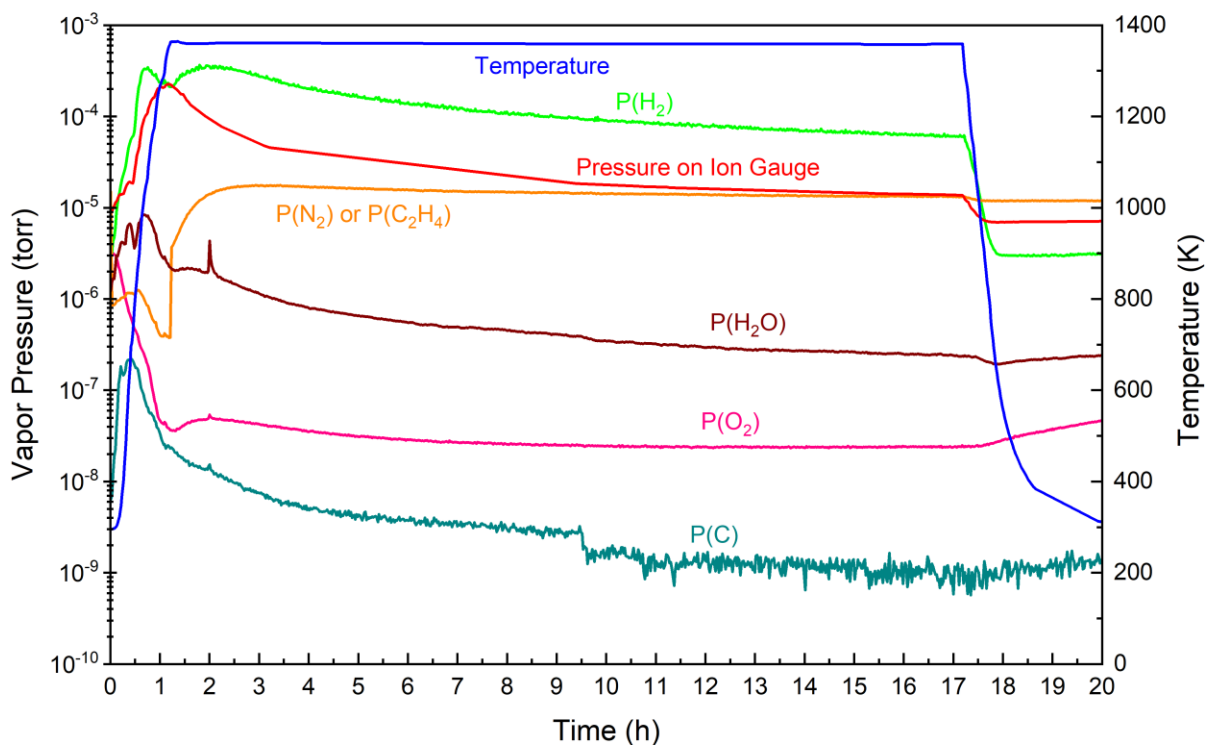


Fig. 6.24 Major gases measured in the RGA showing the decreased $P(\text{O}_2)$ during distillation of 7N Ga

In order to clarify the sources of RGA signals measured during the distillation of 7N Ga, the RGA signals measured during the second and third outgassing were also indicated in Fig 6.25 and Fig 6.26 for $P(\text{O}_2)$ and $P(\text{GeO})$. Also, the RGA signals of major gaseous elements measured during the second and third outgassing were also indicated in Fig 6.27 and Fig 6.28 as references in the absence of the Ga sample with high Ge. The RGA monitoring for the first crucible outgassing was excluded because RGA was not monitored during the entire first outgassing due to high vapor pressure above 2×10^{-4} torr. Furthermore, residual elements on the PBN crucible from nitric acid

and water during cleaning were outgassed during the first crucible outgassing. Also, the first crucible outgassing was not performed using the same routine as the distillation of 7N Ga and the second and the third crucible outgassing for the minimization of transient temperature. Consequently, the first crucible outgassing RGA data were not directly comparable with the distillation of 7N Ga RGA data.

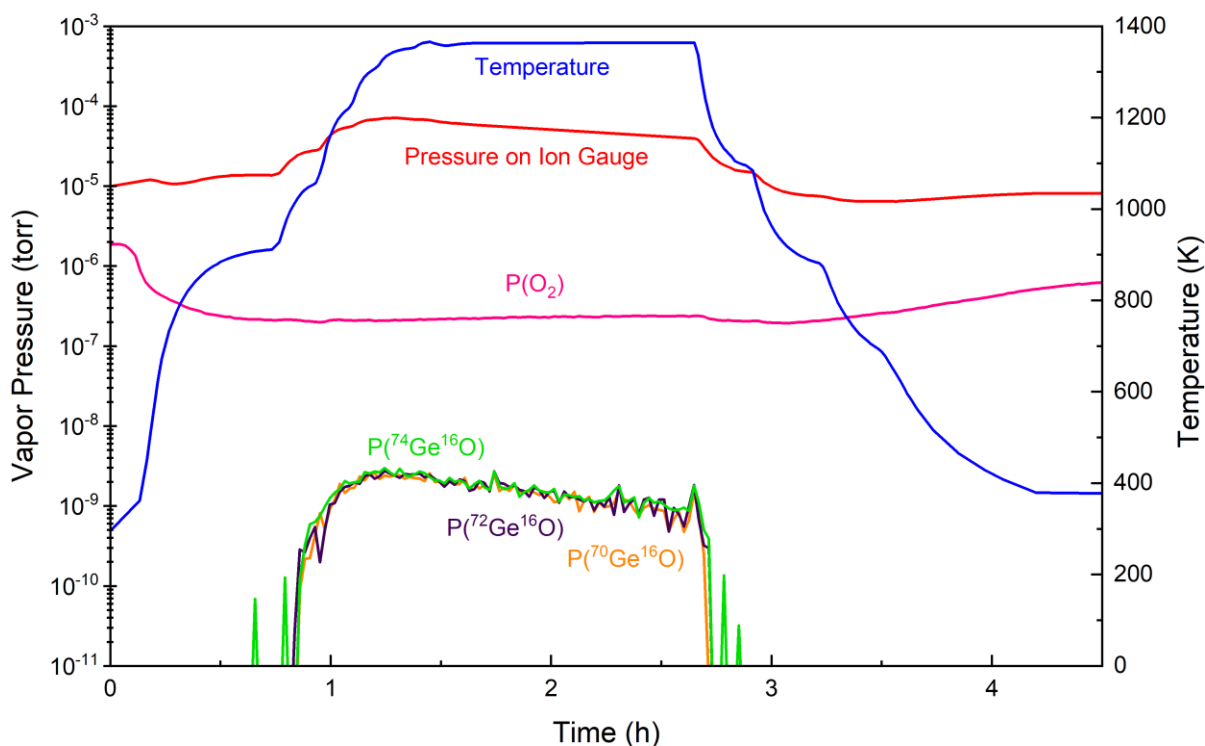


Fig. 6.25 RGA monitoring for $P(\text{O}_2)$ and $P(\text{GeO})$ with total pressure in the second crucible outgassing

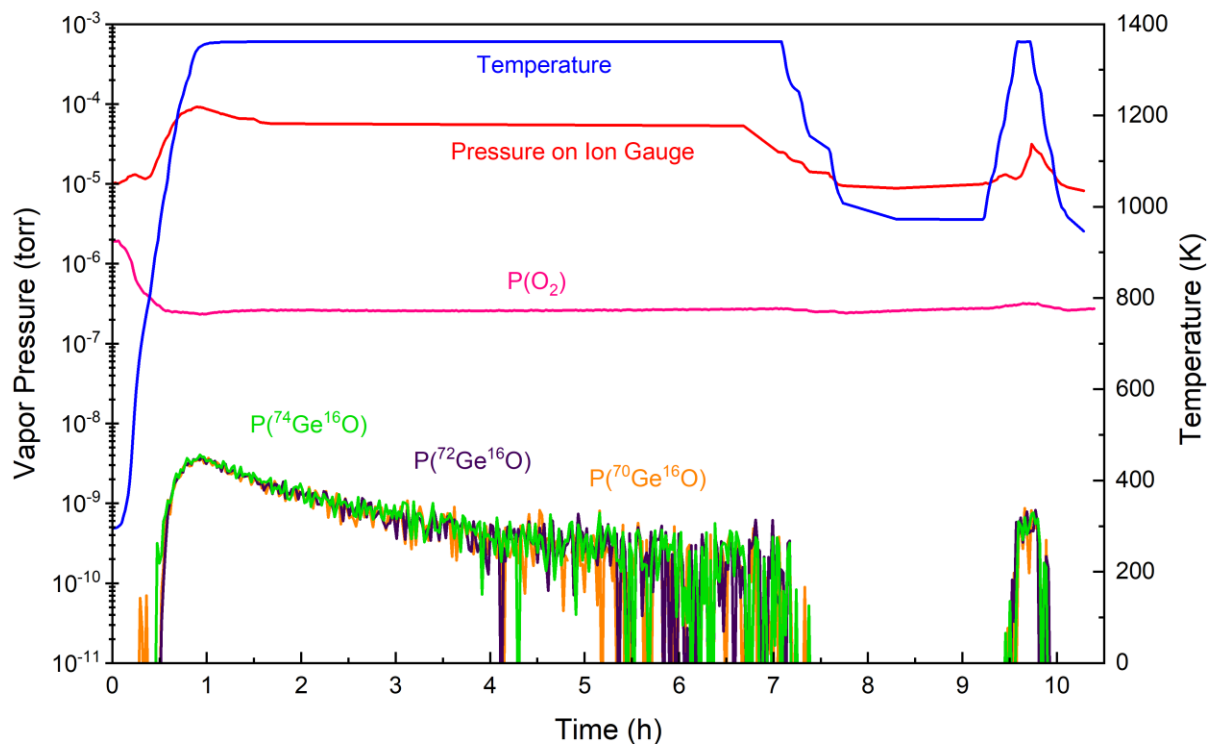


Fig. 6.26 RGA monitoring for $P(O_2)$ and $P(GeO)$ with total pressure in the third and fourth crucible outgassing

As shown Fig 6.25 and Fig 6.26, the RGA signals of mass number of 86, 88, and 90 were also measured during the second, third and fourth crucible outgassing, despite of the absence of Ga sample with high Ge. Interestingly, the signals disappeared once in the end of third crucible outgassing near 1000 K, and then reappeared during the temperature increase and decrease for the fourth crucible outgassing. The source of signal for mass number of 86, 88 and 90 in the crucible outgassing can be electrical background noise of RGA at high temperature, or organic compounds evaporated at high temperature. The mass number of 90 is also equivalent with toluene (C_7H_8). The portion of toluene in mass number 90 is only $\sim 2\%$, while the mass number of 91 for toluene occupies $\sim 40\%$. Since the RGA signal shows the average of spectra measured near the target mass number and near the detection limit, the tail of mass number of 91 signal spectra can overlap with the mass number of 90, so the signal measured for 90 in the crucible outgassing can be toluene

rather than GeO. The mass numbers of 86 and 88 can also be CH_2Cl_2 . Considering the absence of Ge source during the crucible outgassing, the signals for the mass number of 86, 88, and 90 can be from the organic compounds (C-H compounds) activated by temperature increase or background electrical noise, during temperature ramp and at high temperature.

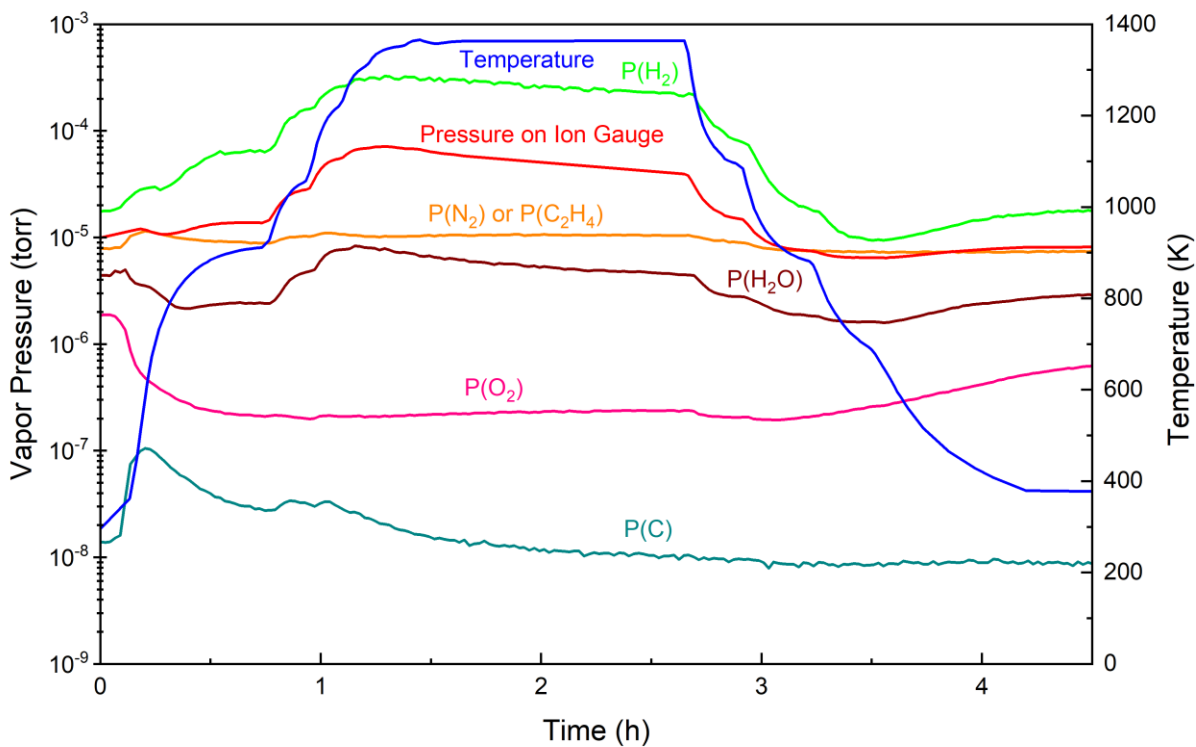


Fig. 6.27 Major gases measured in the RGA during the second crucible outgassing

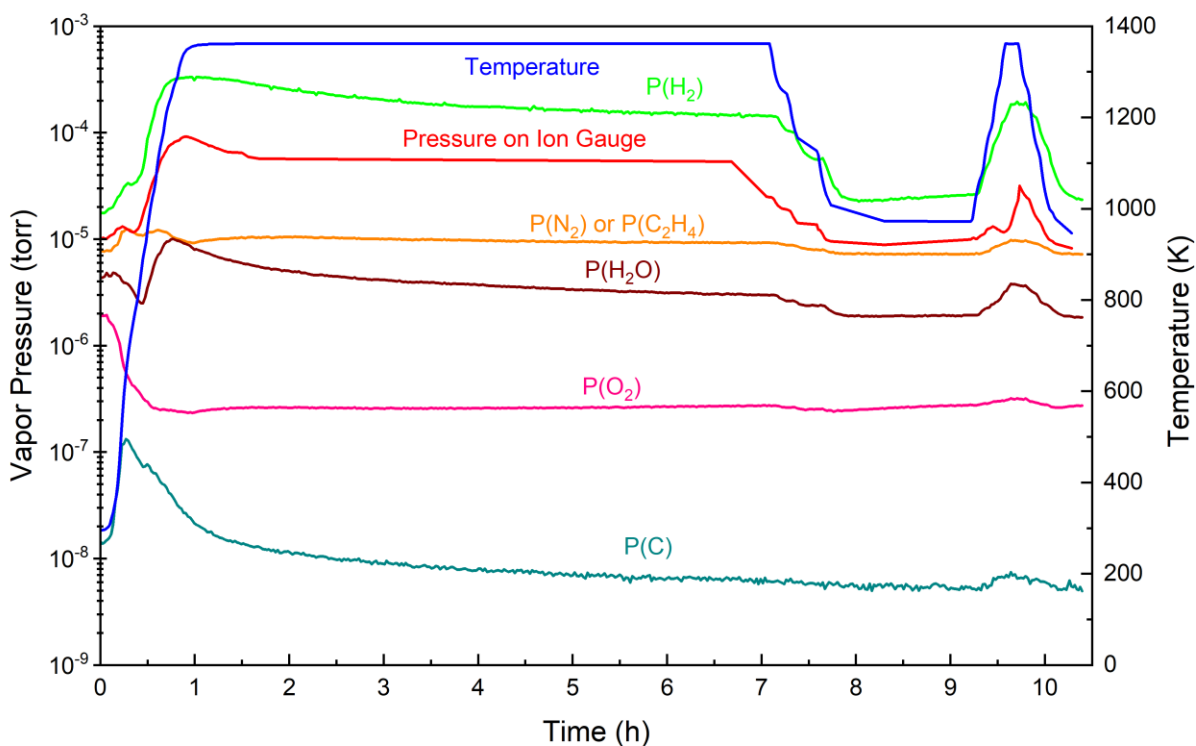


Fig. 6.28 Major gases measured in the RGA during the third and fourth crucible outgassing

However, the signal amplitudes of the mass number of 86, 88 and 90 during crucible outgassing were $\sim 50\%$ smaller than that during distillation of 7N Ga. This is clearer when the signal of mass number 90 in the distillation of 7N Ga is directly compared to that in the crucible outgassing, as shown in Fig 6.29, portion indicated in the only distillation. The signal of mass number 90 in the distillation of Ga shows an obvious difference in amplitude in the region of 30 min \sim 4 h from that in the third crucible outgassing. Between the 3rd crucible outgassing and distillation experiment, the chamber was exposed to 6N grade Ar for venting, but no Ar molecules or compounds does not share the mass numbers of 86, 88 and 90. The only changed parameters that contributed to the signal difference of crucible outgassing and distillation of 7N Ga and related to the mass number of 86, 88 and 90 should be the occurrence of GeO. Therefore, the signal difference possibly shows that GeO was produced and detected in the RGA in the beginning of distillation.

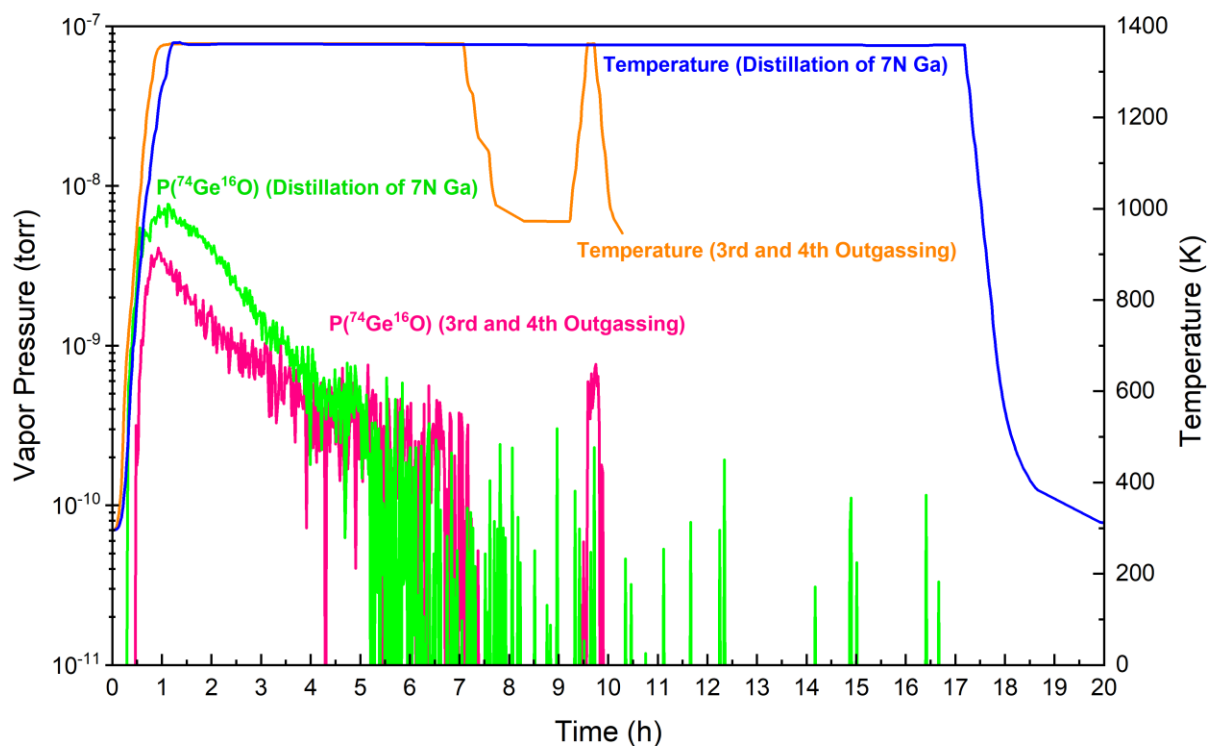
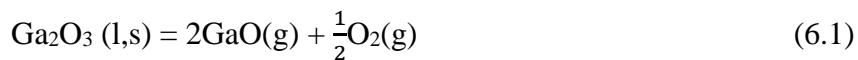


Fig. 6.29 RGA monitoring for $P(O_2)$ and $P(GeO)$ in the third and fourth crucible outgassing

The radically decreased $P(O_2)$ in the distillation of 7N Ga can support the occurrence of GeO. As mentioned earlier, $P(O_2)$ showed a different tendency from other major gases as well as total pressure. Considering the decreased $P(O_2)$ in both second and third crucible outgassing by one order, oxygen was removed more by heating the cell than the activated oxygen molecules due to thermal increase resulting in pressure increase. Although H_2O is the evaporating species by cell heating, $P(H_2O)$ followed the total pressure behavior probably due to large hydrogen bonding energy of H_2O . Large decreases of $P(O_2)$ by cell heating also found only in the cell outgassing supported the probability of oxygen evaporation during heating. However, a far larger decrease in $P(O_2)$ of 100 times than crucible and cell outgassing was found during the distillation of Ga. This is possibly due to Ga oxidation or dissolved oxygen in Ga. Also, this is possibly due to Ge active oxidation in GeO from the beginning to 4 h, considering the minimum of $P(O_2)$ at the maximum

of signals for the mass numbers of 86, 88 and 90. In addition, any Ga oxide that formed would easily dissociate to Ga and oxygen again following the reaction of (6.1), (6.2) and (6.3) [57].



Therefore, oxygen produced near the Ga surface or in the bulk Ga melt from the dissociation of Ga oxide should contribute to increased $P(\text{O}_2)$ during the distillation. However, the $P(\text{O}_2)$ was rather decreased in the beginning of distillation. Therefore, Ge could pick up the oxygen dissociated from the Ga oxide, becoming oxidized and evaporated as GeO until the $P(\text{O}_2)$ increased again.

In major gaseous element measurement by RGA, the $P(\text{N}_2)$ decrease in the beginning of distillation of 7N Ga was distinct from the crucible outgassing and could imply that N_2O or NO_2 was involved in the GeO formation. The mass number of 28 for $P(\text{N}_2)$ also can be applied to the $P(\text{C}_2\text{H}_4)$. In this case, $P(\text{C}_2\text{H}_4)$ for the mass number of 28 could decrease due to the formation of $\text{Ga}(\text{C}_2\text{H}_4)$ compounds. The RGA signal of $P(\text{C})$ for the mass number of 12 decreased more after 10 h in the distillation of Ga than during crucible outgassing. This is possibly due to further evaporation of organic compounds at high temperature for a long time. Or, carbon is possibly dissolved in Ga, resulting in lowering $P(\text{C})$.

In conclusion, the measured RGA signals of mass numbers of 86, 88 and 90 corresponding to the P(GeO) during distillation of 7N Ga were possibly detected and included the signals from gaseous GeO. During the distillation of 7N Ga, the RGA signal of P(O₂) continually decreased and stabilized at a far lower value than during the crucible outgassing, thus supporting the Ge active oxidation and Ga oxidation.

6.5.4 Ga Evaporation Analysis

The Ga loss by distillation was 0.2 g. The cleaned PTFE bottle was weighed to 192.1 g. The weight of the crucible before outgassing was 5.3 g. The PTFE bottle with crucible and distilled Ga extracted after distillation weighed 222.2 g. Thus, the weight of distilled Ga was 24.8 g. Compared to the initial Ga weight of 25 g, 0.2 g was lost.

Earlier calculation suggested the 25 g Ga initially in the PBN crucible would lose 6.4 g during 16 h distillation. However, the actual Ga loss of 0.2 g in the distillation experiment was significantly lower than the calculated amount. This does not agree with the Ga loss of 25 g found in MBE distillation and growth which was close to the calculation results predicted by molecular evaporation theory. The possible reasons of the smaller Ga loss than expected will be explained in the following.

One possible reason of less Ga loss is higher oxygen pressure in the Materials Distillation Chamber. The higher P(O₂) of 3×10^{-6} torr in the Chamber than P(O₂) of the MBE system of 10^{-12} torr could contribute to form Ga oxide on the surface by equation (6.1). The available free energy of

formation of Ga_2O_3 is $\Delta G = -173,670 + 51.56T$ (cal/mol). At the conditions of $P(\text{O}_2)$ of 3×10^{-6} torr and 1360 K, Ga_2O_3 is thermodynamically possible to be formed. Lee, Ahn and Oh [58] found less Ga loss than expected in their vacuum refining of Ga and suggested the Ga oxide layer on the surface could cause the lesser loss of Ga. As observed in the RGA monitoring of Fig 6.23 in the distillation of 7N Ga, a higher drop of $P(\text{O}_2)$ was found compared with crucible-only outgassing. As discussed earlier, this is further evidence of Ga oxidation. In addition, dissolved oxygen in Ga of 300 ppb was found in the GDMS analysis, as listed in Table 6.2. Therefore, an oxygen layer possibly formed on Ga surface in the Materials Distillation Chamber experiment, thus causing the less Ga loss, unlike MBE distillation and growth under almost perfect vacuum.

Another possible reason is that Ga vapor pressure did not reach equilibrium vapor pressure, thus resulting in less Ga loss corresponding to the smaller Ga vapor pressure. In fact, such high vapor pressure corresponding to the equilibrium vapor pressure of Ga at 1360 K of 1.92×10^{-2} torr was not measured in the RGA, or ion gauge. One factor decreasing the vapor pressure of an evaporating species is the effective pressure of other species present in the chamber [10]. As measured by the ion gauge, the total pressure of the chamber was $\sim 10^{-5}$ torr at room temperature before cell heating, unlike the MBE system with almost perfect vacuum level. Therefore, the other gases present in the chamber could disturb the Ga evaporation. The evaporation rate with the consideration of the effective pressure is calculated by deduction of the effective pressure from the equilibrium vapor pressure of the existing surface in Langmuir equation (2.1). However, the Ga equilibrium vapor pressure is three orders higher than the effective pressure of other gases. Consequently, the disturbing effect of the other gaseous species on the evaporating Ga is negligible.

The other factor decreasing the vapor pressure of evaporating species is the pressure drop because the evaporating species takes kinetic energy to move with a certain velocity. Safarian and Engh [59] suggested this concept by comparing the evaporating species getting the kinetic energy to a moving piston in a cylinder. First, the vapor pressure of the system on the surface reached the equilibrium pressure. Then, the overall pressure dropped to move the piston with a certain velocity due to the evaporating gases from the surface. Also, Safarian and Engh analyzed that the pressure drop was bigger as the effective pressure of other gases disturbing the evaporating species was larger. Since the effective pressure (background pressure) of the Materials Distillation Chamber was larger than that of the MBE, the pressure drop due to the evaporating species was larger in the distillation of 7N Ga in the Materials Distillation Chamber than the MBE. Therefore, the significantly smaller Ga loss of 0.2 g was found compared to the calculation of 6.4 g, unlike Ga loss in the MBE distillation and growth was close to the calculated amount.

The other reason is the mean free path of Ga in the distillation experiment. The mean free path λ is defined by [52]

$$\lambda = \frac{kT}{\sqrt{2}\pi d^2 P} \quad (6.4)$$

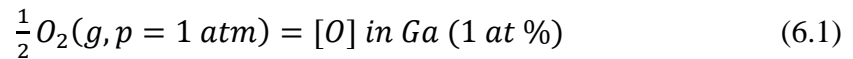
where k is boltzmann constant, d is atomic radius and P is the vapor pressure. At 1360 K, the mean free path of Ga at its saturation vapor pressure is ~ 1.18 cm. The depth from the top of the crucible to the liquid Ga surface was ~ 3.5 cm in the distillation experiment. This implies most Ga atoms did not escape from the crucible due to the smaller mean free path than the crucible depth. On the while, the depth from the top of the crucible to the Ga surface was ~ 1.08 cm as shown in Fig 2.1 in the MBE distillation and growth because 100 g Ga was used. The crucible depth in the MBE distillation and growth was shorter than the mean free path of 1.18 cm at 1360 K or 56.5 cm at

1160 K. Therefore, higher Ga loss of 25 g was possible in the MBE distillation and growth, whereas only 0.2 g Ga loss was found in the Materials Distillation Chamber experiment.

6.5.5 Calculations of Solubility of Oxygen in Ga

The GDMS results showed the concentration of oxygen dissolved in 7N Ga (Alcan) increased from 10 ppb to 300 ppb in the recovered Ga. This implies oxygen in background dissolved into the Ga during the 16 h distillation at 1360 K. The decreased $P(O_2)$ during distillation measured in RGA in the previous section also supports the dissolved oxygen in Ga. The solubility of oxygen that can dissolve in Ga in the equilibrium state can be calculated from the given Gibbs free energy of oxygen in Ga at 1 at % Oxygen atom.

The reaction of dissolved oxygen in Ga is defined by



The Gibbs energy of oxygen in liquid Ga at 1 at % O is given by (6.2) [60],

$$\Delta G_{1 \text{ at \% in Ga}}^0 = -215,800 + 24.0 T \left(\frac{J}{\text{mol}} \right) \quad (T = 1048 - 1473 \text{ K}) \quad (6.2)$$

The Gibbs energy of oxygen in liquid Ga at 1 at % O can be represented by equilibrium constant as shown (6.3)

$$\Delta G_{1 \text{ at \% in Ga}}^0 = -RT \ln K_{1 \text{ at \%}} = -RT \ln \frac{[\text{at \% O}] \text{ in Ga}}{P(O_2)^{\frac{1}{2}}} \quad (6.3)$$

The relation of at % and wt % is given by (6.4)

$$[O] \text{ in Ga (1 at \%)} = [O] \text{ in Ga (1 wt \%)} \quad (6.4)$$

To convert the unit at % to wt %, the Gibbs free energy of (6.4) is considered as shown (6.5).

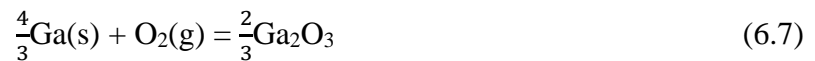
$$\Delta G_{(4)}^0 = 8.3144 \times 10^{-3} T \ln \frac{0.042159}{0.01} = 12.0 T \text{ (J)} \quad (5)$$

The Gibbs free energy in wt % is the sum of (6.2) and (6.5) and given by (6.6)

$$\Delta G_{1 \text{ wt \% in Ga}}^0 = -215,800 + 36.0 T \left(\frac{\text{J}}{\text{mol}} \right) \quad (6.6)$$

Using the equation (6.6), the oxygen solubility in liquid Ga can be derived as a function of $P(\text{O}_2)$ and temperature.

Oxygen can be dissolved in Ga as well as react with Ga forming Ga_2O_3 . Above the dissociation $P(\text{O}_2)$ of the formation of Ga_2O_3 , oxygen reacts with Ga forming a Ga oxide layer, Ga_2O_3 and below the dissociation $P(\text{O}_2)$, oxygen is dissolved in Ga [61]. The free energy of formation of Ga_2O_3 is $\Delta G_T^0 = -173670 + 51.56 T$ (cal/mole) for the reaction of



The dissociation $P(\text{O}_2)$ at 1360 K for the reaction of (6.7) is 2.3×10^{-17} atm. Since oxygen reacts with Ga and forms Ga oxide rather than dissolving in Ga above the dissociation $P(\text{O}_2)$, the maximum equilibrium concentration of oxygen dissolved in Ga may be calculated at the

dissociation $P(O_2)$ of 2.3×10^{-17} atm instead of the starting $P(O_2)$ of 4×10^{-8} atm (3×10^{-6} torr) in the Materials Distillation Chamber.

The equilibrium concentration of oxygen in liquid Ga at the corresponding $P(O_2)$ were derived as shown in Fig 6.30. In the conditions of distillation of 7N Ga, which were 1360 K and the starting $P(O_2)$ of 4×10^{-8} atm, the $P(O_2)$ already reached the equilibrium (dissociation) pressure of Ga_2O_3 formation. Since Ga_2O_3 was thermodynamically stable in the distillation of 7N Ga, Ga oxide layers could form possibly with the equilibrium concentration of oxygen of 123 ppm corresponding to the equilibrium $P(O_2)$ of Ga_2O_3 formation of 2.3×10^{-17} atm at 1360 K in Fig 6.30. This is still high enough compared to the GDMS result of 300 ppb. Considering that actual $P(O_2)$ near liquid Ga surface where oxidation occurred could lower than the $P(O_2)$ measured by RGA and the Ga oxidation was kinetically slow, the equilibrium for 123 ppm oxygen concentration in Ga possibly did not achieved during the 16 h distillation. Thus, the oxygen concentration in Ga could increase in further distillation.

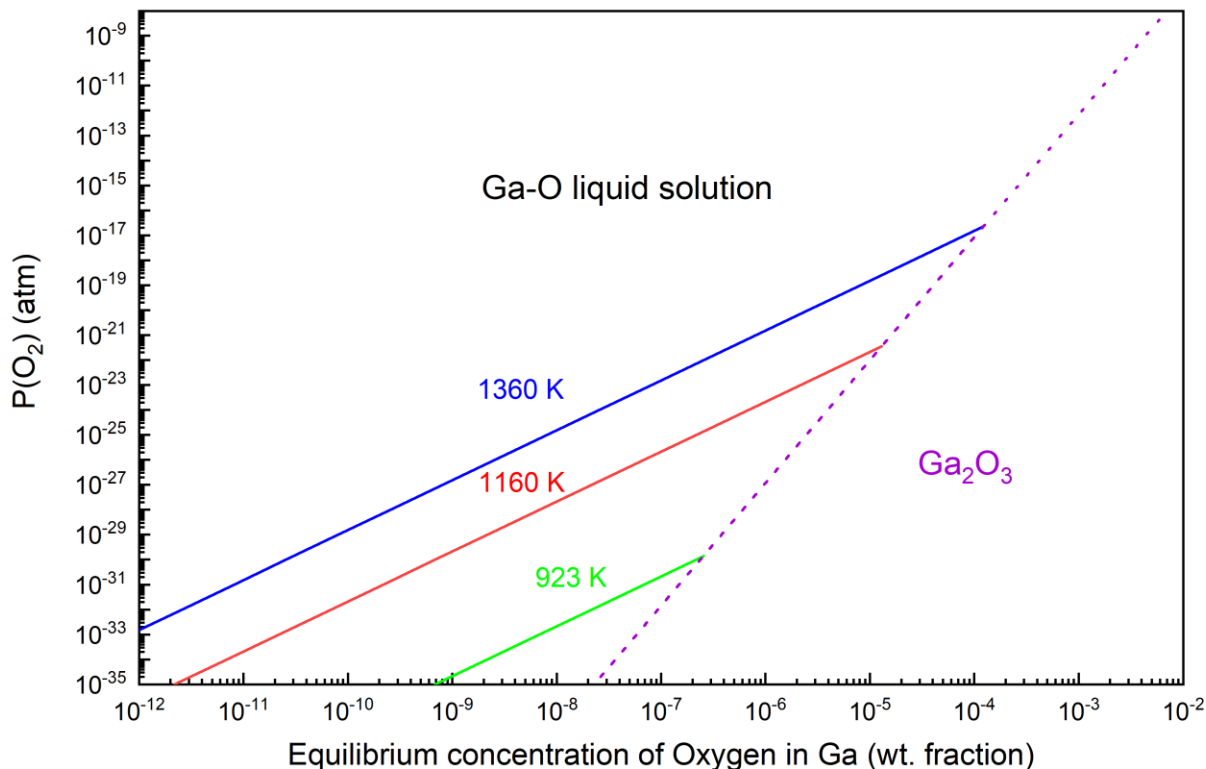


Fig. 6.30 The solubility of oxygen in liquid Ga in equilibrium and stable phase depending on $P(\text{O}_2)$ at 1360 K, 1160 K and 923 K

The MBE background $P(\text{O}_2)$ of $\sim 10^{-15}$ atm was higher than the equilibrium $P(\text{O}_2)$ for the Ga₂O₃ formation in all three temperature ranges of 1360 K, 1160 K and 923 K. Consequently, the oxygen solubility in Ga at 1360 K was 123 ppm corresponding to the dissociation $P(\text{O}_2)$ for the Ga₂O₃ formation at 1360 K of 2.3×10^{-17} atm. The oxygen solubility in Ga at 1160 K was 13 ppm corresponding to the dissociation $P(\text{O}_2)$ for the Ga₂O₃ formation at 1160 K of 3.5×10^{-22} atm. The oxygen solubility in Ga at 923 K was 250 ppm corresponding to the dissociation $P(\text{O}_2)$ for the Ga₂O₃ formation at 923 K of 1.4×10^{-30} atm.

The equilibrium oxygen concentrations in Ga at the three temperatures of distillation, growth and idling were relatively high to other impurity concentrations in 7N and 8N Ga (Appendix B).

Particularly, Ga was stored at 923 K over a year in the second growth campaign, hence the oxygen dissolution could reach the equilibrium. A significant amount of oxygen, corresponding to 250 ppb (compared to the initial concentrations of impurities in ultra-pure Ga) could be dissolved in Ga and affect the purity of grown GaAs thus resulting low mobility in the case Ga was used for growth without distillation. The extremely low mobility found in the beginning of second growth campaign can be explained due to the dissolved oxygen during storing at idling temperature.

7. CONCLUSIONS

Prior results established that the mobility in 2DEG confined in GaAs/AlGaAs depends on source Ga purity. A significant increase of mobility was found in the in-situ MBE distillation of Ga. Moreover, 8N Ga led to higher mobility of $35 \times 10^6 \text{ cm}^2/\text{Vs}$ compared to the 7N Ga, resulting in the mobility of $20 \times 10^6 \text{ cm}^2/\text{Vs}$.

In order to clarify what specific impurities degrade the mobility, the initial 7N and 8N Ga and the remained 7N and 8N Ga after in-situ MBE distillation and growth were elementally analyzed by ICP-MS. However, the analyzed impurity elements reached the detection limit except for Ge. Although ICP-MS is the state-of-art technique able to measure to sub-ppt concentration levels, cross contamination, spectral interference and matrix effect in the metal analysis in the liquid samples degraded the capability of ICP-MS. The high dissolved Ga to achieve sufficient concentration in the samples caused the matrix effect where Ga is deposited on the ICP-MS components, thus disturbing analyte (impurity elements) cannot reach the mass spectrometer and resulting in low signals. For further lowering the detection limit of ICP-MS, the matrix Ga separation was recommended in the sample preparation steps. Therefore, the methodology to separate Ga from Ge using dextran-resin gel was established through thermodynamic study to attempt the Ga matrix removal in the ICP-MS sample.

Unusually high Ge loss was found in the ICP-MS analysis of the initial and the remained Ga. This did not agree with the calculated Ge loss of $\sim 39 \text{ ng}$ predicted from Langmuir-Knudsen by Ge atomic evaporation. Molecular distillation theory was analyzed to investigate the reason for high

Ge loss. First, Ga evaporation was analyzed and then impurity evaporation was analyzed. The actual Ga loss of ~25 g was significantly smaller than the calculated potential Ga loss of ~67 g from the Langmuir equation during in-situ MBE distillation and growth. The difference was mostly explained by considering Ga evaporation from the MBE crucible with a receding liquid surface, considering collision and condensation effects, which gave ~ 28 g matching closely with the actual Ga loss. When collision and condensation effects are added to Ge evaporation, the calculated Ge loss further decreased. Therefore, some additional explanation was requested to explain high loss of Ge during the distillation and growth.

A Ge active oxidation hypothesis that Ge was evaporated in the form of gaseous Ge oxide of GeO(g) was proposed to explain the high Ge loss. The vapor species diagram of equilibrium $\text{P(GeO)-P(O}_2\text{)}$ at a dilute Ge in Ga about ~ 1 ppm concentration was developed. The vapor species diagram for 1 ppm dilute Ge in Ga system showed Ge could be actively oxidized at the extremely low $\text{P(O}_2\text{)}$ of MBE.

In order to prove Ge active oxidation, a molecular distillation experiment was performed in a specially constructed high vacuum chamber. A 7N Ga with unusually high Ge concentration was distilled for 16 h at 1360 K under the starting $\text{P(O}_2\text{)}$ of 3×10^{-6} torr and the total pressure of 10^{-5} torr. The distilled Ga was analyzed by GDMS and compared with the initial 7N Ga GDMS analysis. Germanium was found to decrease from 440 ppb to below the detection limit of 10 ppb. This confirmed Ge active oxidation. RGA spectra comparison of the distillation experiment and of crucible outgassing also supported Ge active oxidation. A smaller Ga loss of ~ 0.2 g than the expected Ga loss of ~ 6.4 g was found. This is possibly due to Ga oxide formation on Ga melt

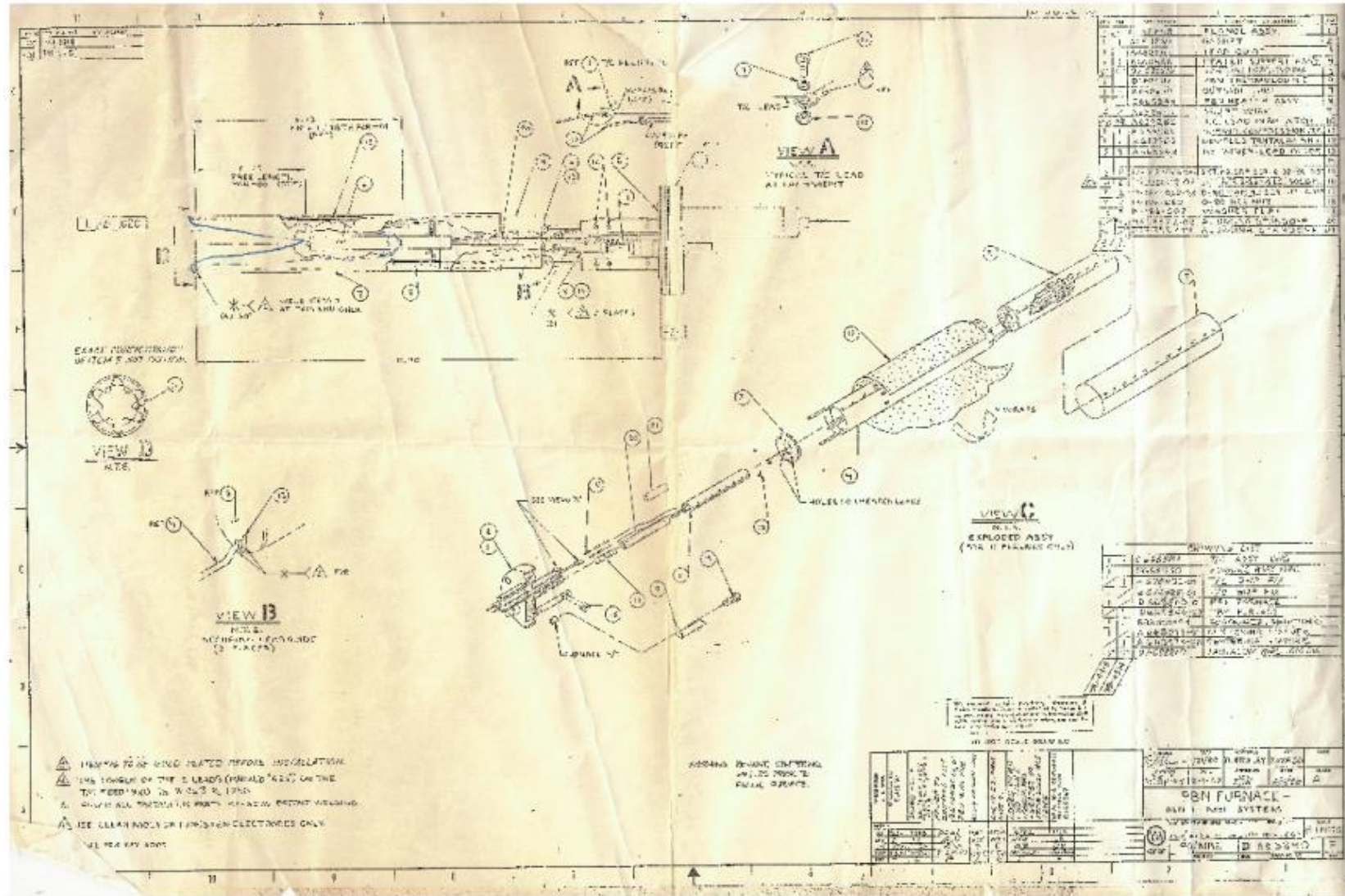
surface disturbing further Ga evaporation. Other possibilities include a lower Ga vapor pressure than equilibrium and a smaller mean free path than crucible depth, thus causing Ga to be stuck in the crucible. Also, an increased oxygen concentration in Ga was found in the GDMS analysis, possibly due to background oxygen dissolution in Ga during distillation.

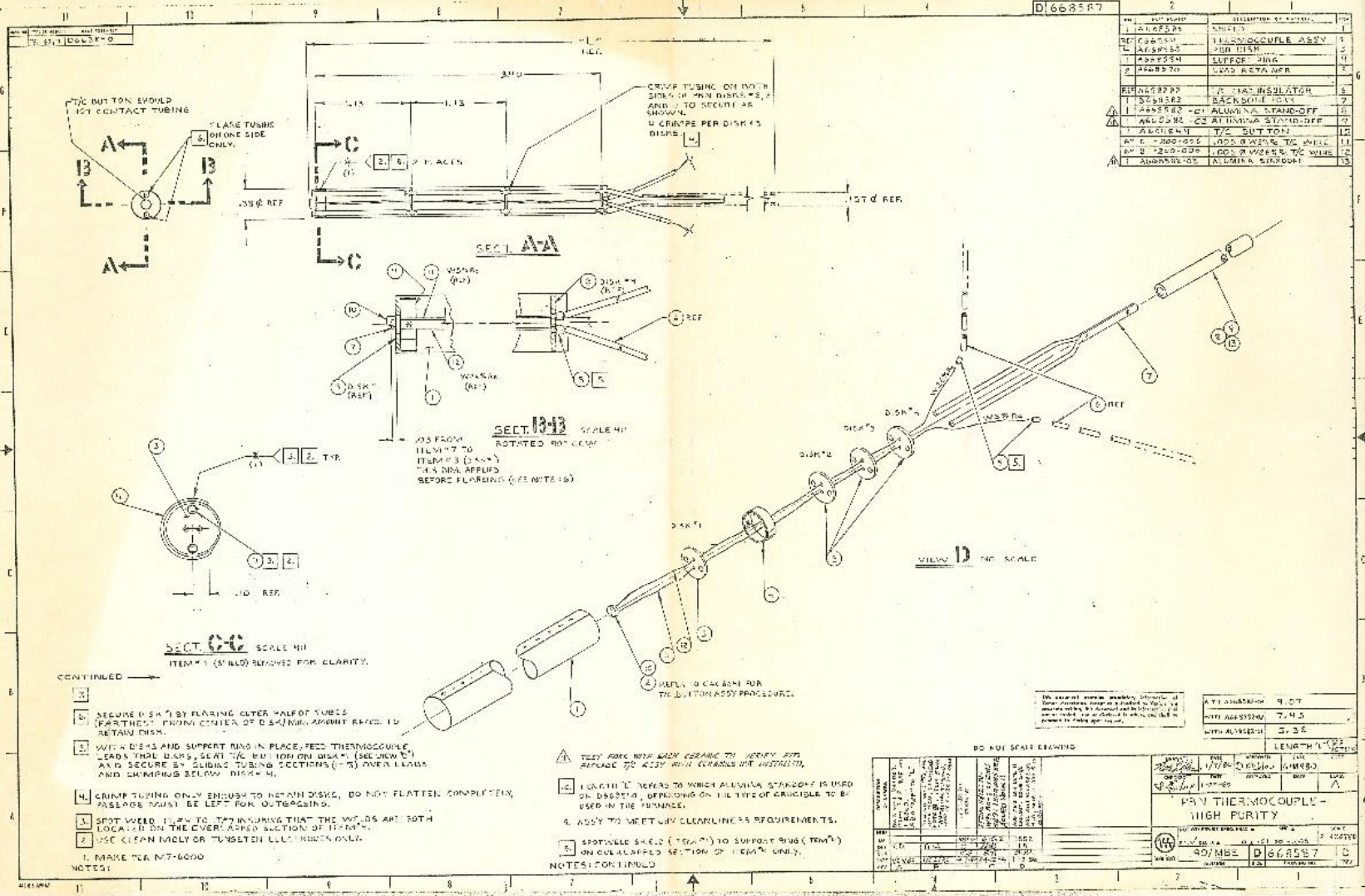
Germanium loss through Ge active oxidation implies oxygen helped in impurity removal. The oxygen-assisted impurity removal in distillation also may be applicable to other impurities with high vapor pressure gaseous oxides, but low vapor pressure itself such as Al, Si and Sn. Indium also has a gaseous oxide of In_2O . However, In itself has a high vapor pressure. Consequently, there is no reason to remove In by intentionally introducing oxygen.

Germanium active oxidation implies Ge can be introduced to GaAs during growth. This indicates impurity elements with high vapor pressure gaseous oxide can be evaporated and deposited in GaAs though the impurity elements has lower vapor pressure itself. As discussed in Chapter 5, high enough $P(\text{GeO})$ was shown in dilute Ge vapor species diagram for the growth temperature of 1160 K even at the MBE $P(\text{O}_2)$ condition. Rather, slightly higher equilibrium $P(\text{GeO})$ was found in the lower temperature range in the direct active oxidation region. Although the equilibrium $P(\text{GeO})$ decreases as Ge concentration decrease for the fixed $P(\text{O}_2)$, the formation of GeO is thermodynamically possible no matter how Ge concentration significantly decrease as far as minute Ge is present in the system. This may be applied to Si or other impurity elements with similar gaseous oxide as Ge. Therefore, the sufficient distillation should be preceded ahead of growth to remove impurities in active oxidation.

The distillation analysis showed higher vapor pressure elements than solvent Ga are more effectively distilled, suggesting the distillation of materials with impurities of high vapor pressure has an advantage on purification of Ga. However, the distillation of materials only with impurities of lower vapor pressure than solvent Ga rather increases the impurity concentration in the residual Ga due to high evaporation rate of Ga. Therefore, the benefit of distillation to purify Ga and evaporating Ga vapor for growth depends on the composition of impurities, the relative vapor pressures of impurities to Ga and the initial concentration of each impurity.

APPENDIX A. SOURCE CELL DRAWING





APPENDIX B. GDMS ANALYSIS RESULTS

1. 7N Ga (Alcan, Lot No. AEM 7/605)

	GDMS ANALYTICAL REPORT	Evans Analytical Group 103 Commerce Blvd Liverpool, New York 13088	Telephone (315) 431-9900 Fax: (315) 431-9800 Email info.ny@eaglabs.com www.eaglabs.com
---	----------------------------------	--	---

Customer:	Purdue University 1205 West State Street, West Lafayette, IN 47907-2057 USA	P.O.#	4500003214
Date:	30-Oct-13	Job #	S0DKG886
Customer ID:	Ga 20131011 Ga Initial Material	Sample ID:	S131022048

(Rev: 2013-10-30 12:02:07)

Element	Concentration [ppb wt]	Element	Concentration [ppb wt]
Li	< 0.1	Pd	< 0.5
Be	< 0.1	Ag	< 50
B	< 0.1	Cd	< 1
C	< 1	In	< 0.1
N	2	Sn	< 0.5
O	10	Sb	< 0.5
F	< 10	Te	< 0.1
Na	< 0.1	I	< 0.1
Mg	< 0.1	Cs	< 0.1
Al	< 0.1	Ba	< 1
Si	< 0.5	La	< 1
P	< 0.1	Ce	< 100
S	0.6	Pr	< 1
Cl	0.8	Nd	< 0.5
K	< 5	Sm	< 5
Ca	< 0.5	Eu	< 0.5
Sc	< 0.1	Gd	< 0.5
Ti	< 0.1	Tb	< 0.1
V	< 0.1	Dy	< 0.1
Cr	< 0.1	Ho	< 0.1
Mn	< 0.1	Er	< 0.1
Fe	< 0.1	Tm	< 0.1
Co	< 0.1	Yb	< 0.1
Ni	< 0.1	Lu	< 0.1
Cu	< 0.5	Hf	< 0.1
Zn	< 0.5	Ta	Source
Ga	Matrix	W	< 5
Ge	440	Re	< 0.1
As	< 0.5	Os	< 0.1
Se	< 1	Ir	< 0.1
Br	< 5	Pt	< 0.1
Rb	< 5	Au	< 10
Sr	< 0.1	Hg	< 0.5
Y	< 0.1	Tl	< 0.5
Zr	< 0.1	Pb	< 0.5
Nb	< 0.1	Bi	< 0.5
Mo	< 0.1	Th	< 0.1
Ru	< 0.1	U	< 0.1
Rh	< 0.1		



Page 1 of 1 - GDMS
Analyzed according to WI F rev. 12/08/12
Reviewed by _____

C.GAGNON (Analyst)



Precision and bias typical of GDMS measurements are discussed under ASTM F1503.
This shall not be reproduced except in full without written approval of the laboratory.

2. Recovered Ga from distillation of 7N Ga



Eurofins
Materials Science

GDMS
Analytical Report

103 Commerce Blvd. Liverpool, NY 13086
T (315) 431-6900 F (315) 431-6900
info.ny@eag.com www.eag.com

Customer: **Purdue University**

P.O.#

Date: 14-Jan-19

Job #

SOJZM115

Customer ID: Ga

Sample ID:

S190109059

BRK-01-2019-14

[Rev: 2019-01-15 16:47:22]

Element	Concentration [ppb wt]	Element	Concentration [ppb wt]
Li	< 0.1	Pd	< 0.5
Be	< 0.1	Ag	< 50
B	< 0.1	Cd	< 1
C	-	In	10
N	-	Sn	< 0.5
O	300	Sb	< 0.5
F	< 10	Te	< 0.1
Na	1.1	I	< 0.1
Mg	< 0.1	Cs	< 0.1
Al	0.3	Ba	< 1
Si	2	La	< 1
P	< 0.1	Ce	< 100
S	< 0.5	Pr	< 1
Cl	3	Nd	< 0.5
K	< 5	Sm	< 5
Ca	< 0.5	Eu	< 0.5
Sc	< 0.1	Gd	< 0.5
Ti	< 0.1	Tb	< 0.1
V	< 0.1	Dy	< 0.1
Cr	< 0.1	Ho	< 0.1
Mn	< 0.1	Er	< 0.1
Fe	0.8	Tm	< 0.1
Co	< 1	Yb	< 0.1
Ni	< 0.1	Lu	< 0.1
Cu	< 0.5	Hf	< 0.1
Zn	2	Ta	Source
Ga	Matrix	W	< 5
Ge	< 10	Re	< 0.1
As	< 0.5	Os	< 0.1
Se	< 0.5	Ir	< 0.1
Br	< 5	Pt	< 0.1
Rb	< 5	Au	< 10
Sr	< 0.1	Hg	< 0.5
Y	< 0.1	Tl	< 0.5
Zr	< 0.1	Pb	< 0.5
Nb	< 0.1	Bi	< 0.5
Mo	< 0.1	Th	< 0.1
Ru	< 0.1	U	< 0.1
Rh	< 0.1		



Page 1 of 1 - GDMS
Analyzed according to W1 F rev. 11/10/17
Reviewed by _____

S.KUSHNIR (Analyst)

Precision and bias typical of GDMS measurements are discussed under ASTM F1063.
This shall not be reproduced except in full without written approval of the laboratory.

2. 8N Ga



Molycorp Rare Metals (Utah), Inc.
 1877 East Harris Lane
 Blanding, Utah 84511 USA
 Tel: 435-678-2734
 Fax: 435-678-3276
 www.molycorp.com

Gallium MBE

CERTIFICATE OF ANALYSIS

Customer : Purdue University
 PO#4500174781

Date : 06-11-2015
 Lot No. : 815040
 RRR Value: 80,000

Element		ppb	Element		ppb
Beryllium	Be	< 0.1	Nickel	Ni	< 0.3
Boron	B	< 0.2	Copper	Cu	< 0.7
Sodium	Na	< 0.2	Zinc	Zn	< 2
Magnesium	Mg	< 0.3	Germanium	Ge	< 10
Aluminium	Al	< 0.2	Arsenic	As	< 0.5
Silicon	Si	< 0.4	Selenium	Se	< 5
Phosphorus	P	< 0.3	Bromine	Br	< 6
Sulphur	S	< 0.4	Strontium	Sr	< 0.2
Chlorine	Cl	< 2	Silver	Ag	< 50
Potassium	K	< 25	Cadmium	Cd	< 4
Calcium	Ca	< 4	Indium	In	< 1
Scandium	Sc	< 0.1	Tin	Sn	< 4
Titanium	Ti	< 0.2	Antimony	Sb	< 0.9
Vanadium	V	< 0.1	Tellurium	Te	< 2
Chromium	Cr	< 0.3	Gold	Au	< 15
Manganese	Mn	< 0.2	Mercury	Hg	< 6
Iron	Fe	1	Thallium	Tl	< 1
Cobalt	Co	< 0.2	Lead	Pb	< 0.4

Analysis performed by Glow Discharge Mass Spectroscopy (GDMS). Figures relate to weight. Values marked as < (less than) are below analytical detection limits and do not necessarily indicate the presence or absence of the element.

The best indicator for overall purity is the Residual Resistivity Ratio (RRR) analysis. The minimum RRR reading for MBE grade Gallium is 75,000.

Prepared by: Jeremy Jex

REFERENCES

- [1] D. C. Tsui and A. C. Gossard, "Resistance standard using quantization of the Hall resistance of GaAs-Al_xGa_{1-x}As heterostructures," *Appl. Phys. Lett.*, vol. 38, no. 7, pp. 550–552, 1981.
- [2] S. Das Sarma, M. Freedman, and C. Nayak, "Topologically protected qubits from a possible non-Abelian fractional quantum Hall state," *Phys. Rev. Lett.*, vol. 94, no. 16, 2005.
- [3] S. Das Sarma and A. Pinczuk, *Perspectives in quantum Hall effects novel quantum liquids in low-dimensional semiconductor structures*. New York: John Wiley & Sons, Inc, 1997.
- [4] E. H. Hwang and S. Das Sarma, "Limit to two-dimensional mobility in modulation-doped GaAs quantum structures: How to achieve a mobility of 100 million," *Phys. Rev. B - Condens. Matter Mater. Phys.*, vol. 77, no. 23, pp. 4–9, 2008.
- [5] M. J. Manfra, "Molecular Beam Epitaxy of Ultra-High-Quality AlGaAs/GaAs Heterostructures: Enabling Physics in Low-Dimensional Electronic Systems," *Annu. Rev. Condens. Matter Phys.*, vol. 5, no. 1, pp. 347–373, 2014.
- [6] G. C. Gardner, S. Fallahi, J. D. Watson, and M. J. Manfra, "Modified MBE hardware and techniques and role of gallium purity for attainment of two dimensional electron gas mobility $>35 \times 10^6 \text{ cm}^2/\text{Vs}$ in AlGaAs/GaAs quantum wells grown by MBE," *J. Cryst. Growth*, vol. 441, pp. 71–77, 2016.
- [7] E. F. Schubert, *Doping in III-V semiconductors*. Cambridge [England]; New York, NY, USA: Cambridge University Press, 1993.
- [8] R. Bautista, "Processing to Obtain High-Purity Gallium," *JOM*, vol. 55, no. 3, pp. 23–26, 2003.
- [9] W. G. Pfann, *Zone melting.*, 2d ed.. New York: Wiley, 1966.
- [10] R. D. Pehlke, *Unit Processes of Extractive Metallurgy*. Elsevier Science Ltd, 1973.
- [11] I. Langmuir, "The vapor pressure of metallic tungsten," *Phys. Rev.*, vol. 2, no. 5, pp. 329–342, 1913.
- [12] R. Speiser and H. L. Johnston, "Vapor Pressures of Inorganic Substances.," *J. Am. Chem. Soc.*, vol. 75, no. 6, p. 1469, 1953.

- [13] P. Clausing, "Über die Strömung sehr verdünnter Gase durch Röhren von beliebiger Länge," *Ann. Phys.*, vol. 404, no. 8, pp. 961–989, 1932.
- [14] M. Hino and T. Azakami, "Thermodynamic Study of Liquid Ag-In and Ag-Ga Alloys With a Knudsen Cell-Mass Spectrometer," *Mater. Trans., JIM*, vol. 30, no. 8, pp. 575–582, 1989.
- [15] J. Wang, Y. J. Liu, L. B. Liu, H. Y. Zhou, and Z. P. Jin, "Thermodynamic assessment of the Au-Ga binary system," *Calphad*, vol. 35, no. 2, 2011.
- [16] A. Kostov, D. Zivkovic, and Z. Zivkovic, "Thermodynamic analysis of binary systems Ge," *Thermochim. Acta*, vol. 338, no. 1–2, pp. 35–43, 1999.
- [17] K. K. Hultgren, Ralph; Orr, Raymond L.; Anderson, Philip D.; Kelley, *Selected values of thermodynamic properties of metals and alloys*. John Wiley and Sons, Inc., 1963.
- [18] D. Zivkovic, D. Manasijevic, and Z. Zivkovic, "Thermodynamic study of Ga-Sn and Ga-Zn systems using quantitative differential thermal analysis," *J. Therm. Anal. Calorim.*, vol. 74, no. 1, pp. 85–96, 2003.
- [19] C. Weaver M, A. Rothwell P, and K. Wood V, "Measuring calcium absorption and utilization in humans," *Curr. Opin. Clin. Nutr. Metab. Care*, vol. 9, no. 5, pp. 568–574, 2006.
- [20] C. Technologies, "Aridus Desolvating Sample Introduction System Operator's Manual," *CETAC Technol.*, 2000.
- [21] M. Berglund and M. E. Wieser, "Isotopic compositions of the elements 2009 (IUPAC Technical Report)," *Pure Appl. Chem.*, vol. 83, no. 2, pp. 397–410, 2011.
- [22] Thomas W. May and Ray H. Wiedmeyer, "A Table of Polyatomic Interferences in ICP-MS," *At. Spectrosc.*, vol. 19, no. 5, pp. 150–155, 1998.
- [23] ThermoFinnigan, "Element2 Operator Manual," 2001.
- [24] H. Xie, X. Nie, and Y. Tang, "Direct Determination of Trace Elements in High Purity Gallium by High Resolution Inductively Coupled Plasma Mass Spectrometry," *Chinese J. Anal. Chem.*, vol. 34, no. 11, pp. 1570–1574, 2006.
- [25] C. Agatemor and D. Beauchemin, "Matrix effects in inductively coupled plasma mass spectrometry: A review," *Anal. Chim. Acta*, vol. 706, no. 1, pp. 66–83, 2011.
- [26] S. J. Kumar, N. N. Meeravali, and J. Arunachalam, "Determination of trace impurities in high purity gallium by inductively coupled plasma mass spectrometry and cross validation

- of results by transverse heated graphite furnace atomic absorption spectrometry,” *Anal. Chim. Acta*, vol. 371, no. 2, pp. 305–316, 1998.
- [27] S. H. Tan and G. Horlick, “Matrix-effect observations in inductively coupled plasma mass spectrometry,” *J. Anal. At. Spectrom.*, vol. 2, no. 8, pp. 745–763, 1987.
- [28] R. Rafaeloff, “Separation of gallium from Group III elements, germanium, copper, arsenic, and iron,” *Anal. Chem.*, vol. 43, no. 2, pp. 272–274, 1971.
- [29] J. Fitzsimmons and L. Mausner, “Evaluation of Materials for the Separation of Germanium from Gallium, Zinc and Cobalt,” *J. Chem. Chem. Eng.*, vol. 9, 2015.
- [30] J. M. Fitzsimmons and L. Mausner, “Development of a production scale purification of Ge-68 from irradiated gallium metal,” *Radiochim. Acta*, vol. 103, no. 2, pp. 117–123, 2015.
- [31] A. Harada, T. Tarutani, and K. Yoshimura, “Spectrophotometric determination of germanium in rocks after selective adsorption on sephadex gel,” *Anal. Chim. Acta*, vol. 209, no. C, pp. 333–338, 1988.
- [32] C. F. Baes, *The hydrolysis of cations*. New York: Wiley, 1976.
- [33] P. L. Brown, *Hydrolysis of metal ions*. Wiley-VCH Verlag, 2016.
- [34] S. A. Wood and I. M. Samson, “The aqueous geochemistry of gallium, germanium, indium and scandium,” *Ore Geol. Rev.*, vol. 28, no. 1, pp. 57–102, 2006.
- [35] A. W. Searcy and R. D. Freeman, “Measurement of the Molecular Weights of Vapors at High Temperature. II. The Vapor Pressure of Germanium and the Molecular Weight of Germanium Vapor,” *J. Chem. Phys.*, vol. 23, no. 1, pp. 88–90, 1955.
- [36] K. Min, D. Johnson, and K. Trumble, “Materials Processing Fundamentals 2017,” pp. 73–83, 2017.
- [37] E. T. Turkdogan, P. Grieveson, and L. S. Darken, “Enhancement of diffusion-limited rates of vaporization of metals,” *J. Phys. Chem.*, vol. 67, no. 8, pp. 1647–1654, 1963.
- [38] C. Wagner, “Passivity during the oxidation of silicon at elevated temperatures,” *J. Appl. Phys.*, vol. 29, no. 9, pp. 1295–1297, 1958.
- [39] C. Wagner, “Passivity and inhibition during the oxidation of metals at elevated temperatures,” *Corros. Sci.*, vol. 5, no. 11, pp. 751–764, 1965.
- [40] E. A. Gulbransen, K. F. Andrew, and F. A. Brassart, “Oxidation of Silicon at High Temperatures and Low Pressure under Flow Conditions and the Vapor Pressure of Silicon,” *J. Electrochem. Soc.*, vol. 113, no. 8, pp. 834–837, 1966.

- [41] O. (Oswald) Kubaschewski, *Metallurgical thermochemistry*, 5th ed., R. Oxford ; New York: Pergamon Press, 1979.
- [42] E. T. Turkdogan, *Physical chemistry of high temperature technology*. New York: Academic Press, 1980.
- [43] W. L. Jolly and W. M. Latimer, "The Equilibrium $\text{Ge(s)} + \text{GeO}_2\text{(s)} = 2\text{GeO(g)}$. The Heat of Formation of Germanic Oxide," *J. Am. Chem. Soc.*, vol. 74, no. 22, pp. 5757–5758, 1952.
- [44] P. Flubacher, A. J. Leadbetter, and J. A. Morrison, "The heat capacity of pure silicon and germanium and properties of their vibrational frequency spectra," *Philos. Mag.*, vol. 4, no. 39, pp. 273–294, 1959.
- [45] U. L. R. I. C. H. Piesbergen, "Die durchschnittlichen A t o m w ä r m e n der A m B v - Halbleiter AlSb , GaAs , GaSb , InP , InAs , InSb und die A t o m w ä r m e des Elements Germanium zwischen 12 und 273 ° K," 1963.
- [46] K. K. Kelley, "Critical evaluation of high-temperature heat capacities of inorganic compounds," *US Bur. Mines Bull.*, 1949.
- [47] K. K. Kelley, "Contributions to the Data on Theoretical Metallurgy: [Part] 11. Entropies of Inorganic Substances: Revision (1948) of Data and Methods of Calculation ; United States Bureau of Mines Reports ; Contributions to the Data on Theoretical Metallurgy ; United St." United States. Government Printing Office., 1950.
- [48] V. Glushko and L. Gurvich, *Thermodynamic Properties of Individual Substances--Carbon, Silicon, Germanium, Tin, Lead, and Their Compounds: Vol. II. 3rd ed.* 1981.
- [49] K. C. Mills, *Thermodynamic data for inorganic sulphides, selenides and tellurides*. London: Butterworths, 1974.
- [50] A. Shalav, G. H. Collin, Y. Yang, T. Kim, and R. G. Elliman, "SiO_x nanowires grown via the active oxidation of silicon," *IEEE J. Sel. Top. Quantum Electron.*, vol. 17, no. 4, pp. 785–793, 2011.
- [51] S. Schmult, S. Taylor, and W. Dietsche, "Gallium beam analysis and implications for the growth of ultra-high-mobility GaAs/AlGaAs heterostructures," *J. Cryst. Growth*, vol. 311, no. 7, pp. 1655–1657, 2009.
- [52] M. A. Herman, *Molecular Beam Epitaxy Fundamentals and Current Status*, Second, Re. Springer Berlin Heidelberg, 1996.

- [53] J. Wiesenfeld and M. Yuen, "Kinetic studies of tin and germanium atom oxidation in the gas phase," *J. Phys. Chem.*, vol. 82, no. 11, pp. 1225–1230, 1978.
- [54] A. Fontijn and W. Felder, "HTFFR kinetics studies of the Ge/N₂O chemiluminescent reaction," *J. Chem. Phys.*, vol. 72, no. 8, pp. 4315–4323, 1980.
- [55] P. Load and T. Apparatus, "Operating instructions," no. 2, pp. 1–19, 2000.
- [56] R. Ave, "Models RGA100 , Residual Gas Analyzer," *Analyzer*, vol. 6.
- [57] S. I. Stepanov, V. I. Nikolaev, V. E. Bougrov, and A. E. Romanov, "Gallium oxide: Properties and applications - A review," *Rev. Adv. Mater. Sci.*, vol. 44, no. 1, pp. 63–86, 2016.
- [58] M.-S. Lee, J.-G. Ahn, and Y.-J. Oh, "Production of High-Purity Indium and Gallium Metals by Vacuum Refining," *Mater. Trans.*, vol. 43, no. 12, pp. 3195–3198, 2005.
- [59] J. Safarian and T. A. Engh, "Vacuum evaporation of pure metals," *Metall. Mater. Trans. A Phys. Metall. Mater. Sci.*, vol. 44, no. 2, pp. 747–753, 2013.
- [60] Y. Austin Chang, K. Fitzner, and M. X. Zhang, "The solubility of gases in liquid metals and alloys," *Prog. Mater. Sci.*, vol. 32, no. 2–3, pp. 97–259, 1988.
- [61] M. Zinkevich and F. Aldinger, "Thermodynamic Assessment of the Gallium-Oxygen System," *J. Am. Ceram. Soc.*, vol. 87, no. 4, pp. 683–691, 2004.

VITA

Kyungjean Min received her Ph.D. in Materials Engineering at Purdue University, West Lafayette, Indiana, USA. Meanwhile, she also received her M.S. in Materials Engineering at Purdue University, West Lafayette. Her research at Purdue focused on the processing and analysis of semiconductor materials for increasing mobility in GaAs grown by MBE. She also received B.S. and M.S. in Physics at Ewha University, Seoul, South Korea. Before starting Ph.D. degree at Purdue, she worked for the development of proton accelerator and proton beam monitors at Korea Atomic Energy Research Institute (KAERI). After completion of Ph.D. degree, Kyungjean would continue her careers in the field of semiconductors and quantum computing.